

Passive Hypervelocity Boundary Layer Control Using an Ultrasonically Absorptive Surface

Thesis by
Adam Rasheed

In Partial Fulfillment of the Requirements
for the Degree of
Doctor of Philosophy



California Institute of Technology
Pasadena, California

2001

(Submitted January 19, 2001)

© 2001

Adam Rasheed

All Rights Reserved

Acknowledgments

It is with my deepest gratitude that I thank my advisor, Professor Hans G. Hornung, for not only guiding my quest for scientific knowledge, but also for encouraging me to explore and appreciate life in itself. I would also like to thank our collaborators, Alexander Fedorov and Norm Malmuth, whose assistance was invaluable throughout this project. Special recognition is due to Bahram Valiferdowski who, for the past four years, has not only been a valuable friend, but also kindly and patiently showed me how to design, machine, build and repair anything and everything.

On a more personal level, it goes without saying that I must acknowledge the role of my family in my development and education. I am eternally grateful to my sister who, among other things, showed me how to take my first derivative and my cousin who first introduced me to the world of engineering. As for my parents, uncle and aunt, their contribution is beyond words. I would also like to thank all my friends here at Caltech who entertained or annoyed me when I wasn't working and have made my stay here enjoyable.

Lastly, I would like to acknowledge the late Professor Bradford Sturtevant who originally provided me with the opportunity to study at Caltech and to whom I am forever indebted. His tenacity and excitement for science will be sorely missed.

This work was sponsored by the Air Force Office of Scientific Research (AFOSR), under AFOSR Grant F49620-98-1-0353 (Dr. Steven Walker).

Abstract

A series of exploratory boundary layer transition experiments was performed on a sharp 5.06° half-angle round cone at zero angle-of-attack in the T5 Hypervelocity Shock Tunnel in order to test a novel hypersonic boundary layer control scheme. Recently performed linear stability analyses suggested that transition could be delayed in hypersonic boundary layers by using an ultrasonically absorptive surface that would damp the second mode (Mack mode). The cone used in the experiments was constructed with a smooth surface on half the cone (to serve as a control) and an acoustically absorptive porous surface on the other half. It was instrumented with flush-mounted thermocouples to detect the transition location. Test gases investigated included nitrogen and carbon dioxide at $M_\infty \simeq 5$ with specific reservoir enthalpy ranging from 1.3 MJ/kg to 13.0 MJ/kg and reservoir pressure ranging from 9.0 MPa to 50.0 MPa. Detailed comparisons were performed to insure that previous results obtained in similar boundary layer transition experiments (on a regular smooth surface) were reproduced and the results were extended to examine the effects of the porous surface. These experiments indicated that the porous surface was highly effective in delaying transition provided that the hole size was significantly smaller than the viscous length scale.

Contents

Acknowledgments	iii
Abstract	v
1 Introduction	1
1.1 Motivation	1
1.2 Scope of Present Work	3
1.3 Linear Stability Analysis	4
1.3.1 Incompressible Linear Stability Analysis	6
1.3.2 Compressible Linear Stability Analysis	7
1.3.3 Other Linear Stability Mechanisms	10
1.4 Transition	11
1.5 Previous Transition Experiments in T5	13
1.6 Boundary Layer Control	16
1.7 Overview	18
2 Theoretical Approach	19
2.1 General Description	19
2.2 Linear Stability Analysis	20
2.2.1 Inviscid Linear Stability Analysis	20
2.2.2 Viscous Linear Stability Analysis	22
2.2.3 Viscous Analysis with Porous Microstructure Boundary Conditions	23
2.3 Flow Physics	30
2.3.1 Acoustic Propagation in a Tube of Finite Length	30
2.3.2 Electric Transmission Line Theory	34
2.3.3 Electrical Analogy	38
2.3.4 Derivation of Series Impedance (Z)	39
2.3.5 Derivation of Shunt Admittance (Y)	43

2.3.6	Propagation of an Acoustic Wave in an Infinite Cylindrical Tube . . .	46
2.3.7	Limitations of the Electrical Analogy	51
2.3.8	Alternate Approach to the Electrical Analogy	52
2.4	Theoretical Basis for the Present Experiments	54
3	Experimental Approach	59
3.1	Experimental Objective and Method	59
3.2	T5 Hypervelocity Shock Tunnel	60
3.2.1	Description	60
3.2.2	Data Acquisition System and Tunnel Diagnostic Data	61
3.2.3	Calculation of Freestream Conditions in T5	62
3.2.4	Flow Visualization	63
3.3	Model and Instrumentation	64
3.3.1	Model Configuration	64
3.3.2	Model Verification	66
3.3.3	Test Section Setup	70
3.3.4	Instrumentation	70
3.4	T5 Soot Problem	72
3.4.1	90° Flat Plate Test Piece	72
3.4.2	5° Cylinder Test Piece	73
3.5	Heat Flux	74
3.5.1	Theoretical Heat Flux	75
3.5.1.1	Laminar Theory	76
3.5.1.2	Turbulent Theory	78
3.5.2	Experimental Heat Flux	79
3.5.3	Heat Flux Results	81
3.5.3.1	Uncertainty Analysis	84
4	Experimental Results	87
4.1	Test Conditions	87
4.2	Determination of Transition Reynolds Number (Re_{tr})	87
4.3	Enthalpy Effects on Transition	90
4.4	Effectiveness of the Porous Surface	93

4.4.1	Case I: Both Sides Laminar	93
4.4.2	Case II: Both Sides Transitional	93
4.4.3	Case III: Porous Surface Laminar, Smooth Surface Transitional . . .	94
4.4.4	Laminar Heat Flux	94
4.4.5	Summary Data	98
4.4.5.1	Nitrogen Shots	98
4.4.5.2	Carbon Dioxide Shots	98
4.4.6	Elimination of Other Causes for the Observed Effectiveness of the Porous Surface	99
4.4.6.1	Repeatability	100
4.4.6.2	Angle-of-attack	100
4.4.6.3	Axisymmetry	101
4.4.7	Effects of Surface Roughness	101
4.4.7.1	Previous Surface Roughness Experiments in T5	104
4.5	Resonantly Enhanced Shadowgraph	105
4.6	Limitations of the Experiments	105
4.6.1	Comparison with Linear Stability	105
4.6.2	Lack of Noise Spectrum Information	107
4.6.3	Model and Flow Imperfections	108
4.7	Summary	109
5	Conclusions	111
5.1	Recommendations for Future Work	111
5.1.1	Experimental	112
5.1.2	Computational	113
5.2	Final Word	114
	Bibliography	115
	A Test Conditions	126
	B Kirchhoff Solution for Acoustic Propagation in an Infinite Tube	135

C Design and Manufacturing Details	139
C.1 Perforated Sheet	139
C.2 Rolling and Welding of the Cone Sheet	142
C.3 Attachment Details	142
C.4 Thermocouple Installation	145
C.5 Interesting Alternative Material - Feltmetal	146
D Acoustic Testing	149

List of Figures

1.1	Laminar versus turbulent viscous drag on a hypersonic transport	2
1.2	Total heat and heat transfer rate for a reentry vehicle	3
1.3	Heat transfer rates for a trans-atmospheric hypersonic vehicle	4
1.4	Schematic diagram of the Mack mode in the boundary layer	8
1.5	Growth rate of first and second mode as a function of Mach number	9
1.6	Illustration of boundary layer transition process	12
1.7	Amplification rates for typical T5 shots computed using thermochemical non-equilibrium linear stability analysis	15
2.1	Amplification rates from inviscid linear stability analysis with wall reflection coefficient as a parameter	22
2.2	Amplification rates from viscous linear stability analysis with wall reflection coefficient as a parameter	24
2.3	Schematic diagram of the porous microstructure	25
2.4	Amplification rates with hole radius as a parameter	29
2.5	Growth rates as functions of the porosity and depth of the holes	29
2.6	Diagram of the acoustic model for an individual hole	31
2.7	Circuit diagram used to represent an electric transmission line	35
2.8	Diagram of the motion of the gas in narrow and wide holes	47
2.9	Calculated radial variation of the disturbance quantities in a hole	49
2.10	Axial variation of normalized particle velocity and pressure perturbation within a hole	50
2.11	Schematic drawing showing porous surface to scale	55
2.12	Calculated radial variation of the disturbance quantities for the expected experimental conditions	56
2.13	Axial variation of normalized particle velocity and pressure perturbation within a hole at the expected experimental conditions	57
3.1	Diagram of T5 Hypervelocity Shock Tunnel	61

3.2	Diagram of the test model	65
3.3	Micrograph of the weld and the perforated sheet	66
3.4	Diagram of the measured cross-section of the cone	68
3.5	Micrograph of new and blunted cone tips	69
3.6	Diagram of the thermocouple layout on the test model	71
3.7	Photograph of the 90° flat plate test piece	73
3.8	Photograph of the 5° cylinder test piece	74
3.9	Typical time-resolved temperature and heat transfer data trace	82
3.10	Typical non-dimensional spatial heat flux distribution	83
4.1	Typical non-dimensional spatial heat flux distribution used to determine transition location	88
4.2	Typical plot of cumulative sum of recursive residuals	90
4.3	Transition Reynolds number versus stagnation enthalpy	91
4.4	Reference transition Reynolds number versus stagnation enthalpy	92
4.5	Stanton number versus Reynolds number for shot 1960	95
4.6	Stanton number versus Reynolds number for shot 1963	96
4.7	Stanton number versus Reynolds number for shot 1976	97
4.8	Summary plot of the nitrogen transition data	99
4.9	Summary plot of the carbon dioxide transition data	100
4.10	Effect of surface roughness on the transition data	103
4.11	Resonantly enhanced shadowgraph for shot 2008	106
C.1	Micrograph of the polyester perforated sheet	140
C.2	Micrograph of the stainless steel perforated sheet	141
C.3	Micrograph of the final porous surface	141
C.4	Micrograph of the weld joining the perforated and solid sheets	143
C.5	Micrograph of thermocouple mounted in a test piece	145
C.6	Micrograph of Feltmetal product	146
D.1	Diagram of the setup for the static benchmark acoustic tests	149

List of Tables

2.1	Summary of the electrical analogy	40
3.1	Measured steps at cone junctions	66
A.1	Summary of the freestream conditions for the N ₂ shots	126
A.2	Summary of the edge and reference conditions for the N ₂ shots	127
A.3	Summary of the transition data for the N ₂ shots	128
A.4	Freestream molecular weight and species concentrations for the N ₂ shots as computed by NENZF	129
A.5	Summary of the freestream conditions for the CO ₂ shots	130
A.6	Summary of the edge and reference conditions for the CO ₂ shots	131
A.7	Summary of the transition data for the CO ₂ shots	132
A.8	Freestream molecular weight and species concentrations for the CO ₂ shots as computed by NENZF	133
C.1	Calculated thermal interference strains	144
D.1	Summary results for acoustic testing of samples	150

Chapter 1 Introduction

1.1 Motivation

The introduction of the concept of the boundary layer by Prandtl at the turn of the century was a watershed moment in the history of fluid mechanics. For the first time, it brought theoretical considerations, which at the time were based almost entirely on Euler's inviscid relations, into agreement with experiments. It was quickly realized that the state of the boundary layer had an enormous impact on the skin friction (viscous) drag of a body. Furthermore, the boundary layer readily transitioned from a low drag, smooth, laminar state to a higher drag, chaotic, turbulent state. The important ability to predict the location of this transition has proved to be difficult and has plagued fluid dynamicists for generations. The more desirable feature of being able to control the boundary layer to minimize drag is also a problem that has been continuously addressed over the past century. This endeavour is not unique to humankind and there are many examples of nature employing different techniques to modify the boundary layer for drag reduction. For example, the swordfish uses a swerving motion to prematurely trip the boundary layer on its sword and many fish are coated with 'slime' that reduces the skin friction coefficient. Similarly, sharks have dermal denticles whose ridges are aligned with the flow and also reduce the skin friction coefficient. This latter discovery has, in fact, been recreated artificially to reduce drag on America's Cup yachts, on an Airbus A320 and, most recently, on Olympic swimmers.

The problem of controlling the boundary layer, specifically to delay transition, takes on even greater significance when considering hypervelocity flight vehicles. In such flows, laminar boundary layers not only exhibit reduced viscous drag, but more importantly, they result in greatly reduced heating rates to the vehicle surface when compared to turbulent boundary layers. Figure 1.1 shows a comparison of the fraction of the drag coefficient due to skin friction for a generic hypersonic transport assuming fully laminar and fully turbulent boundary layers. The benefit of a fully laminar boundary layer is self-evident. These large increases in drag for turbulent boundary layers translate directly into increased vehicle weight, performance penalties and reduced payload fraction.

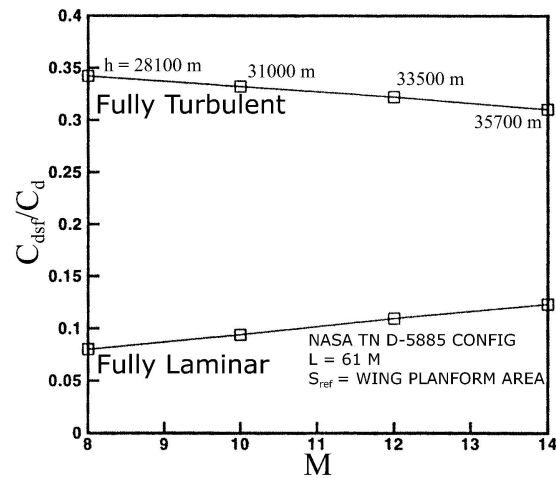


Figure 1.1: Estimated contribution of skin friction (viscous) drag to the overall drag of a hypersonic transport assuming fully laminar and fully turbulent flow. (Reproduced from Reed *et al.* [92])

The issue of aerodynamic heating is of particular concern in hypervelocity regimes. Figure 1.2a shows the results of a back-of-the-envelope calculation that estimates the total amount of heat transferred to a reentry vehicle assuming different viscous drag fractions. The case of the laminar boundary layer is seen to result in 25% of the heating experienced assuming a turbulent boundary layer. In practice, it is even more important to consider the *heat transfer rate* to the vehicle since the thermal conductivities of most materials do not allow the heat to be distributed fast enough within the structure to avoid overheating the surface. Figure 1.2b presents results from experiments that show that the heat transfer rate for a laminar boundary layer is 40% less than that of a turbulent boundary layer.

From the above discussion, the benefits of maintaining a laminar boundary layer can already be seen to be enormous; however, it takes on even greater importance when considering the next generation of orbital vehicles. One of the dreams of the aerospace industry is to achieve single-stage-to-orbit. In order to attain orbit, such trans-atmospheric vehicles will be required to fly at hypersonic speeds in the relatively dense atmosphere at lower altitudes. This is quite different from reentry vehicles which expend most of their kinetic energy in the upper atmosphere. The significance of this difference is appreciated in Figure 1.3 which shows the results of engineering estimates of the heat transfer rates expected on a trans-atmospheric vehicle as compared to the Space Shuttle. The realization that the heat transfer rates will be one order of magnitude greater than those experienced by any reusable reentry vehicle previously built is a humbling prospect.

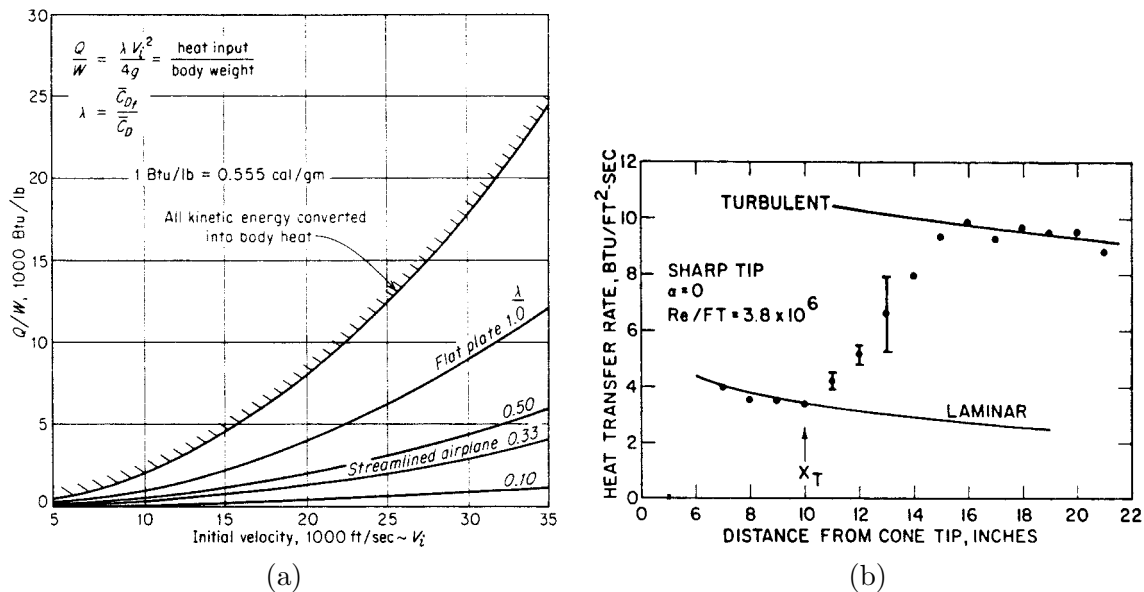


Figure 1.2: (a) Estimate of total heat transferred to a reentry vehicle with the viscous drag fraction as a parameter. The amount of heat absorbed assuming a laminar boundary layer (viscous drag fraction = 0.10) is seen to be 25% of that for a turbulent boundary layer (viscous drag fraction = 0.33). (Reproduced from Dorrance [28]) (b) Experimental data obtained on a sharp cone at $M = 5.5$ showing that the heat transfer rate for a laminar boundary layer is 40% less than that of a turbulent boundary layer. (Reproduced from Stetson and Rushton [113])

From fish swimming in the sea to the Space Shuttle returning to the Earth, it is clear that the problem of controlling boundary layer transition needs to be addressed. Although sometimes nature can be used as a guide for human beings, this can not always be done and one must then rely on theory and extensive wind tunnel testing.

1.2 Scope of Present Work

The present effort is an exploratory experimental investigation of a novel passive hypervelocity laminar boundary layer control scheme proposed by Fedorov and Malmuth [32]. The scheme, based on the results of linear stability analysis, involves using an ultrasonically absorptive surface in order to damp the acoustic-like Mack mode which is the dominant instability that leads to transition of the hypersonic boundary layer. The present experiments combine the above-mentioned theoretical work with the extensive previous boundary layer transition experiments performed in T5 by Germain [38] and Adam [2] supported by the results of non-equilibrium, chemically reacting, linear stability calculations by Johnson *et al.* [51]. These three bodies of work are crucial and form the basis for the present

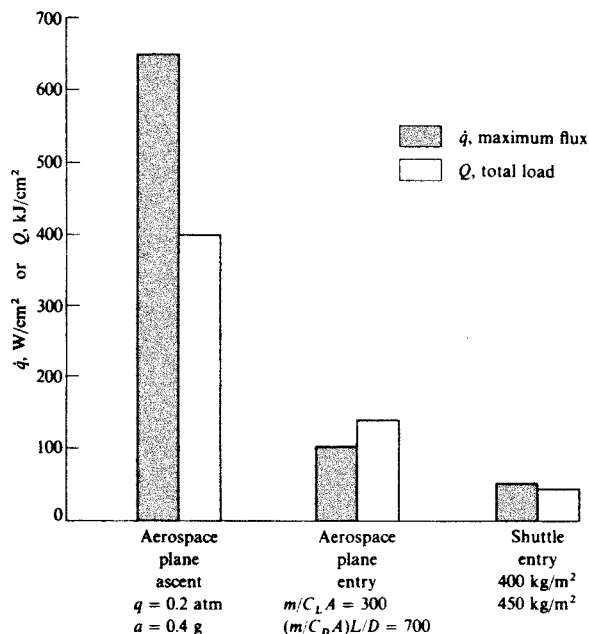


Figure 1.3: Engineering estimates of the heat transfer rates expected on a trans-atmospheric vehicle are found to be more than one order of magnitude greater than those experienced by the Space Shuttle. (Reproduced from Anderson [3], after Tauber [126])

experiments. The objective of this work was to broadly test the theoretical prediction of linear stability analysis that ultrasonic absorption would delay transition in the hypervelocity boundary layer. In order to understand the experiments, however, it is first necessary to understand the concepts of linear stability analysis, its use and limitations, and its role in understanding transition and boundary layer control schemes.

1.3 Linear Stability Analysis

Some of the earliest studies of linear stability of fluid flows can be traced to Rayleigh, who prepared a series of papers concerning the instability of inviscid flows. At roughly the same time, Reynolds was performing his pioneering experiments on transition from laminar to turbulent flow in pipes and postulated that this transition occurred because of an instability in the laminar flow. The relevance of this hypothesis to boundary layers became apparent in 1914 when Prandtl carried out his experiments with spheres showing that the boundary layer could also be either laminar or turbulent. This led many researchers to begin theoretical investigations into the transition process, but it was Tollmien who, in 1929, was the first to compute the critical Reynolds number for a boundary layer on a flat-

plate. Schlichting subsequently contributed a series of papers on this topic, and Tollmien contributed a second paper, resulting in a well-developed viscous theory of boundary layer instability. A summary of their work can be found in Schlichting [104]. At the time, this theory was hotly contested and essentially rejected by the scientific community since no experiment had been successful in observing these waves and, more importantly, it was felt that linear theory should have little relevance to transition to turbulence which is a highly non-linear process. This opinion remained unchanged until the ground-breaking experiments of Schubauer and Skramstad [106] conclusively demonstrated the existence of instability waves in the subsonic laminar boundary layer and the theory's successful quantitative description of their behaviour.

Since then, linear stability theory has been developed extensively. Both theory and experiments have been extended with some success to include compressibility, pressure gradients, wall cooling and heating, blowing and suction, and many other effects. A complete review of the present-day knowledge of linear stability analysis is not possible here. Instead, the basic principles of the analysis will be described and the main results relevant to the present experiments will be discussed. Mack's review [69] is the most comprehensive and detailed compilation of linear stability analysis to date and includes the derivations for the linear stability equations for both incompressible and compressible flow. Other review articles by Reshotko [96], and more recently, by Reed *et al.* [93] also provide excellent discussion. Stetson's article [111] is the most complete review of hypersonic linear stability analysis and boundary layer transition and is the most applicable to the present work.

A typical linear stability analysis involves linearizing the equations of motion about mean flow quantities, assuming a particular (typically normal-mode) form for the disturbances, and then solving the resulting eigenvalue problem. An additional typical assumption in this analysis is that there are no variations in the downstream direction. Of course, this is not strictly valid for a boundary layer. It is, however, a reasonable assumption over short distances and is often referred to as the locally parallel assumption. The normal-mode form for a three-dimensional disturbance quantity is typically expressed as $q(x, y, z, t) = q(y)e^{j(\alpha x + \beta z - \omega t)}$, where q is a flow quantity such as velocity or pressure, x is the streamwise direction, z is the transverse direction, y is the wall normal direction, t is time, α and β are the wavenumbers in the x and z directions, ω is angular frequency and $q(y)$ represents the mode shape of the given flow quantity. The solution to the eigenvalue

problem determines the values of the last four quantities. It is common to perform the analysis using only two-dimensional disturbances, in which case β is taken to be zero. In both cases, the stability of these travelling waves can be determined by examining the sign of the real part of the exponent. A temporal stability analysis is performed by assuming α to be real and allowing $\omega = \omega_r + j\omega_i$ to be complex. In this case, if the imaginary part of ω is positive then there is unbounded exponential growth of the wave (*i.e.*, it is unstable). An alternative is to perform a spatial stability analysis by assuming ω to be real and allowing $\alpha = \alpha_r + j\alpha_i$ to be complex. This time, if the imaginary part of α is negative then the waves are unstable and will result in unbounded growth of the disturbances.

1.3.1 Incompressible Linear Stability Analysis

Following the steps of linear stability analysis of linearizing the equations of motion and assuming normal-mode disturbances for the case of an incompressible, viscous fluid results in the Orr-Sommerfeld equation; a fourth order linear ordinary differential equation. It was this equation that formed the basis for the work of Tollmien and Schlichting. Taking the limit of this equation as Reynolds number approaches infinity (*i.e.*, the inviscid limit) results in the Rayleigh equation which had been studied extensively by Rayleigh before the turn of the century.

Linear stability theory applied to incompressible flows obtained several important results. First, it was shown by Squire that in two-dimensional incompressible boundary layers, the most unstable disturbances were also two-dimensional (*i.e.*, they propagated in the same direction as the mean flow). This was a significant finding since it became sufficient to solve a much simpler problem using only two-dimensional disturbances. Second, it was initially Rayleigh who obtained the result that a necessary condition for inviscid instability is that the velocity profile must have an inflection point. This, unfortunately, initially led to the erroneous belief that viscosity would be a stabilizing effect since the velocity profile in a viscous, zero-pressure gradient boundary layer does not have an inflection point. For this reason, the presence of laminar instability waves (Tollmien-Schlichting or T-S waves) in a viscous boundary layer is referred to as a viscous instability since it is the effect of viscosity that allows a velocity profile without an inflection point to result in instability. These T-S waves are low frequency, slow moving vorticity disturbances that are close to the wall with wavelengths that are approximately six times the boundary layer thickness.

As indicated previously, since the time of Reynolds, it has been believed that instability waves were related to transition to turbulence. For this reason, early efforts were made to find solutions which reduced the growth rate of the T-S waves. These studies revealed that a cold wall reduced these growth rates and this led to the prediction by linear theory that wall cooling would stabilize the boundary layer. Favourable pressure gradients and wall normal suction were also found to reduce the disturbance growth rates and were also expected to stabilize the boundary layer.

1.3.2 Compressible Linear Stability Analysis

The most significant early attempt to extend linear theory to include the effects of compressibility was performed by Lees and Lin [64]. Their work led to the necessary and sufficient condition of the existence of a generalized inflection point ($D(\rho DU) = 0$, where D is differentiation with respect to the wall normal direction) for inviscid instability. The importance of this generalized inflection point is recognized when one realizes that a boundary layer in supersonic flow over an insulated surface always exhibits this inflection point. This implies that all such boundary layers are unstable to inviscid waves.

The analysis by Lees and Lin, however, only included the effects of subsonic disturbances (with respect to the mean velocity at the generalized inflection point). Under such conditions, the equations exhibit elliptic behaviour and there is a unique unstable eigenvalue, as in the incompressible case. This instability mode is similar to the Tollmien-Schlichting mode and is commonly referred to as the ‘first mode’. If, however, supersonic disturbances are considered, the equations are hyperbolic and an infinite set of discrete eigenvalues can be obtained. This important point was appreciated by Mack and it is his theoretical work that forms the basis of most of the current knowledge of supersonic and hypersonic boundary layer instability. These ‘higher modes’, commonly referred to as Mack modes, exist even in the absence of viscosity, and are thus considered to constitute an inviscid instability. They exist as high frequency, acoustic disturbances that reflect between the solid wall and the sonic line in the boundary layer as shown in Figure 1.4. In essence, the boundary layer behaves as an acoustic wave guide and the unstable disturbances grow in amplitude in a manner analogous to resonance. The lowest order of these higher modes, commonly referred to as the ‘second mode’, was found to be the most unstable of these modes. Furthermore, unlike the first mode, Mack showed that this second mode was destabilized by wall cooling.

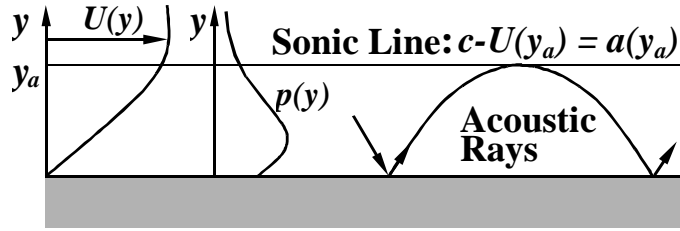


Figure 1.4: Schematic diagram showing the Mack mode in the boundary layer. $U(y)$ is the mean flow velocity profile, $p(y)$ is the disturbance pressure profile, c is the phase velocity of the waves, a is the local speed of sound, y_a is the location of the sonic line (*i.e.*, the location in the boundary layer where the disturbances are sonic relative to the local mean flow velocity). (Reproduced from Fedorov and Malmuth [32])

The importance of the second mode (or Mack mode) is seen in Figure 1.5, which shows the maximum amplification rates of the instability waves as a function of Mach number. The maximum growth rate of the first mode is shown to decrease as Mach number is increased. Furthermore, the most unstable first mode frequencies occur for waves that are oblique to the main flow ($\psi > 0$) and must essentially be considered as three-dimensional disturbances (*i.e.*, Squire's theorem does not hold). This is different from the behaviour in incompressible flows ($M \rightarrow 0$) where the most unstable waves are parallel to the mean flow. For supersonic flows, the oblique first mode waves are seen to be the dominant mode, and they were found to be stabilized by wall cooling, favourable pressure gradients and boundary layer suction just as in the incompressible case. As Mach number increases, however, the second mode is seen to come into existence and very quickly becomes the dominant instability mode for $M > 4$. This observation, combined with the fundamentally different nature of the second mode as compared to the first mode, led to the conclusion that the problem of hypersonic boundary layer transition must be treated separately from subsonic and supersonic transition. In particular, it was appreciated that any attempt to control the hypersonic boundary layer must directly address the Mack mode. This realization represented a significant advancement in the understanding of boundary layer transition and explained some previously unexplained experimental results.

Some of the first hypersonic boundary layer stability experiments were performed by Demetriades [25]. These experiments, however, were performed before the theoretical work of Mack and they did not identify the higher modes. Other experiments by Stetson and Rushton [113], also before the work of Mack, found that wall cooling was a destabilizing effect on hypersonic boundary layers. At the time, this 'transition reversal' was subject

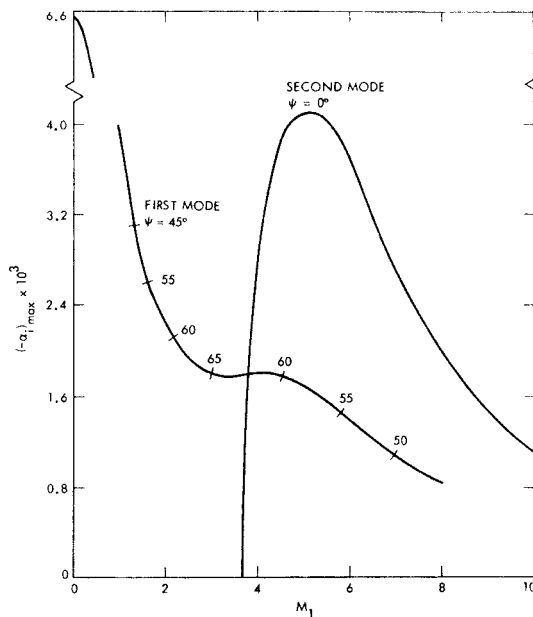


Figure 1.5: Results of spatial linear stability analysis for supersonic flow over a cone showing the growth rate of the first and second modes as functions of Mach number. (Reproduced from Mack [67])

of much discussion [95] since it was the opposite of what was found in subsonic and low supersonic flows. The pioneering experiments by Kendall [56] provided the first experimental evidence of the existence and dominance of second mode disturbances in hypersonic boundary layers over flat-plates and cones. Subsequent stability experiments by Demetriades [26], Stetson *et al.* [114, 115, 116, 117] and Stetson and Kimmel [112] on 5° and 7° cones investigated a wide variety of parameters including nose-tip bluntness, angle-of-attack, wall cooling and other effects. More recent experiments by Kimmel *et al.* [58] used hot-wire measurements at multiple points and represent the first attempt at understanding the spatial structure of the instability waves in hypersonic laminar boundary layers. Lachowicz *et al.* [63] have recently performed the first instability experiments in a quiet hypersonic tunnel and have reaffirmed that the second mode is indeed the dominant mode.

Through the combination of theory and experiments, a number of interesting phenomena related to the second mode have been found. In particular, the second mode disturbances appear to be highly tuned to the boundary layer. It was experimentally shown by Demetriades [26] and Stetson *et al.* [118] that the disturbances travel at a phase speed that is approximately equal to the boundary layer edge velocity and that their wavelength is approximately twice the boundary layer thickness. This allows a quick estimate of the fre-

quency of the most unstable mode through the relation $f \simeq U_e/(2\delta)$, where f is frequency, U_e is the boundary layer edge velocity and δ is the boundary layer thickness. For hypervelocity flight vehicles travelling at 6 km/s with a boundary layer approximately 10 mm thick, the Mack mode frequency would be approximately 300 kHz.

Once again, because of the recognition of the role of linear stability with respect to transition, a variety of numerical studies were performed to identify regimes that minimized the growth rates of the second mode. It has already been mentioned that Mack had demonstrated that, although wall cooling was a stabilizing influence on the first mode, it was a strong destabilizing influence on the second mode. This effect is of particular importance for hypervelocity flight vehicles where structural considerations require that the wall temperature be very small compared to boundary layer temperatures; in essence it is a cold wall. Further work by Malik [70], and Zurigat *et al.* [136] showed that similar to the first mode, the second mode was stabilized by favourable pressure gradients. In addition, Malik showed that the second mode was stabilized by boundary layer suction. It is only very recently that linear stability analysis has begun to include real gas effects that are important at high temperatures. Early work in this area by Malik and Anderson [71] assumed thermal and chemical equilibrium, while later work by Stuckert and Reed [122] considered chemical non-equilibrium (but still thermal equilibrium). Numerical studies by Bertolotti [9] which considered thermal non-equilibrium (but no chemistry) have shown that the assumption of thermal equilibrium is too restrictive and, in fact, vibrational relaxation by itself is destabilizing to the second mode. The most recent work, however, by Hudson *et al.* [50] and Johnson *et al.* [51] have included both chemical and thermal non-equilibrium effects. This last study indicates that the use of thermochemical non-equilibrium effects in establishing the mean flow is slightly destabilizing. This, however, is greatly overshadowed by the strong stabilizing effect of having chemistry in the disturbances themselves.

1.3.3 Other Linear Stability Mechanisms

So far, the description of linear stability analysis presented above has only considered two types of disturbances (first mode and acoustic second mode) that experience linear amplification leading to transition. These modes are indeed the dominant modes in two-dimensional planar and axisymmetric flows. There are, however, at least two other modes that can exist depending on the flow being considered.

The first of these, known as cross-flow instability, typically occurs in three-dimensional boundary layers such as those found on swept wings and cones at angles-of-attack. It occurs as a result of an inflection point in the cross-flow velocity profile. Most of the current knowledge relates to low-speed flows and is reviewed by Saric [103]. The most important observation is that these waves are only weakly affected by cooling. Very recent experiments on an elliptic cone by Kimmel *et al.* [59] and Poggie *et al.* [88] are the first to study cross-flow instability in hypersonic flow. Their preliminary results indicate that the cross-flow instability may be the dominant instability and the nature of the transition process is quite different from that previously observed on cones and flat-plates.

The other type, known as Görtler instability, manifests itself in the form of pairs of counter-rotating vortices produced by concave streamline curvature. Once again, little is known about this instability with respect to hypersonic flows. Although it has not been studied explicitly, knowledge of this instability was recently used to design the first quiet hypersonic nozzle [17]. A review of this instability at lower speeds is provided by Saric [102]. Finally, recent theoretical work by Malmuth [72] suggests another mechanism for wave amplification by the shock layer in the strong interaction region.

1.4 Transition

The general process by which transition is believed to occur is shown schematically in Figure 1.6 for the specific case of incompressible flow. A similar process is believed to occur for the second mode, and most likely also for the cross-flow instability and Görtler instability mechanisms when they are relevant. Initially, a stable laminar boundary layer exists and all linear instability waves are damped. As the critical Reynolds number is reached, waves of particular frequencies become unstable and experience unbounded growth. The unstable waves grow in amplitude to the point that non-linear processes take over and turbulent spots begin to appear before the boundary layer ultimately transitions to turbulence.

The above description gives a relatively straightforward process for the onset of transition. Unfortunately, in reality it is not necessarily this clear since transition to turbulence is affected by many external factors. For the sake of brevity, only two of these will be mentioned here. First, the previous description assumes a completely linear growth process. In reality, the formation of turbulent spots which ultimately leads to transition is highly

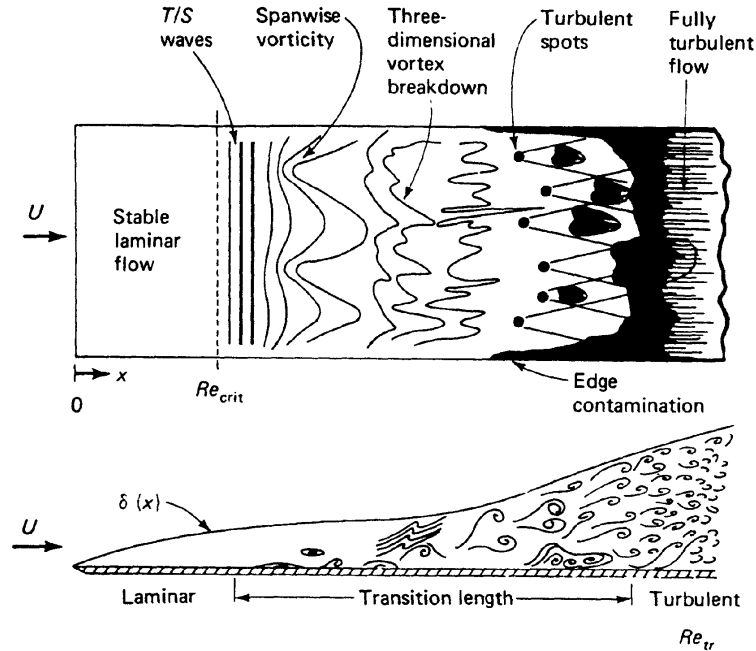


Figure 1.6: Schematic diagram showing the transition process from the initial linear amplification of instability waves through to the formation of turbulent spots and transition. (Reproduced from White [132])

non-linear. In fact, as noted by Morkovin [78], when the freestream disturbances are large, the entire linear amplification regime can be bypassed and transition to turbulence can occur almost immediately. Furthermore, there is reason to believe that, in certain cases, non-linear interactions between different modes may cause the formation of turbulent spots, even though each of these modes individually would not cause transition. The second point deals with one of the most vexing issues with wind tunnel transition experiments and it is the fact that the onset of transition is highly dependent on the freestream noise. For supersonic and hypersonic wind tunnel experiments, most of this noise is radiated from the nozzle wall boundary layer and every wind tunnel has its own characteristic noise spectrum. In fact, Pate and Schueler [84] correlated transition data from nine different wind tunnels and showed that the transition Reynolds number was dependent on the nozzle turbulent boundary layer, aerodynamic noise characteristics and test section size. The result is that wind tunnel experiments often underpredict the transition Reynolds number by an order of magnitude when compared with similar free-flight experiments since the atmosphere has very low noise levels. Significant effort has been made to design and build quiet wind tunnels and the measured transition Reynolds number in such facilities have been shown to

compare well with free-flight data [16]. A proper transition experiment must, therefore, not only include Mach number and Reynolds number in its similarity criteria, but also the environmental conditions.

It is important to note that this is the best understanding of how transition occurs. As Stetson [111] observes, there is no transition theory. Linear stability in itself can not predict the onset of transition, rather it simply predicts the unstable growth of waves in the laminar boundary layer. The most common prediction tool used, the so-called e^N method by Smith and Camberoni [108], assumes that transition occurs when the amplitude ratio of the most unstable mode reaches a value of e^N where N was found to range from 9 to 11 as determined by correlation with experiments. At best, this is a semi-empirical method, where the value of N can depend drastically on the flow configuration, the environment and the exact instability mechanism. Despite this apparent incompleteness, the value of stability theory can not be overstated. It provides valuable information about the processes that lead up to transition and, as alluded to earlier, it provides clues as to how a boundary layer can be controlled.

1.5 Previous Transition Experiments in T5

An extensive series of experiments studying boundary layer transition over a 5° smooth surfaced cone has previously been performed in the T5 Hypervelocity Shock Tunnel by Germain [38] and Adam [2] at flow speeds around 5 km/s and freestream temperatures around 4000 K. These experiments represented the first attempt to study real gas effects on boundary layer transition in hypervelocity conditions and an extensive database of results in air, nitrogen and carbon dioxide was generated. All previous hypersonic boundary layer experiments were conducted at low enthalpies where the effects of vibrational excitation and chemical dissociation/recombination were non-existent. Due to the harsh environment at these conditions, it was not (and still is not) possible to perform proper stability experiments to directly measure the presence and characteristics of instability waves. Instead, the experiments were transition experiments that measured the transition location as a function of stagnation enthalpy. Transition experiments in hypervelocity (as opposed to hypersonic flow) are scarce, so it should be mentioned that the only other experiments are flat-plate experiments by He and Morgan [44], and Mee [75, 76]. The most recent work by Mee is

the closest to a true stability experiment in the sense that it identifies the formation of turbulent spots and tracks the growth of the transition region.

In addition to capturing a flow visualization (resonantly enhanced shadowgraph) image of the boundary layer transition process, the experiments by Germain and Adam determined the dependence of transition Reynolds number (Re_{tr}) on specific stagnation enthalpy (h_o). One of the main results obtained by Germain was that the transition Reynolds number correlated with specific stagnation enthalpy provided that the Reynolds number was calculated at a reference temperature (Re_{tr}^*) rather than the boundary layer edge conditions. Furthermore, the Re_{tr}^* was consistently higher in air than in nitrogen and even still higher in carbon dioxide. This delay in transition for the different gases was attributed to the increased chemical activity acting as a damping mechanism on the growth rate of the instability waves. Carbon dioxide has the lowest dissociation energy and a larger number of vibrational modes, and therefore exhibited the strongest damping effect and the greatest increase in transition Reynolds number.

Another interesting result obtained from the experiments was that the flow visualization images seemed to indicate that low frequency waves were present in the boundary layer. This suggested that perhaps the first mode may be the dominant mode. This evidence was not particularly strong, and certainly all theoretical results indicated that the second mode should be the dominant mode. Subsequent linear stability calculations which included thermochemical non-equilibrium effects were performed by Johnson *et al.* [51] for direct comparison with the T5 experiments. Figure 1.7a shows the computed amplification rates for a typical T5 high enthalpy shot in air with (solid line) and without (dashed line) the effects of vibrational excitation and chemistry, while Figure 1.7b shows the same for a shot in carbon dioxide. The frequencies of the most strongly amplified mode are seen to be approximately 1 to 3 MHz and such high frequencies are highly indicative of the second mode. Furthermore, these calculations showed a strong damping effect of the amplification rates because of vibrational excitation and chemistry. As anticipated from the experiments, the damping effect is seen to be much more pronounced for the carbon dioxide case.

The stabilizing trends of the second mode in the computations correlate very well with the trends observed in the experiments. From this, it is reasonable to conclude that the dominant instability mode in the T5 experiments was indeed the high frequency Mack mode. Assuming this to be the case, it is possible to estimate the wavelength of the second

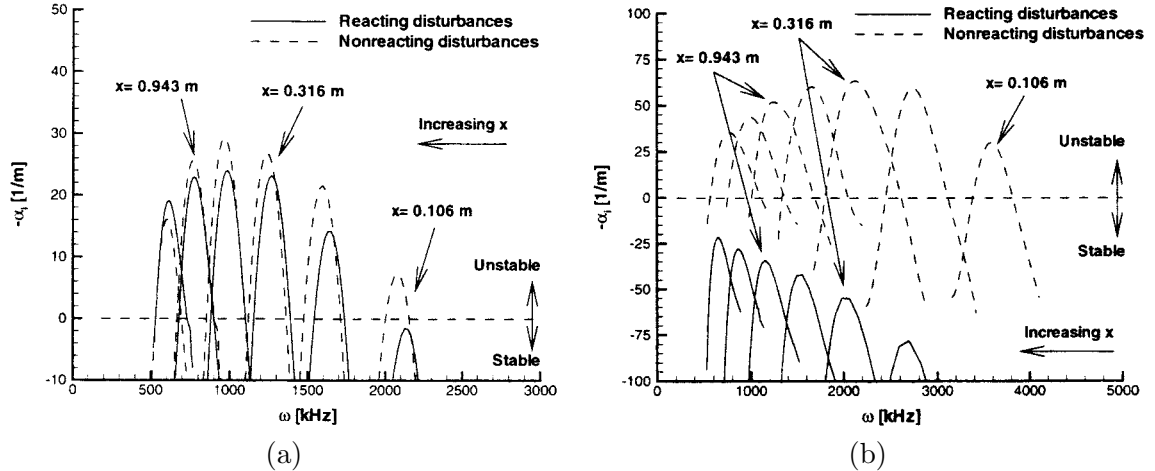


Figure 1.7: Results of linear stability calculations with thermochemical non-equilibrium effects for (a) T5 shot 1162 (in air, $h_0 = 9.3$ MJ/kg) and (b) T5 shot 1150 (in carbon dioxide, $h_0 = 4.0$ MJ/kg). The frequencies are seen to be of the order of megahertz which is indicative of the dominance of the Mack mode. The thermochemical non-equilibrium effects are seen to damp the growth rates (solid lines are below the dashed lines), with the effect being more pronounced in carbon dioxide. (Reproduced from Johnson *et al.* [51])

mode waves based on the boundary layer thickness. Numerical simulations by Adam [1] (along with approximate measurements made from the shadowgraphs) indicated that the boundary layer thickness ranged from 0.5 mm to 1 mm. The second mode, therefore, has a wavelength of approximately 1 mm to 2 mm at the T5 conditions. Noting that a typical boundary layer edge velocity is about 5 km/s and using the equation $f \simeq U_e/(2\delta)$, the frequency can be estimated purely from the experimental data to be around 2.5 to 5 MHz which also agrees with the linear stability calculations.

Finally, Adam performed comparisons of the T5 experimental results with experimental flight data obtained from the NASA reentry F flight tests performed in the late 1960's by Wright and Zoby [135]. These flight tests were performed on a 5° half-angle cone and also encompassed the specific stagnation enthalpies achieved in the T5 experiments, making them well suited for a direct comparison. Comparing the results using the reference transition Reynolds number collapsed the T5 experimental data to within a factor of 1.5 of the flight experiment data. As noted earlier, since the shock tunnel's noise spectrum does not match the free-flight conditions, this result was not expected. It does, however, seem to support Stetson's [111] hypothesis that shock tunnels are probably relatively quiet in the very high frequency range of the Mack mode which dominates the process to transition at these conditions.

1.6 Boundary Layer Control

As indicated earlier, the desire to control a boundary layer, specifically to extend the laminar region, is of utmost importance in all flight regimes for the purposes of drag and heating reduction. To this end, many boundary layer control schemes have been proposed based on linear stability analysis. For subsonic and supersonic flow, linear stability analysis showed that wall cooling, favourable pressure gradients and suction all had strong stabilizing effects on the growth rates of the T-S waves. These results formed the basis for a variety of wind tunnel experiments and flight tests for subsonic and supersonic flows, although none have been successfully used in an operational environment for a variety of practical reasons. To date, boundary layer control has not been used on any hypervelocity flight vehicle.

In general, there are three classes of boundary layer control schemes and they are discussed in the order of increasing complexity. The first is passive control which seeks to increase the length of the laminar boundary layer without necessarily introducing disturbances in the flow. Special surface coatings and natural flow control (NFC) which uses appropriate shaping of the aerodynamic surface to induce a favourable pressure gradient are such concepts. The second is active control which seeks to control the boundary layer through an open-loop control scheme. Laminar flow control (LFC) techniques such as boundary layer suction and wall cooling fall into this category. Active techniques are significantly more complicated than passive techniques, often requiring the use of complicated plumbing and pumps which ultimately lead to significant weight gains for an aircraft. The third is reactive control which uses closed-loop control schemes to delay transition. These techniques tend to be complicated and use a variety of schemes to introduce disturbances that are in counter-phase to the original laminar instability waves with the intention of cancelling the latter. This can include concepts such as wall vibrations and periodic blowing/suction or heating/cooling. More recently, with the understanding of the role of the second mode, such concepts have included the use of acoustic perturbations in hypersonic flows. These techniques are the most complicated since they require an in-depth knowledge of the noise environment or sensors to determine the characteristics of the instability waves.

Historically, active control techniques have been pursued the most aggressively. Although wall cooling was successful in wind tunnel experiments, it appeared to be less practical for actual flight vehicles. In particular, flight vehicles tend to have swept wings in

which cross-flow instabilities become important and as noted earlier, these instabilities are not strongly stabilized by wall cooling. An extensive series of experiments and flight tests with an F-94 were performed by Goldsmith [39, 40], Pfenninger *et al.* [86], Groth *et al.* [43], and Carmichael *et al.* [13, 14] at Northrop Corporation throughout the 1950's and 1960's. These same individuals were involved with similar experiments on the NASA X-21. A detailed review of this early work can be found in Pfenninger [85]. Subsequent flight research experiments were performed by NASA using an F-111 and F-14 to examine the effects of crossflow. In addition, during the 1980's, NASA used a C-140 Jetstar to examine the robustness of leading edge LFC with respect to insect, ice, snow and other contamination. More recent investigations into laminar flow control include flight tests on a modified 757 aircraft and on the tail fin of an A320 aircraft [19]. In addition NASA initiated a test program in 1990 to demonstrate the first supersonic LFC using their F-16XL laminar flow control test aircraft [80]. Recent reviews on early and present day laminar flow control computations, experiments and flight tests can be found in Braslow [11] and Joslin [52]. These experiments and flight tests all achieved varying degrees of success, attaining laminar flow over significant portions of the wing surface and attaining significant reductions in drag (as much as 5%). Unfortunately, contamination from pollution, insects, icing and other atmospheric conditions limit their effectiveness. These operational issues combined with the increased cost and weight penalty typically prevent the widespread use of such active control techniques.

The progress of active boundary layer control in subsonic and supersonic flow over the past fifty years has been slow, but steady, and the role of linear stability analysis in suggesting possible successful boundary layer control schemes is now well established. The benefits of maintaining laminar flow over a significant portion of a hypervelocity flight vehicle are also well known. For trans-atmospheric vehicles, both the reduction in heating and drag are of significant value, while the heat reduction is still of enormous value for reentry vehicles. The prospect, however, of using active or reactive boundary layer control on a hypervelocity flight vehicle is daunting. Ideally, a simple passive control scheme is desired and linear stability analysis can be used as a guide. The recent linear stability analysis of Fedorov and Malmuth proposes such a scheme using an acoustically absorbing surface that directly damps the Mack mode. The experimental testing and proof-of-concept of this idea is the subject of this thesis.

1.7 Overview

This introductory chapter has given a brief, but broad, introduction into the principles of linear stability analysis and the insights it has given into the important process of boundary layer transition. Although linear stability analysis can not predict transition, it is highly successful in suggesting boundary layer control schemes once the nature of the instability waves is known. The T5 boundary layer experiments by Germain and Adam, combined with the computations of Johnson *et al.*, have conclusively demonstrated that the most dominant mode in the T5 experiments is the Mack mode. In Chapter 2, the linear stability analysis of Fedorov and Malmuth which proposes the use of an ultrasonically absorbing surface to damp the Mack mode is described. In addition, the physical mechanism of this damping process is elucidated. Chapter 3 describes the experimental setup for the experiments performed to test the proposed boundary layer control scheme. This includes the details of the T5 Hypervelocity Shock Tunnel, the model, and the instrumentation used for the tests. Chapter 4 presents the analysis methods and the results of the experiments. Finally, Chapter 5 summarizes the current work and makes recommendations for future efforts.

Chapter 2 Theoretical Approach

This chapter summarizes the theoretical and computational work that forms the basis for the experiments. It first describes the linear stability analysis performed by Fedorov and Malmuth that predicted the reduction in growth rates of the unstable waves. The physics of the flow are then examined and the validity of the electrical analogy used in the stability analysis is discussed. The fundamental analysis originally performed by Kirchhoff is then presented in order to better understand the details of the mechanism of the attenuation of the unstable waves. Finally, the theory is used to determine the required parameters for the present experiments.

2.1 General Description

As outlined in the previous chapter, it is generally accepted that, in the absence of large flow disturbances, transition of the two-dimensional or quasi-two-dimensional hypersonic boundary layer ($M > 4$) is caused by the amplification of the second mode (Mack mode) which is acoustic in nature. In this case, the boundary layer acts as an acoustic wave guide as high frequency pressure perturbations become trapped in the boundary layer, grow in amplitude, and eventually cause the boundary layer to transition from laminar to turbulent. Fedorov and Malmuth postulated that these high frequency acoustic waves could be damped by choosing a suitable ultrasonically absorbing surface, thereby reducing the second mode growth rate and ultimately delaying transition¹. In particular, a ‘porous’ surface with suitably sized cylindrical blind microholes (*i.e.*, holes with closed bottoms) arranged in a rectangular grid was proposed as the ultrasonically absorbing surface. The term ‘porous’ is somewhat of a misnomer since no flow actually passes through the holes. The appropriate boundary conditions to represent this surface were applied and this hypothesis was successfully tested numerically using linear stability analysis.

¹U.S. patent number 5884871 issued to Boeing, March 23, 1999 (Dr. Alexander V. Fedorov and Dr. Norman D. Malmuth).

2.2 Linear Stability Analysis

The complete set of linear stability analyses which formed the basis for these experiments is summarized below and is described in detail in Fedorov and Malmuth [31]. The initial inviscid analysis is also described in Fedorov *et al.* [33] and the details of the viscous analysis are also presented in Fedorov and Malmuth [32]. These analyses are similar to typical linear stability analyses performed in the past. The innovation by Fedorov and Malmuth is the use of a generic boundary condition to represent the ultrasonically absorbing surface. The even more significant innovation is the development and use of boundary conditions to represent the specified surface microstructure of equally spaced cylindrical blind microholes.

2.2.1 Inviscid Linear Stability Analysis

The linear stability analysis considered two-dimensional supersonic boundary layer flow over a flat plate. The inviscid, compressible stability equations can be derived for linearized, locally parallel, viscous flow of a heat conducting perfect gas in the limit of zero heat conduction and infinite Reynolds number. The details of this derivation are provided in Mack [69]. In general, for compressible linear stability analysis, Squire's theorem does not hold since the energy dissipation terms in the energy equation do not transform properly from the three-dimensional problem to an equivalent two-dimensional problem. For the inviscid, compressible case, however, these terms are ignored and Squire's theorem can be used to note that the most unstable disturbances are two-dimensional and are parallel to the mean flow. It is, therefore, adequate to only consider two-dimensional normal-mode disturbances of the form

$$[\tilde{u}, \tilde{v}, \tilde{p}, \tilde{\theta}]^T(x, y, t) = [u(y), v(y), p(y), \theta(y)]^T e^{j(\alpha x - \omega t)}, \quad (2.1)$$

where u and v are the velocity components in the x and y directions, p is the pressure, θ is the temperature, the tilde (\sim) quantities are the disturbance quantities, α is the wavenumber, and ω is the frequency. The final linearized normal mode equations to be solved are

$$v^{*'} = \frac{U^*}{U^* - c^*} v^* + j\alpha^* \frac{T^* - M^2(U^* - c^*)^2}{U^* - c^*} p^*, \quad (2.2)$$

$$p^{*'} = -j\alpha^* \frac{U^* - c^*}{T^*} v^*, \quad (2.3)$$

where U^* and T^* are the mean flow velocity and temperature which are both functions of y^* , M is the edge Mach number, $c^* = \omega^*/\alpha^*$ is the complex wave speed and the primes ($'$) denote differentiation with respect to y^* . The star ($*$) expressions represent non-dimensional quantities that have been non-dimensionalized with respect to the displacement thickness (δ^*), the local boundary layer edge velocity (U_e) and the local edge temperature (T_e). Pressure is referenced to twice the dynamic pressure ($\rho_e U_e^2$) and the wavenumber and frequency are non-dimensionalized by $\alpha^* = \alpha \delta^*$ and $\omega^* = \omega \delta^*/U_e$, respectively.

As stated earlier, the difference from the analysis by Mack is in the boundary conditions which are now

$$v^*(0) = A p^*(0), \quad p^*(\infty) = 0, \quad (2.4)$$

where A is a complex absorption coefficient that depends on the surface properties. An expression for this absorption coefficient remains to be determined. By rearranging the above system of equations, one can derive the following relation for pressure fluctuations

$$p^{*''} - \left(\frac{2U^{*'}}{U^* - c^*} - \frac{T^{*'}}{T^*} \right) p^{*' } + \lambda^2 p^* = 0, \quad \lambda^2 = \alpha^{*2} \left[\frac{M^2(U^* - c^*)^2}{T^*} - 1 \right], \quad (2.5)$$

with the boundary conditions

$$p^*(\infty) = 0, \quad p^{*'}(0) = A \frac{j\alpha^* c^*}{T^*(0)} p^*(0). \quad (2.6)$$

Using the WKB method, the solution to Equation 2.5 can be expressed as:

$$p(y) = \hat{p}_1^*(y) e^{-j \int_0^y \lambda dy} + \hat{p}_2^*(y) e^{j \int_0^y \lambda dy} + O(\epsilon), \quad (2.7)$$

$$\hat{p}_{1,2}^*(y) = Const_{1,2} \frac{U - c}{\sqrt{T}} \left[\frac{M^2(U - c)^2}{T} - 1 \right]^{-0.25}, \quad (2.8)$$

where \hat{p}_1^* is the incident wave, \hat{p}_2^* is the reflected wave from the surface, and $\epsilon = 1/\max(|\lambda|)$ is small. The reflection coefficient is defined as

$$\tau = \frac{\hat{p}_2^*(0)}{\hat{p}_1^*(0)}, \quad (2.9)$$

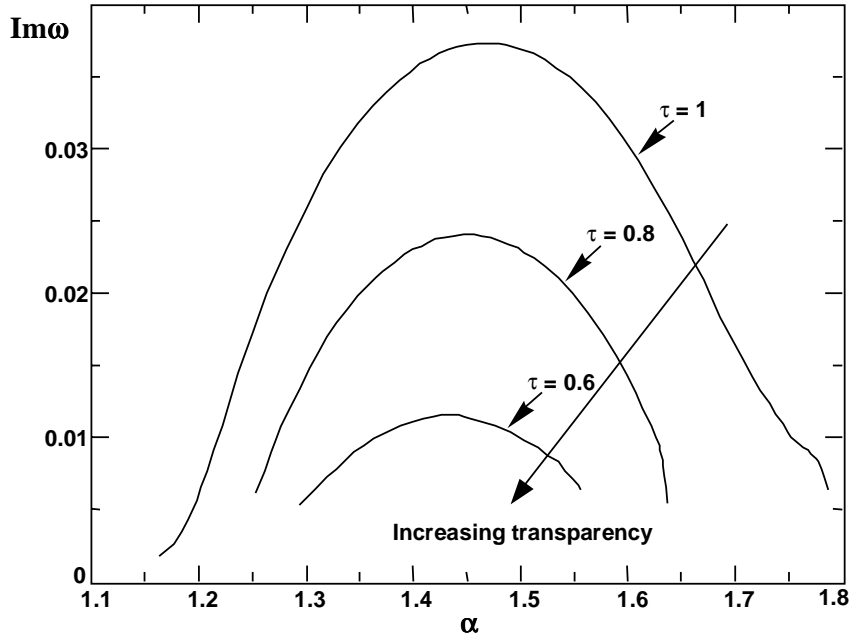


Figure 2.1: Plot of temporal growth rate of the second mode ($\text{Im}(\omega) = \text{Im}(\omega^*)$) versus wavenumber ($\alpha = \alpha^*$) with the wall reflection coefficient (τ) as a parameter. Decreasing the wall reflection coefficient is seen to have a strong damping effect on the growth rate; Mach number $M=6$, specific heat ratio $\gamma=1.4$, Prandtl number $Pr=0.72$, and wall temperature ratio $T_w^*/T_{aw}^*=0.2$ (typical of hypersonic vehicles). (Reproduced from Fedorov *et al.* [33])

and the following explicit form for the absorption coefficient can be obtained

$$A = -\frac{T^*(0)}{c^*} \sqrt{\frac{M^2 c^{*2}}{T^*(0)} - 1} \frac{1 - \tau}{1 + \tau}, \quad \text{Real}(A) < 0. \quad (2.10)$$

The original eigenvalue problem defined in Equations 2.2 - 2.4 using the absorption coefficient in Equation 2.10 was then solved using a temporal linear stability analysis. Figure 2.1 shows the results of the numerical integration for a flat plate boundary layer on a cool wall at different values of the reflection coefficient. Recall that for a temporal linear stability analysis the quantity $\text{Im}(\omega)$ is the growth rate of the wave with positive quantities identifying unstable exponential growth. This plot clearly shows the general trend that decreasing the reflection coefficient (*i.e.*, increasing the amount of absorption) tends to decrease the growth rate of the most unstable mode.

2.2.2 Viscous Linear Stability Analysis

The full parallel flow, viscous, compressible, two-dimensional boundary layer linear stability equations are significantly more complicated than the inviscid limit described above.

Once again, the detailed derivation of these equations is given in Mack [69]. As mentioned previously, it is not possible to simplify this case to a fully two-dimensional problem and it is necessary to consider three-dimensional disturbances of the form

$$[\tilde{u}, \tilde{v}, \tilde{w}, \tilde{p}, \tilde{\theta}]^T(x, y, t) = [u(y), v(y), w(y), p(y), \theta(y)]^T e^{j(\alpha x + \beta y - \omega t)}, \quad (2.11)$$

where α and β are the wavenumber components in the x and y directions, respectively. The final linearized normal-mode stability equations represent an 8th order system of differential equations that can be expressed in the form

$$\frac{d\bar{\mathbf{z}}}{dy} = \mathbf{S} \cdot \bar{\mathbf{z}}, \quad (2.12)$$

$$\bar{\mathbf{z}} = [u, \frac{du}{dy}, v, p, \theta, \frac{d\theta}{dy}, w, \frac{dw}{dy}]^T \quad (2.13)$$

where \mathbf{S} is an 8 x 8 matrix whose coefficients are functions of the mean velocity profiles, the displacement thickness, the Reynolds number, the Prandtl number, the ratio of specific heats, the parameters of a temperature-viscosity law, and the disturbance properties (ω , α , β). The boundary conditions for this problem are

$$u(0) = 0, w(0) = 0, \theta(0) = 0, v(0) = A p(0), \quad (2.14)$$

$$u(\infty) = v(\infty) = w(\infty) = \theta(\infty) = 0, \quad (2.15)$$

where A is the complex absorption coefficient given in the previous section. The eigenvalue problem 2.12 - 2.15 was solved by Fedorov and Malmuth using a spatial linear stability analysis. Figure 2.2 shows a plot of the growth rate versus Reynolds number for a particular frequency with the reflection coefficient as a parameter. Once again, the trend of strong stabilization with increasing absorption is observed. In fact, for this analysis, the disturbances were completely stabilized at all Reynolds numbers for $\tau < 0.5$.

2.2.3 Viscous Analysis with Porous Microstructure Boundary Conditions

The analysis described in the previous sections used a generic absorption coefficient that successfully demonstrated that ultrasonic absorption would, in principle, damp the growth of the second mode and delay transition. It did not, however, address the issue of how a

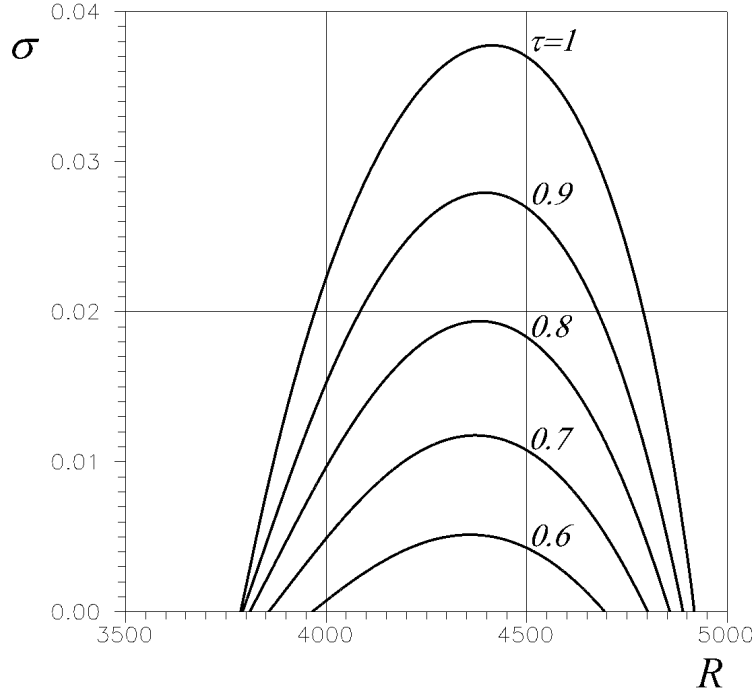


Figure 2.2: Plot of spatial growth rate of the second mode (σ) versus Reynolds number ($R = Re_{\delta^*} = \delta^* U_e \rho_e / \mu_e$) with the wall reflection coefficient (τ) as a parameter. As with the inviscid case, decreasing the wall reflection coefficient is seen to have a strong damping effect on the growth rate; $M=6$, $Pr=0.72$, $\gamma=1.4$, $F^* = \omega \mu_e / \rho_e U_e^2 = 2.78 \times 10^{-4}$, $T_w^*/T_{ad}^* = 0.2$. The viscosity (μ) was computed using a power law $\mu \sim T^{0.75}$. (Reproduced from Fedorov *et al.* [33])

specific surface could be constructed to perform this task. As mentioned earlier, the more significant innovation by Fedorov and Malmuth was to apply boundary conditions that were representative of a surface with specific microstructure. The idea of using a porous surface with equally spaced blind cylindrical microholes has its roots in architectural acoustics where similar surfaces with larger holes sized for audio wavelengths are often used to control the acoustics of concert halls and other similar facilities. The remainder of this section is used to rederive a new complex absorption coefficient A that is based on the specific proposed surface microstructure and to discuss the results of the linear stability analysis performed using this new boundary condition.

Significant theoretical work to develop the proper boundary conditions was previously done by Gaponov. In particular, Gaponov studied the effects of similar porosity in subsonic [34, 35] and low supersonic flows [36]. Recall that at such conditions, natural transition of the boundary layer is dominated by the unstable growth of the viscous Tollmien-Schlichting waves. In this case, Gaponov was examining the unstable growth of vortical disturbances generated by the porosity that became unstable due to a viscous mechanism.

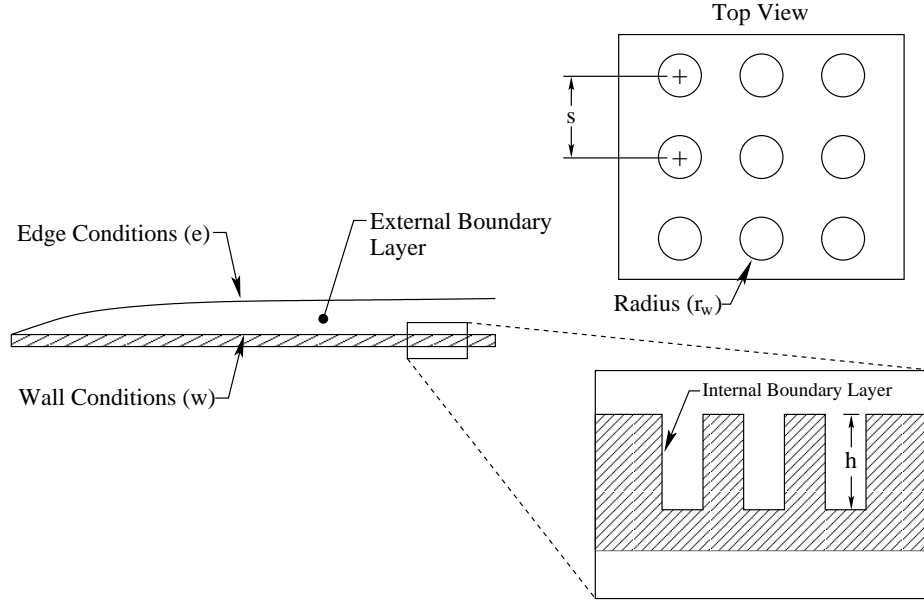


Figure 2.3: Schematic diagram showing the porous microstructure under consideration. The holes of radius r_w and depth h are arranged in a rectangular grid with a uniform spacing of s . The ‘external boundary layer’ refers to the overall boundary layer on the surface, while the ‘internal boundary layer’ refers to the boundary layer within a hole.

This is entirely different from the present theoretical analysis performed by Fedorov and Malmuth, which examines the effects of the porosity on the second mode which is an inviscid, acoustic mode. Despite the differences in the mean flow, the boundary conditions proposed by Gaponov are suitable for application to the current problem since the propagation of the disturbances within the porous wall is independent of the type of disturbance. Figure 2.3 shows a schematic of the porous microstructure under consideration and also defines some terms that will be used. Following the analysis of Gaponov, Fedorov and Malmuth applied the theory of sound wave propagation in thin, long tubes where the acoustic wavelength is significantly larger than the tube diameter. This problem is directly analogous to the practical problem of electrical transmission of current and voltage over long, lossy transmission lines, which has been studied extensively. In this case, the acoustic (or electric) field within the tube (transmission line) can be completely characterized by a propagation constant (Λ) and a characteristic impedance (Z_o). Borrowing from the electrical analogy, these two parameters can in turn be expressed in terms of a series impedance (Z) and a shunt admittance (Y) per unit length of tube (or transmission wire) through the following

relations

$$Z_o = \sqrt{\frac{Z}{Y}}, \quad \Lambda = \sqrt{ZY}. \quad (2.16)$$

The expressions for the specific impedance and specific admittance must be derived from the actual flow physics and are found to be

$$Z = -j\omega\rho_w \left[1 - \frac{2}{k_v} \frac{J_1(k_v)}{J_0(k_v)} \right]^{-1}, \quad (2.17)$$

$$Y = -\frac{j\omega}{\rho_w c_w^2} \left[1 + (\gamma - 1) \frac{2}{k_t} \frac{J_1(k_t)}{J_0(k_t)} \right], \quad (2.18)$$

where ρ_w is the mean density in the tube, c_w is the mean sound speed in the tube, γ is the ratio of specific heats, J_0 and J_1 are Bessel functions of the first kind, and the subscript w is used to denote quantities evaluated at the wall of the external surface (*i.e.*, at the input to the microhole). The arguments of the Bessel functions, k_v and k_t , are the ratios of the tube radius to the internal viscous and thermal boundary layer thicknesses, respectively, and can be shown to be

$$k_v = r_w \sqrt{\frac{j\omega\rho_w}{\mu_w}}, \quad k_t = r_w \sqrt{\frac{j\omega\rho_w C_p}{k_w}}, \quad (2.19)$$

where μ_w is the viscosity, k_w is the thermal conductivity and C_p is the specific heat at constant pressure. Note that the viscous and thermal boundary layer thicknesses are related through $k_t = k_v \sqrt{Pr}$, where Pr is the Prandtl number. All of the above equations are derived in detail from the fundamental flow physics and appropriate electrical circuit theory in Section 2.3. Using the relation

$$J_0(x) + J_2(x) = 2\frac{J_1(x)}{x}, \quad (2.20)$$

the following expressions can be obtained:

$$Z = j\omega\rho_w \frac{J_0(k_v)}{J_2(k_v)}, \quad (2.21)$$

$$Y = -\frac{j\omega}{\rho_w c_w^2} \left[\gamma + (\gamma - 1) \frac{J_2(k_t)}{J_0(k_t)} \right]. \quad (2.22)$$

Non-dimensionalizing the above equations using the external boundary layer displacement

thickness (δ^*) and the mean flow parameters at the edge of the external boundary layer, the following non-dimensional expressions can be obtained:

$$Z^* = \frac{j\omega^* J_0(k_v)}{T_w^* J_2(k_v)}, \quad (2.23)$$

$$Y^* = -j\omega^* M^2 \left[\gamma + (\gamma - 1) \frac{J_2(k_t)}{J_0(k_t)} \right], \quad (2.24)$$

$$k_v^* = r^* \sqrt{\frac{j\omega^* \rho_w^*}{\mu_w^*} Re_{\delta^*}}, \quad (2.25)$$

where Re_{δ^*} is the Reynolds number based on the external displacement thickness and external boundary layer edge conditions, and superscripts stars (*) are used to denote the quantities that have been non-dimensionalized. Once again, borrowing from the electrical analogy, it will be shown in Section 2.3.2 that the input impedance (Z_i) for the configuration under consideration (*i.e.*, blind microhole) is

$$Z_i^* = \frac{p^*(0)}{\bar{v}^*(0)} = -Z_o^* \coth(-\Lambda^* h^*), \quad (2.26)$$

where $p^*(0)$ is the pressure at the entrance to the cylindrical microhole (*i.e.*, it is equal to the pressure at the external wall, p_w^*), $\bar{v}^*(0)$ is the average vertical velocity at the entrance to the cylindrical microhole, and $h^* = h/\delta^*$ is the non-dimensional length of the cylindrical microhole. It is this input impedance (or rather its reciprocal which is the input admittance) that is the basis for the absorption coefficient (A) required for the boundary condition to solve the original eigenvalue problem. The above analysis was done for a single hole in the porous surface. The result is extended to the overall porous surface by averaging the vertical velocity $\bar{v}^*(0)$ over the surface area using

$$v^*(0) = n \bar{v}^*(0), \quad (2.27)$$

where n is the porosity defined as the ratio of the hole volume to the total volume:

$$n = \frac{Volume_{Holes}}{Volume_{Total}} = \frac{\pi r_w^2}{s^2}, \quad (2.28)$$

where s is the hole spacing as defined in Figure 2.3. The absorption coefficient then becomes

$$A = \frac{n}{Z_i^*} = \frac{n\bar{v}^*(0)}{p^*(0)} = -\frac{n}{Z_o^*} \tanh(-\Lambda^*h^*). \quad (2.29)$$

This is the final expression used in the boundary condition (Equation 2.14) to solve the eigenvalue problem. It is interesting to note that this equation can be further simplified in the case of a deep microhole ($h^* \rightarrow \infty$) to

$$A = -\frac{n}{Z_o^*}. \quad (2.30)$$

A similar analysis following the work of Stinson and Champoux [120] was also performed to develop the thermal admittance for use in a thermal boundary condition. For all the cases considered by Fedorov and Malmuth, it was found that thermal perturbations had very little effect on the growth rates. For this reason, the development of the thermal admittance is not included here and the reader is referred to Fedorov and Malmuth [32] for more details.

Figure 2.4 shows a plot of the growth rate versus Reynolds number for a fixed frequency with non-dimensional hole radius (r_w^*) as a parameter. Increasing r_w^* is equivalent to increasing the absorption coefficient and, once again, a strong stabilizing effect can be observed. One of the main parameters affecting the stabilizing effect is the porosity (n). Figure 2.5a is a plot of the maximum growth rate versus the porosity and shows the strong stabilizing effect as porosity is increased. It should be noted that this linear stability analysis assumes that the hole diameter is small enough that the holes do not prematurely trip the boundary layer. For a practical experiment or flight vehicle, there is clearly an optimum hole size which is large enough to maximize the stabilizing effect, yet small enough that the holes do not act as surface roughness to trip the boundary layer. Another study examining the effect of the depth of the microholes was also performed and its results are summarized in Figure 2.5b which shows the growth rate as a function of the non-dimensional hole depth (h^*). Two things should be noted. First, the growth rate quickly approaches a limiting value for $h^* \geq 0.3$. Second, there is an optimum thickness ($h^* \simeq 0.12$) where the porous surface completely damps the disturbances since the reflected wave from the bottom of the pore is in counter phase with the incident wave. This latter effect is strongly frequency dependent and for the sake of robustness for a practical flight vehicle, it is better to rely on the limiting

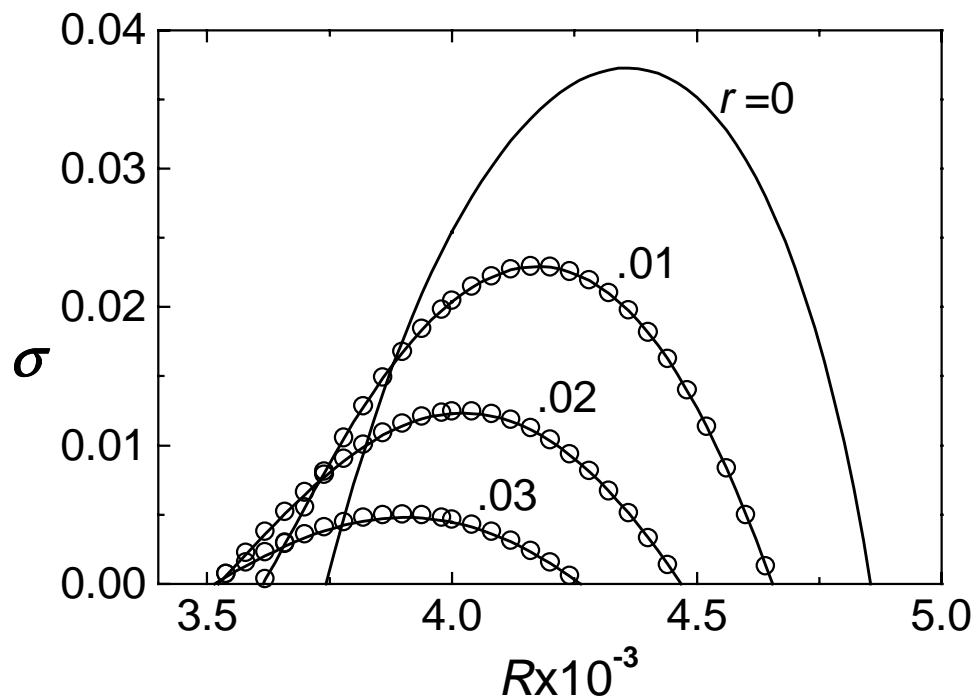


Figure 2.4: Plot of spatial growth rate of the second mode (σ) versus Reynolds number ($R = Re_{\delta^*} = \delta^* U_e \rho_e / \mu_e$) with non-dimensional radius (r) as a parameter. The solid lines correspond to calculations using both the pressure and thermal admittance boundary conditions and the circles correspond to calculations with the thermal admittance taken to be zero. The case $r = 0$ corresponds to a solid wall (both pressure and thermal admittance are zero). Increasing the radius of the holes (and therefore the absorption coefficient) is seen to have a strong damping effect on the growth rate; $F^* = 2.8 \times 10^{-4}$, $n = 0.5$, $M=6$, $Pr=0.71$, $\gamma=1.4$, $T_w^*/T_{ad}^*=0.2$ and $h^* \rightarrow \infty$. (Reproduced from Fedorov *et al.* [32])

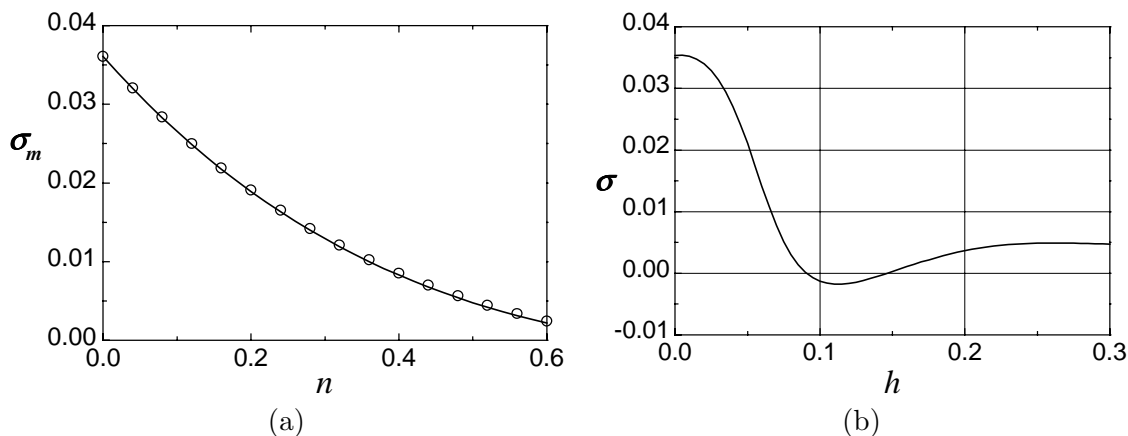


Figure 2.5: (a) Plot of the maximum spatial growth rate (σ_m) of the second mode versus the porosity (n); $F^* = 2.8 \times 10^{-4}$, $M=6$, $Pr=0.71$, $\gamma=1.4$, $T_w^*/T_{ad}^*=0.2$, $r^*=0.03$, and $Re_{\delta^*} = 4000$. Increasing the porosity is seen to increase the stabilizing effect. (b) Plot of spatial growth rate (σ) of the second mode versus the non-dimensional depth of the microholes ($h = h^*$); all parameters are the same as above, except n is fixed at 0.4. The damping is seen to be an optimum at $h^* = 0.12$ and rapidly approaches a limiting value for $h^* \geq 0.3$. (Reproduced from Fedorov *et al.* [32])

value and have deeper holes. As indicated by Fedorov and Malmuth [32], the stabilizing effect provided by the porous surface was found to be very robust. In particular, it was found to be effective regardless of the disturbance amplitude and phase distributions in space and time. Furthermore, it was found that it was even more effective at small wall temperature ratios (*i.e.*, cold wall case) typical of actual hypervelocity flight conditions. Calculations using e^N -methods indicated that the porous surface was able to increase the transition Reynolds number by more than three times its value without porosity. Such dramatic delays in transition by a relatively simple passive control scheme would be extremely valuable in reducing heating rates experienced by hypervelocity flight vehicles.

2.3 Flow Physics

The linear stability analysis performed by Fedorov and Malmuth showed great promise for the proposed boundary layer control scheme. The analysis, however, did not give insight into the actual physics of the flow within the porous layer and the manner in which it damped the acoustic perturbations responsible for transition. The boundary conditions were developed using an electrical analogy for propagation of an acoustic wave in a long cylindrical tube which was then averaged over the entire surface to simulate the effect of the many parallel cylindrical holes that made up the porous surface. In order to do this, however, it is important to understand the basis for using the analogy. In the sections below, the electric transmission line equations are derived and the problem of acoustic propagation in a tube is shown to reduce to the electrical equivalent. From this electrical analogy, the details of the flow within each cylindrical microhole can be examined to gain an understanding of the actual mechanism by which the damping occurs. Ultimately, this analogy is related to the more fundamental problem of the attenuation of a single acoustic wave propagating in an infinitely long tube.

2.3.1 Acoustic Propagation in a Tube of Finite Length

Each hole within the porous surface can be modeled as the case of an oscillating piston at the input of a long, thin tube whose far end is closed and contains a lossy medium as shown in Figure 2.6. This situation is similar to an organ pipe and an infinite number of acoustic waves are generated. These waves will travel back and forth between the closed

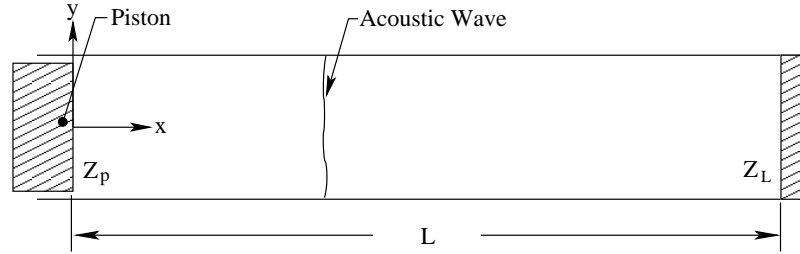


Figure 2.6: Schematic diagram showing the acoustic problem to be solved. A vibrating piston generates acoustic waves which travel back and forth between both ends of the tube. The piston face has an impedance of Z_p and the tube end has an impedance of Z_L .

tube end which has an impedance Z_L and the piston face which has an impedance of Z_p . A critical assumption made in this analysis is that the tube diameter must be much smaller than the acoustic wavelength. The exact definition of ‘small’ will be given in Section 2.3.7. Also, this analysis assumes plane acoustic waves; however, it is not necessary to make this assumption. It can be shown that for tubes of radius much smaller than the acoustic wavelength, any non-uniformities will quickly smooth out and the resulting wave will converge to a plane wave [60, 99]. For a cylindrical rigid-walled acoustic waveguide, Kinsler [60] indicates that all waves with angular frequency $\omega < 1.84c/r_w$ are evanescent standing waves that are attenuated exponentially. This condition can be re-expressed as $r_w < 1.84\lambda/(2\pi)$. Furthermore, it can be shown that under such conditions, the pressure across the tube is essentially constant.

Before continuing further, it is useful to mention an important difference between acoustic propagation in an inviscid medium as compared to a viscous medium. When considering the propagation of a plane acoustic wave in the former, it is common to derive the following relation:

$$P = \pm \rho_o c_o \dot{\xi}, \quad (2.31)$$

where P is pressure, ρ_o is equilibrium density of the medium, c_o is the adiabatic speed of sound, $\dot{\xi}$ is the particle velocity and the \pm is used to denote the forward and backward waves. In this case, the quantity $\rho_o c_o$ is often described as being the specific acoustic impedance. In order to include the effects of attenuation, however, the above equation needs to be modified since the relaxation (viscous or thermal) of the medium will introduce a phase lag ($\phi' - \phi$) between the pressure and the particle velocity. The above equation is then modified to be

$$P = \pm \rho_o c_o \dot{\xi} e^{-j(\phi' - \phi)} = W \dot{\xi}, \quad (2.32)$$

where $W = \rho_o c_o e^{-j(\phi' - \phi)}$ is the newly defined specific acoustic impedance. A proper derivation of the above can be found in any acoustics textbook such as Kinsler *et al.* [60], Morse and Ingard [79] or Pierce [87] and typically involves solving some variation of a lossy Helmholtz equation.

Closely following Rschevkin [99], the solution to the acoustic problem under consideration will contain travelling waves in both directions and the particle velocity can be expressed as

$$\dot{\xi}(x, t) = [\dot{\xi}^+(x) + \dot{\xi}^-(x)]e^{-j\omega t} = (ae^{-\Lambda x} + be^{\Lambda x})e^{-j\omega t}, \quad (2.33)$$

where a and b are constants to be determined, $\dot{\xi}^+$ and $\dot{\xi}^-$ are the forward and backward waves, respectively, ω is the angular frequency, t is time, $e^{-j\omega t}$ is the assumed time dependence, and Λ is the complex propagation constant. The pressure can then be expressed as

$$P(x, t) = W[ae^{-\Lambda x} - be^{\Lambda x}]e^{-j\omega t}. \quad (2.34)$$

Using the boundary conditions

$$Z_p \dot{\xi}_i + SP_i = \psi_i \quad (\text{at } x = 0), \quad (2.35)$$

$$Z_L \dot{\xi}_L = SP_L \quad (\text{at } x = L), \quad (2.36)$$

where subscripts i and L are used to denote quantities at the tube entrance ($x = 0$) and tube end ($x = L$), respectively, S is the tube cross-sectional area and $\psi_i = \psi e^{-j\omega t}$ is the external forcing function driving the piston, a and b can be determined to be

$$a = \frac{Z_L + WS}{\Delta} e^{\Lambda L} \psi, \quad b = -\frac{Z_L - WS}{\Delta} e^{-\Lambda L} \psi, \quad (2.37)$$

$$\Delta = 2[Z_p Z_L + (WS)^2] \sinh(\Lambda L) + 2WS(Z_p + Z_L) \cosh(\Lambda L). \quad (2.38)$$

The resulting equations are

$$\dot{\xi}(x, t) = [(Z_L + WS)e^{\Lambda(L-x)} - (Z_L - WS)e^{-\Lambda(L-x)}] \frac{\psi_i}{\Delta}, \quad (2.39)$$

$$P(x, t) = W[(Z_L + WS)e^{\Lambda(L-x)} + (Z_L - WS)e^{-\Lambda(L-x)}] \frac{\psi_i}{\Delta}. \quad (2.40)$$

Evaluating the above at $x = L$, one obtains

$$\dot{\xi}_L = \frac{2WS}{\Delta}\psi_i, \quad P_L = \frac{2Z_L W}{\Delta}\psi_i. \quad (2.41)$$

Evaluating the same equations at $x = 0$ and re-expressing the exponentials in terms of hyperbolic functions, one obtains

$$\dot{\xi}_i = \left[\frac{2Z_L}{\Delta} \sinh(\Lambda L) + \frac{2WS}{\Delta} \cosh(\Lambda L) \right] \psi_i, \quad (2.42)$$

$$P_i = W \left[\frac{2WS}{\Delta} \sinh(\Lambda L) + \frac{2Z_L}{\Delta} \cosh(\Lambda L) \right] \psi_i. \quad (2.43)$$

Combining Equations 2.41 - 2.43, one can finally express the input pressure and particle velocity in terms of the quantities at the tube end:

$$\dot{\xi}_i = \cosh(\Lambda L) \dot{\xi}_L + \frac{1}{W} \sinh(\Lambda L) P_L, \quad (2.44)$$

$$P_i = W \sinh(\Lambda L) \dot{\xi}_L + \cosh(\Lambda L) P_L. \quad (2.45)$$

An examination of the above equations reveals that they are in the form

$$\dot{\xi}_i = C_1 \dot{\xi}_L + C_2 P_L, \quad (2.46)$$

$$P_i = C_3 \dot{\xi}_L + C_4 P_L, \quad (2.47)$$

where $C_1 = C_4 = \cosh(\Lambda L)$, $C_2 = (1/W) \sinh(\Lambda L)$, and $C_3 = W \sinh(\Lambda L)$. Systems of equations with this form are known as four-poles and are used extensively in electrical transmission line theory. In particular, since $C_1 = C_4$ and $C_1 C_4 - C_2 C_3 = 1$, this is a symmetric four-pole which means that it is reversible (*i.e.*, the output quantities can be expressed in terms of the input quantities by simply switching the subscripts in the above equations). This reversibility feature can be demonstrated rigorously by straightforward algebraic manipulations and a suitable change of sign ($\dot{\xi}_i = -\dot{\xi}_i$ and $\dot{\xi}_L = -\dot{\xi}_L$) in order to take into account the change in direction of the wave propagation. This reduced form of the symmetric four-pole will be used to derive some interesting results, but first it is useful to pursue the apparent analogy with electrical transmission lines.

2.3.2 Electric Transmission Line Theory

For most electrical circuits, the wavelengths of the voltage and current are much longer than the physical size of any actual device and the wave nature can be neglected. This can be readily seen if one considers that for typical 60 Hz electrical power grids, the wavelength is approximately 5000 km. For power transmission lines, however, the length of the conducting power line becomes of the same order as the wavelength and it is no longer possible to ignore wave effects. The additional fact that the wavelength is much larger than the cross-sectional diameter of the wire gives reason to believe that this would be an appropriate analogy for the problem of an acoustic wave propagating in a long, thin tube whose diameter is much smaller than the acoustic wavelength. A detailed derivation and discussion of the standard transmission line equations using basic circuit theory can be found in Karakash [53]. A modified version of this derivation is presented below. Karakash noted that these equations can also be derived from the more fundamental Maxwell equations, although it is unnecessary for the purposes of the present work.

The standard transmission line formalism begins by assuming that a differential segment of the transmission line can be modeled using the circuit diagram shown in Figure 2.7. This is known as a lump-mass model since the electrical properties which are normally distributed along the entire length of the transmission line have been lumped into discrete electrical elements in a transmission line segment of differential length. The series resistance (R) represents the actual resistivity of the wire, the series inductance (L) models phase shifts due to magnetic flux interactions, the shunt conductivity (G) is used to represent leakage current across the dielectric separating the two conductors and the shunt capacitance (C) is used to represent phase shifts due to electric field interactions. The R and G terms are pure resistances and are responsible for losses (attenuation of the signal), while the L and C terms are pure reactances responsible for phase shifts. All of the above quantities are expressed per unit length of transmission wire. Applying Kirchhoff's current and voltage laws to the circuit diagram, one obtains

$$i(x + dx, t) - i(x, t) = -(G + j\omega C) v(x, t) dx, \quad (2.48)$$

$$v(x + dx, t) - v(x, t) = -(R + j\omega L) i(x, t) dx, \quad (2.49)$$

where i is current, v is voltage, k is the wavenumber, ω is angular frequency, t is time, x is the

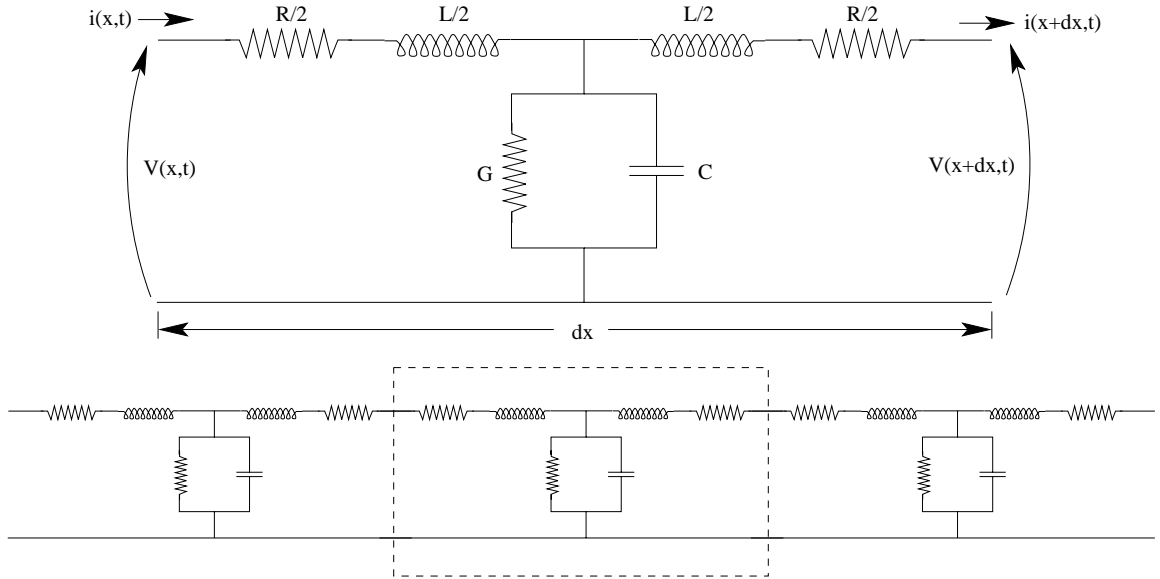


Figure 2.7: The bottom figure shows the circuit diagram used to represent an electrical transmission line. A differential segment called a ‘T-section’ is removed from the chain and analyzed in order to derive the transmission line equations. The electrical elements (R , L , G , C) are used to represent the various properties and are given per unit length of wire.

distance along the direction of propagation and dx is the unit length of transmission wire. Although not explicitly stated, a time dependence of the form $e^{-j\omega t}$ is assumed throughout the derivation. Rearranging and taking the limit $dx \rightarrow 0$, the following differential equations are obtained:

$$\frac{\partial i}{\partial x} = -(G + j\omega C)v = -Yv, \quad (2.50)$$

$$\frac{\partial v}{\partial x} = -(R + j\omega L)i = -Zi, \quad (2.51)$$

where $Z = R + j\omega L$ is the series impedance and $Y = G + j\omega C$ is the shunt admittance. Differentiating Equation 2.51 and substituting for $\partial i/\partial x$ from Equation 2.50 (and vice versa for the current), one can obtain two uncoupled, second order differential equations:

$$\frac{\partial^2 i}{\partial x^2} = \Lambda^2 i, \quad \frac{\partial^2 v}{\partial x^2} = \Lambda^2 v, \quad (2.52)$$

where $\Lambda^2 = (R + j\omega L)(G + j\omega C) = ZY$. Clearly, the solutions are

$$i = i^+ e^{\Lambda x} + i^- e^{-\Lambda x}, \quad (2.53)$$

$$v = v^+ e^{\Lambda x} + v^- e^{-\Lambda x}, \quad (2.54)$$

where v^+ , v^- , i^+ and i^- are the arbitrary constants to be determined. Differentiating Equation 2.54 and using it with Equation 2.51, one can show that

$$i^+ = -\frac{\Lambda}{Z}v^+, \quad i^- = \frac{\Lambda}{Z}v^-. \quad (2.55)$$

Substituting the above relations into Equations 2.53 and 2.54 and evaluating them at $x = L$, where L is the length of the transmission wire, one obtains

$$I_L = -\frac{\Lambda}{Z}v^+e^{\Lambda L} + \frac{\Lambda}{Z}v^-e^{-\Lambda L}, \quad (2.56)$$

$$V_L = v^+e^{\Lambda L} + v^-e^{-\Lambda L}, \quad (2.57)$$

where I_L and V_L are the current and voltage evaluated at the end of the transmission line segment, respectively. Manipulate Equations 2.57 and 2.56, to solve for v^+ and v^- to obtain

$$v^+ = -\frac{1}{2} \left(\sqrt{\frac{Z}{Y}}I_L - V_L \right) e^{-\Lambda L}, \quad v^- = \frac{1}{2} \left(\sqrt{\frac{Z}{Y}}I_L + V_L \right) e^{\Lambda L}. \quad (2.58)$$

Substituting back into Equations 2.53 and 2.54, the final equations can be written as

$$i(x, t) = \frac{1}{2} \left[\left(I_L + \sqrt{\frac{Y}{Z}}V_L \right) e^{\Lambda(L-x)} + \left(I_L - \sqrt{\frac{Y}{Z}}V_L \right) e^{-\Lambda(L-x)} \right] e^{-j\omega t}, \quad (2.59)$$

$$v(x, t) = \frac{1}{2} \left[\left(\sqrt{\frac{Z}{Y}}I_L + V_L \right) e^{\Lambda(L-x)} + \left(-\sqrt{\frac{Z}{Y}}I_L + V_L \right) e^{-\Lambda(L-x)} \right] e^{-j\omega t}, \quad (2.60)$$

where the time dependence of $e^{-j\omega t}$ has been explicitly stated here for completeness. From these equations, it is clear that the entire system is characterized by $\Lambda = \sqrt{ZY}$ and $Z_o = \sqrt{Z/Y}$ which are termed the propagation constant and characteristic impedance, respectively. Re-expressing the above equations in terms of hyperbolic functions and evaluating them at $x = 0$, the equations become

$$I_i = \cosh(\Lambda L) I_L + \frac{1}{Z_o} \sinh(\Lambda L) V_L, \quad (2.61)$$

$$V_i = Z_o \sinh(\Lambda L) I_L + \cosh(\Lambda L) V_L, \quad (2.62)$$

where I_i and V_i are the current and voltage at the input. An examination of the above

equations reveals that they are in the form

$$I_i = C_1 I_L + C_2 V_L, \quad (2.63)$$

$$V_i = C_3 I_L + C_4 V_L, \quad (2.64)$$

where $C_1 = C_4 = \cosh(\Lambda L)$, $C_2 = (1/Z_o) \sinh(\Lambda L)$, and $C_3 = Z_o \sinh(\Lambda L)$. Comparing with Equations 2.46 and 2.47, it is clear that the above equations are identical to those derived for the case of acoustic propagation in a tube. This reduced form of the symmetric four-pole is useful for deriving some interesting results. For example, the input impedance (Z_i) can be expressed as

$$Z_i = \frac{V_i}{I_i} = \frac{C_3 I_L + C_4 V_L}{C_1 I_L + C_2 V_L} = \frac{C_3 + Z_L C_4}{C_1 + Z_L C_2}, \quad (2.65)$$

where $Z_L = V_L/I_L$ is the impedance at the end of the transmission line segment. Substituting the appropriate values into the above equation results in

$$Z_i = \frac{V_i}{I_i} = \frac{Z_o \sinh(\Lambda L) + Z_L \cosh(\Lambda L)}{\cosh(\Lambda L) + (Z_L/Z_o) \sinh(\Lambda L)} = \frac{Z_o \tanh(\Lambda L) + Z_L}{1 + (Z_L/Z_o) \tanh(\Lambda L)}. \quad (2.66)$$

Consider an open circuit at the end of the transmission line segment (*i.e.*, $Z_L \rightarrow \infty$) in which case Equation 2.66 reduces to

$$Z_i = Z_o \coth(\Lambda L). \quad (2.67)$$

Similarly, the case of a short circuit (*i.e.*, $Z_L = 0$) results in

$$Z_i = Z_o \tanh(\Lambda L). \quad (2.68)$$

Another result can be obtained by considering the condition that needs to be satisfied in order for the transmission line segment to be impedance matched (*i.e.*, $Z_i = Z_L$). Using Equation 2.65, it can be easily shown that the condition is

$$Z_i = Z_L = \sqrt{\frac{C_3}{C_2}} = \sqrt{\frac{Z_o \sinh(\Lambda L)}{(1/Z_o) \sinh(\Lambda L)}} = Z_o. \quad (2.69)$$

This provides an interpretation of Z_o which can now be seen to be the required impedance

for an impedance matched transmission line. This interpretation can be taken one step further by noting that impedance matching eliminates all wave reflections and that an electric source behaves as if the circuit were infinitely long in such conditions. In essence, this implies that the characteristic impedance is the input impedance of an infinitely long transmission line.

2.3.3 Electrical Analogy

Comparing Equations 2.46 and 2.47 with Equations 2.63 and 2.64, repeated below, it is clear that there is a direct analogy between the acoustic problem to be solved and the problem of the electrical transmission line.

Acoustic Equations	Electrical Equations
$\dot{\xi}_i = \cosh(\Lambda L) \dot{\xi}_L + \frac{1}{W} \sinh(\Lambda L) P_L,$	$I_i = \cosh(\Lambda L) I_L + \frac{1}{Z_o} \sinh(\Lambda L) V_L,$
$P_i = W \sinh(\Lambda L) \dot{\xi}_L + \cosh(\Lambda L) P_L,$	$V_i = Z_o \sinh(\Lambda L) I_L + \cosh(\Lambda L) V_L.$

In this case, the particle velocity is directly analogous to the current and the pressure is directly analogous to the voltage. Furthermore, the specific acoustic impedance of the medium (W) is seen to be equivalent to the characteristic impedance of the transmission line (Z_o). The relevant results from the transmission line theory can be immediately applied. In fact, the value of the electrical analogy is now observed since it provides the means by which W and Λ will be estimated. Recall from the transmission line theory that the problem is completely specified by the characteristic impedance and the propagation constant, therefore,

$$W = Z_o = \sqrt{\frac{Z}{Y}}, \quad \Lambda = \sqrt{ZY}, \quad (2.70)$$

where $Z = R + j\omega L$ is the series impedance and $Y = G + j\omega C$ is the shunt admittance. This implies that the specific acoustic impedance can be estimated by determining the equivalent series impedance and shunt admittance for the acoustic propagation problem. Furthermore, the special case of the transmission line terminated in an open circuit (Equation 2.67) can be used to obtain

$$A = \frac{1}{Z_i} = \frac{1}{Z_o} \tanh(\Lambda L) = \frac{1}{W} \tanh(\Lambda L) \quad (2.71)$$

where A is the input admittance. This is exactly the admittance boundary condition used by Fedorov and Malmuth in Equation 2.26. The cylindrical hole with a solid wall at its end considered by Fedorov and Malmuth is seen to be equivalent to an open circuit in the electrical analogy. Finally, the case of the impedance matched transmission line showed that $Z_i = Z_o$, therefore

$$A = \frac{1}{Z_i} = \frac{1}{Z_o} = \frac{1}{W}. \quad (2.72)$$

Note that, once again, this is exactly the admittance condition used by Fedorov and Malmuth for the limiting case of an infinitely deep hole.

At this point, it is interesting to discuss the details of the analogy in order to gain a better understanding of the exact comparisons being made. Recall from the standard transmission line theory that $Z = R + j\omega L$ and $Y = G + j\omega C$. In the case of the acoustical problem, the series impedance is related to the kinetic energy and the longitudinal wave motion in the tube. The shunt admittance, on the other hand, is related to the potential energy and the radial wave motion. The R and G terms represent the losses and attenuate the amplitude of the wave, while the L and C terms represent storage of energy and introduce phase shifts between the pressure and velocity. The L is referred to as the acoustical inertance. Its effect is to increase the effective mass of the system and is therefore associated with the storage of kinetic energy. It opposes changes in the velocity analogous to the manner in which inductance opposes changes in current in an electrical system. The C is known as the acoustical capacitance and has the effect of opposing changes in the applied pressure. It is related to the compression of the gas and is therefore associated with storage of potential energy. The electrical analogy is summarized in Table 2.1. An excellent discussion of the various electrical, mechanical and acoustical analogies that can be made for a variety of systems can be found in Olson [81, 82]. The electrical analogy is seen to be very powerful; however, it remains to derive expressions for the series impedance and the shunt admittance. This will be done in the following sections from the fundamental understanding of the propagation of an acoustic wave in a tube.

2.3.4 Derivation of Series Impedance (Z)

The original derivation of the series specific impedance per unit length is found in Crandall [20] and is outlined here. Crandall considered the case of oscillations of a viscous

Table 2.1: Table summarizing the electrical analogy.

Element	Electrical Property	Equivalent Acoustic Property	Effect
R	Resistance of wire.	Viscous dissipation.	Amplitude attenuation.
L	Magnetic flux interactions.	Inertia of fluid. (Kinetic energy storage)	Phase shift.
G	Leakage current across dielectric.	Heat conduction to walls.	Amplitude attenuation.
C	Electric flux interactions.	Fluid compression. (Potential energy storage)	Phase shift.

fluid in a cylindrical tube with a pressure gradient, but neglecting thermal effects. His analysis is very similar to steady Poiseuille flow in liquids, with the difference being the addition of a term to take into account the inertia of the oscillating fluid mass. The equation of motion is derived by performing a force balance on an annular ring of fluid of volume $2\pi r dr dx$ in the direction of the axis of the tube. The driving force due to the pressure gradient is

$$F_p = -\frac{\partial p}{\partial x} 2\pi r dr dx, \quad (2.73)$$

where p is pressure, x is the direction of propagation, r is the radial direction, dr and dx are the radial and axial lengths of a differential volume element, respectively. The reactance due to the inertia of the fluid is

$$F_I = -j\omega \dot{\xi} \rho_o 2\pi r dr dx, \quad (2.74)$$

where ω is the angular frequency of vibration of the fluid and ρ_o is the equilibrium density. The net shear force due to the negative velocity gradient in the radial direction is

$$F_v = \frac{\partial}{\partial r} \left(2\pi r dx \mu \frac{\partial \dot{\xi}}{\partial r} \right) dr, \quad (2.75)$$

where $\dot{\xi}$ is the particle velocity, μ is the viscosity (assumed constant), and $\partial \dot{\xi} / \partial r$ is a negative quantity. The resulting force balance equation is

$$F_I = F_p + F_v \quad (2.76)$$

$$-j\omega \rho_o \dot{\xi} = -\frac{\partial p}{\partial x} + \frac{\mu}{r} \frac{\partial}{\partial r} \left(r \frac{\partial \dot{\xi}}{\partial r} \right), \quad (2.77)$$

which can be expressed as

$$\left[\frac{\partial^2}{\partial r^2} + \frac{1}{r} \frac{\partial}{\partial r} + r_v^2 \right] \dot{\xi} = \frac{1}{\mu} \frac{\partial p}{\partial x}, \quad r_v^2 = \frac{j\omega\rho_o}{\mu}. \quad (2.78)$$

The solution given by Crandall is

$$\dot{\xi} = \frac{1}{\mu r_v^2} \frac{\partial p}{\partial x} + C J_0(r_v r), \quad (2.79)$$

where J_0 is the Bessel function of the first kind of order zero. The arbitrary constant C can be determined by applying the boundary condition that the particle velocity is zero at the tube wall (*i.e.*, $\dot{\xi}(r_w) = 0$). The resulting expression is

$$\dot{\xi} = \frac{1}{j\omega\rho_o} \frac{\partial p}{\partial x} \left[1 - \frac{J_0(r_v r)}{J_0(r_v r_w)} \right]. \quad (2.80)$$

In order to calculate the impedance, it is desirable to use the average velocity over the cross-section

$$\bar{\dot{\xi}} = \frac{1}{\pi r_w^2} \int_0^{r_w} \dot{\xi} 2\pi r dr = \frac{1}{j\omega\rho_o} \frac{\partial p}{\partial x} \left[1 - \frac{2}{r_w^2} \int_0^{r_w} r \frac{J_0(r_v r)}{J_0(r_v r_w)} dr \right]. \quad (2.81)$$

The integral containing the Bessel function can be evaluated using the property

$$\int_0^a x J_0(x) dx = a J_1(a), \quad (2.82)$$

resulting in the final equation for the average particle velocity

$$\bar{\dot{\xi}} = \frac{1}{j\omega\rho_o} \frac{\partial p}{\partial x} \left[1 - \frac{2}{r_v r_w} \frac{J_1(r_v r_w)}{J_0(r_v r_w)} \right]. \quad (2.83)$$

Finally, the desired specific acoustic impedance per unit length is

$$Z = \frac{\partial p / \partial x}{\bar{\dot{\xi}}} = j\omega\rho_o \left[1 - \frac{2}{k_v} \frac{J_1(k_v)}{J_0(k_v)} \right]^{-1}, \quad (2.84)$$

where $k_v = r_v r_w$ as defined in Equation 2.19. Note that $\partial p / \partial x$ is used in the definition of Z (instead of p) since it is desired to obtain the specific impedance *per unit length*. This is the same as Equation 2.17 with the difference of a sign due to the opposite tube axis

directions (Fedorov assumes positive axis going outside the tube, while the present analysis has the positive axis going inside the tube).

It should be noted that, as expected, the above can be determined directly from the momentum equation as follows. The momentum equation is

$$\rho \left[\frac{\partial \dot{\boldsymbol{\xi}}}{\partial t} + (\dot{\boldsymbol{\xi}} \cdot \nabla) \dot{\boldsymbol{\xi}} \right] = -\nabla p + \rho \mathbf{B} + \nabla \cdot \boldsymbol{\tau}, \quad \boldsymbol{\tau} = \mu_2 (\nabla \cdot \dot{\boldsymbol{\xi}}) I + \mu \text{def} \dot{\boldsymbol{\xi}}, \quad (2.85)$$

where ρ is density, $\dot{\boldsymbol{\xi}}$ is velocity, p is the pressure, \mathbf{B} is the body force term, $\boldsymbol{\tau}$ is the stress tensor, μ_2 is the second coefficient of viscosity, μ is the dynamic viscosity, I is the identity matrix, and $\text{def} \dot{\boldsymbol{\xi}}$ is the deformation tensor. Boldface is used to denote vector quantities. Noting that $\nabla \cdot \text{def} \dot{\boldsymbol{\xi}} = \nabla(\nabla \cdot \dot{\boldsymbol{\xi}}) + \nabla^2 \dot{\boldsymbol{\xi}}$, then

$$\nabla \cdot \boldsymbol{\tau} = (\mu_2 + \mu) \nabla(\nabla \cdot \dot{\boldsymbol{\xi}}) + \mu \nabla^2 \dot{\boldsymbol{\xi}}. \quad (2.86)$$

Linearizing the momentum equation, ignoring the body force terms, and substituting the above expression for $\nabla \cdot \boldsymbol{\tau}$, one obtains

$$\rho_o \frac{\partial \dot{\boldsymbol{\xi}}}{\partial t} = -\nabla p + (\mu_2 + \mu) \nabla(\nabla \cdot \dot{\boldsymbol{\xi}}) + \mu \nabla^2 \dot{\boldsymbol{\xi}}, \quad (2.87)$$

where the quantities now represent the perturbation quantities and the subscript o is used to represent the equilibrium values. Noting that the momentum flux in the radial direction is negligible, it is sufficient to only consider the momentum equation in the x direction, which is

$$\rho_o \frac{\partial \dot{\xi}}{\partial t} = -\frac{\partial p}{\partial x} + (\mu_2 + \mu) \frac{\partial^2 \dot{\xi}}{\partial x^2} + \mu \left[\frac{\partial^2 \dot{\xi}}{\partial x^2} + \frac{1}{r} \frac{\partial}{\partial r} \left(r \frac{\partial \dot{\xi}}{\partial r} \right) \right], \quad (2.88)$$

where $\dot{\xi}$ is now the particle velocity in the x direction. Noting that the x scale is the wavelength of the acoustic wave which is assumed large, then the $\partial^2 \dot{\xi} / \partial x^2$ can be neglected. Furthermore, assuming a time dependence for the velocity of the form $\dot{\xi} = \dot{\xi} e^{-j\omega t}$, then the above reduces to

$$-\rho_o j \omega \dot{\xi} = -\frac{\partial p}{\partial x} + \frac{\mu}{r} \frac{\partial}{\partial r} \left(r \frac{\partial \dot{\xi}}{\partial r} \right), \quad (2.89)$$

which is the same as Equation 2.77.

2.3.5 Derivation of Shunt Admittance (Y)

The derivation of the specific shunt admittance per unit length was performed independently by Daniels [22] and Zwikker and Kosten [137]. The derivations considered periodic compression waves travelling in the axial direction of a cylindrical tube and modeled the resulting heat generation due to the compressions and subsequent radial conduction to the boundaries. Viscous effects were neglected and thermal gradients along the axial direction were also ignored. Once again the pressure across the tube was assumed constant since the tube radius is much smaller than the acoustic wavelength. Furthermore, the pressure gradient along the tube axis ($\partial p/\partial x$) can be shown to be zero. The linearized acoustic equation of continuity is

$$\nabla \cdot \dot{\boldsymbol{\xi}} = -\frac{\partial s}{\partial t}, \quad (2.90)$$

where $\dot{\boldsymbol{\xi}}$ is the particle velocity, $s = \rho/\rho_o$ is the condensation, and ρ is the density. In addition, the equation of state for a perfect gas can be logarithmically differentiated to yield

$$p = p_o[s + (\gamma - 1)\theta'], \quad (2.91)$$

where $\theta' = T/((\gamma - 1)T_o)$ is the reduced temperature, and p is the pressure. The subscript o is used to denote the equilibrium values. Zwikker and Kosten refer to the above equation as the ‘compression equation’. Finally, an appropriate form of the energy equation is required. A detailed derivation is provided here since it was not found in any of the references. In its most general form, the energy equation is

$$\rho \frac{D(e + \frac{\xi^2}{2})}{Dt} = -\nabla \cdot p \dot{\boldsymbol{\xi}} + \rho \mathbf{B} \cdot \dot{\boldsymbol{\xi}} + \nabla \cdot \tau \dot{\boldsymbol{\xi}} - \nabla \cdot \dot{\mathbf{q}} + \rho Q, \quad (2.92)$$

where e is the internal energy, \mathbf{B} is the body force term, τ is the stress tensor, $\dot{\mathbf{q}}$ is the heat flux per unit area to the surroundings and Q represents any internal heat addition. Linearizing the above equation, and neglecting viscous effects, internal heat addition and pressure gradients, one obtains

$$\rho_o \frac{De}{Dt} = -p_o \nabla \cdot \dot{\boldsymbol{\xi}} - \nabla \cdot \dot{\mathbf{q}}. \quad (2.93)$$

Using the continuity equation, and Fourier's law ($\dot{\mathbf{q}} = -k\nabla T$), where k is the thermal conductivity, the above becomes

$$\rho_o \left(\frac{De}{Dt} - p_o \frac{D\frac{1}{\rho}}{Dt} \right) = k\nabla^2 T. \quad (2.94)$$

Using the thermodynamic identity $Tds = de + pd\frac{1}{\rho}$, the above can be written as

$$\rho_o T_o \frac{Ds}{Dt} = k\nabla^2 T, \quad (2.95)$$

where s is the entropy. Noting that

$$ds = \left(\frac{\partial s}{\partial T} \right)_p dT + \left(\frac{\partial s}{\partial p} \right)_T dp \quad (2.96)$$

$$= \left(\frac{C_p}{T} \right) dT - \left(\frac{\partial v}{\partial T} \right)_p dp \quad (2.97)$$

$$= \left(\frac{C_p}{T} \right) dT - \left(\frac{1}{\rho T} \right) dp \quad (2.98)$$

where subscripts p and T refer to differentiation while holding them constant and C_p is the ratio of specific heat at constant pressure. The substitutions in the second line are made by recognizing the definition $C_p = T(\partial s/\partial T)_p$ and using Maxwell's thermodynamic relation $(\partial s/\partial p)_T = -(\partial v/\partial T)_p$. The substitution in the third line is made assuming an ideal gas. The energy equation becomes

$$\rho_o C_p \frac{DT}{Dt} = \frac{Dp}{Dt} + k\nabla^2 T. \quad (2.99)$$

Note that the assumed time dependance of the variables is of the form $e^{-j\omega t}$; therefore, the time derivatives can be replaced with $-j\omega$. Performing this step and rearranging, the above equation can be expressed as

$$\nabla^2 T + r_t^2 T = r_t^2 \frac{p}{\rho_o C_p}, \quad r_t^2 = \frac{j\omega \rho_o C_p}{k}. \quad (2.100)$$

Finally, expressing in terms of θ' , using the ideal gas relations, and expanding the Laplace operator, one obtains

$$\left[\frac{\partial^2}{\partial r^2} + \frac{1}{r} \frac{\partial}{\partial r} + r_t^2 \right] \theta' = r_t^2 \frac{p}{\gamma p_o}, \quad r_t^2 = \frac{j\omega \rho_o C_p}{k}, \quad (2.101)$$

where γ is the ratio of specific heats. Recall that p is assumed constant; therefore, the above equation is in exactly the same form as Equation 2.78 and the solution can be immediately written down as

$$\theta' = \frac{1}{\gamma} \frac{p}{p_o} \left[1 - \frac{J_0(r_w r)}{J_0(r_w r_t)} \right]. \quad (2.102)$$

Substituting into Equation 2.91, one obtains

$$s = \frac{1}{\gamma} \frac{p}{p_o} \left[1 + (\gamma - 1) \frac{J_0(r_w r)}{J_0(r_w r_t)} \right]. \quad (2.103)$$

Using the continuity equation, one then obtains

$$\frac{\partial \dot{\xi}}{\partial x} = j\omega \frac{p}{\rho_o c^2} \left[1 + (\gamma - 1) \frac{J_0(r_w r)}{J_0(r_w r_t)} \right], \quad (2.104)$$

where $\gamma p_o = \rho_o c^2$ from the ideal gas law. Using Equation 2.82, the average velocity can be expressed as

$$\frac{\partial \bar{\xi}}{\partial x} = j\omega \frac{p}{\rho_o c^2} \left[1 + (\gamma - 1) \frac{2}{r_w r_t} \frac{J_1(r_w r)}{J_0(r_w r_t)} \right]. \quad (2.105)$$

Finally, the desired specific acoustic admittance per unit length is

$$Y = \frac{\partial \bar{\xi} / \partial x}{p} = \frac{j\omega}{\rho_o c^2} \left[1 + (\gamma - 1) \frac{2}{k_t} \frac{J_1(k_t)}{J_0(k_t)} \right], \quad (2.106)$$

where $k_t = r_w r_t$ as defined in Equation 2.19. Similar to the definition of Z used earlier, $\partial \bar{\xi} / \partial x$ is used in the definition of Y instead of $\bar{\xi}$ since it is desirable to obtain the specific admittance *per unit length*. This is the same as Equation 2.18 with, once again, the difference of a sign due to the opposite assumed positive tube axis directions.

2.3.6 Propagation of an Acoustic Wave in an Infinite Cylindrical Tube

The electrical analogy given above was extremely useful in analyzing the problem of forced acoustic oscillations in a long, thin tube and provided some understanding of the viscous and thermal dissipation mechanisms. This knowledge is still somewhat incomplete, however, since the validity regime of the electrical analogy has not yet been identified except by the original assumption that the hole diameter be much smaller than the acoustic wavelength. For this reason, it is desirable to take this analysis one step further and to examine the details of the dissipation processes at the level of individual acoustic waves.

The propagation of a plane acoustic wave in an infinitely long, thin cylindrical tube has been studied extensively. The full problem which included viscous and thermal conduction effects was first completely solved by Kirchhoff [61]. This was significant since both viscous and thermal effects are generally of the same order of magnitude and neither can be neglected. The full derivation of this solution is provided in Appendix B and it is seen that the critical portion is the determination of the ‘propagation constant’ which governs the attenuation of the acoustic wave. Although the closed form of the complete solutions are unnecessarily complicated for most situations, Kirchhoff showed that a relatively simple solution can be obtained for the limiting case of a wide tube. This same work was later reviewed and repeated by Lord Rayleigh [121] who also extended the work to include a simple solution for the limiting case of a very narrow tube. More recently, Stinson [119] revisited the complete Kirchhoff solution and identified the validity regimes (in terms of frequency and tube radius) of the various approximate methods developed in the past, including the electrical analogy used by Fedorov and Malmuth.

To better understand the phenomenon, the complete Kirchhoff problem was solved for the two limiting cases which are depicted graphically in Figure 2.8. In the case of the narrow tube, the expected motion is lamellar with the velocity varying from zero at the wall to a maximum at the tube centre. This is very similar to Poiseuille flow and, in fact, Rayleigh showed that Kirchhoff’s solution could be reduced to Poiseuille flow in this limit. In this case, the viscosity and thermal conduction dominate the flow since the internal viscous and thermal boundary layers engulf the entire tube. Here, the word ‘internal’ is used to distinguish the boundary layer within a hole as opposed to the boundary layer over the external surface as shown earlier in Figure 2.3. It should be noted that, in this case, the

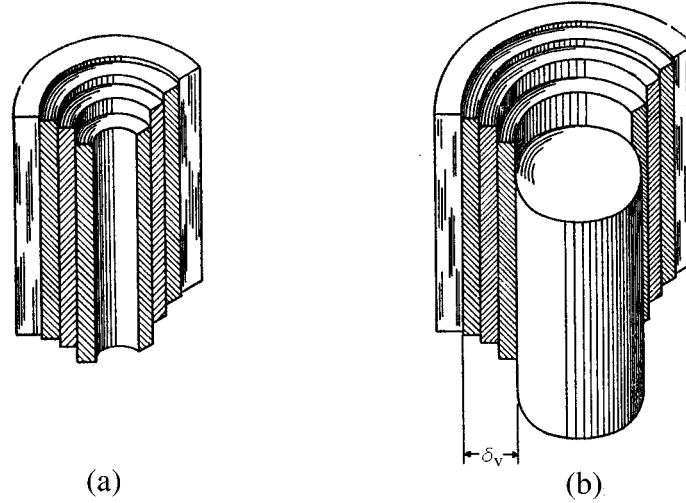


Figure 2.8: Schematic diagram showing the expected motion of the fluid in the two extreme cases of (a) the narrow tube and (b) the wide tube. The narrow tube limit is dominated by viscosity and behaves very much like Poiseuille flow with the velocity increasing smoothly to a maximum at the centre (*i.e.*, parabolic velocity profile). In the wide tube limit, the effects of viscosity are limited to the near-wall regions and the inertia of the large mass of fluid in the centre dominates (*i.e.*, top-hat velocity profile). (Reproduced from Crandall [20])

dissipation is occurring entirely due to viscous effects. The thermal conduction to the tube walls occurs so readily that, in essence, the tube walls control the temperature of the gas. It will be shown later that this effect is so strong that the expansions and compressions of the gas occur isothermally. Rayleigh observed that, under such conditions, the dissipation due to heat conduction is so negligible that it is as if no heat were generated at all. For the wide tube, the velocity gradient is limited to a thin region along the tube wall (*i.e.*, the viscous internal boundary layer) and there is a large central mass of fluid that oscillates as a slug, inducing a phase delay. The overall motion is, in fact, dominated by the inertia of the large central mass. In contrast to the case of the narrow tube, here the dissipation is limited to the thin internal boundary layer region and both viscous and thermal conduction are of similar magnitude.

In the previous paragraph, many allusions have been made to the concepts of a narrow tube and a wide tube, without actually defining these terms precisely. It should be obvious that the relevant length scales are the internal viscous and thermal boundary layer thicknesses. By dimensional analysis, these can be shown to be

$$\delta_v = \sqrt{\frac{\mu}{\omega \rho_o}}, \quad \delta_t = \sqrt{\frac{k}{\omega \rho_o C_p}}, \quad \delta_t = \frac{1}{\sqrt{Pr}} \delta_v, \quad (2.107)$$

where δ_v and δ_t are the internal viscous and thermal boundary layer thicknesses, ω is the angular frequency, μ is the dynamic viscosity, k is the thermal conductivity, C_p is the specific heat at constant pressure, and ρ_o is the equilibrium density. Benade [6] performed computations and showed that the conditions for the narrow and wide tube are

$$\text{Narrow Tube: } \frac{r_w}{\delta_v} \leq 0.5, \quad \text{Wide Tube: } \frac{r_w}{\delta_v} \geq 60, \quad (2.108)$$

where r_w is the tube radius. Alternatively, Weston [131] used a classification scheme based on the quantities

$$\ell_1 = 2r_w f^{1/2}, \quad \ell_2 = 10^{-8} r_w f^{3/2} \quad (2.109)$$

to discriminate between narrow tubes, wide tubes and very wide tubes. A narrow tube has $\ell_1 \ll 1 \text{ cm s}^{-1/2}$; the wide tube has $\ell_1 \gg 1 \text{ cm s}^{-1/2}$ and $\ell_2 \ll 1 \text{ cm s}^{-3/2}$; and the very wide tube has $\ell_2 \gg 1 \text{ cm s}^{-3/2}$. Note that \ll and \gg are used here to indicate that the quantities must be at least one order of magnitude smaller or larger, respectively. Also, Weston noted that this entire dimensional analysis is only valid for $r_w > 10^{-3} \text{ cm}$ for which the hole radius is larger than the mean-free path and for $f < 10^8 \text{ Hz}$ for which the wavelength is larger than the mean-free path.

The Kirchhoff solutions are presented in Figure 2.9 which plots the magnitude of the perturbation quantities (axial velocity u , radial velocity u_r , normalized pressure p/p_o , normalized density ρ/ρ_o , and normalized temperature T/T_o) along the radius of the tube for the limiting cases of the narrow and wide tubes. As a quick check, the first observation is that the velocity and temperature boundary conditions at the wall are satisfied. Furthermore, as expected, in both cases the pressure is essentially constant across the cross-section. This arises from the fundamental assumption that the acoustic wavelength is much larger than the diameter. In the case of the narrow tube, all other quantities can be seen to vary with radius. In particular, the plot of axial velocity shows characteristic Poiseuille-like behaviour. As described earlier, this is to be expected since the internal boundary layer engulfs the entire tube. In contrast, in the wide tube the quantities are seen to be essentially constant throughout most of the tube, with all gradients limited to the region very close to the wall. Finally, recognizing that $\gamma = (p/p_o)/(\rho/\rho_o)$, it is interesting to observe (as noted

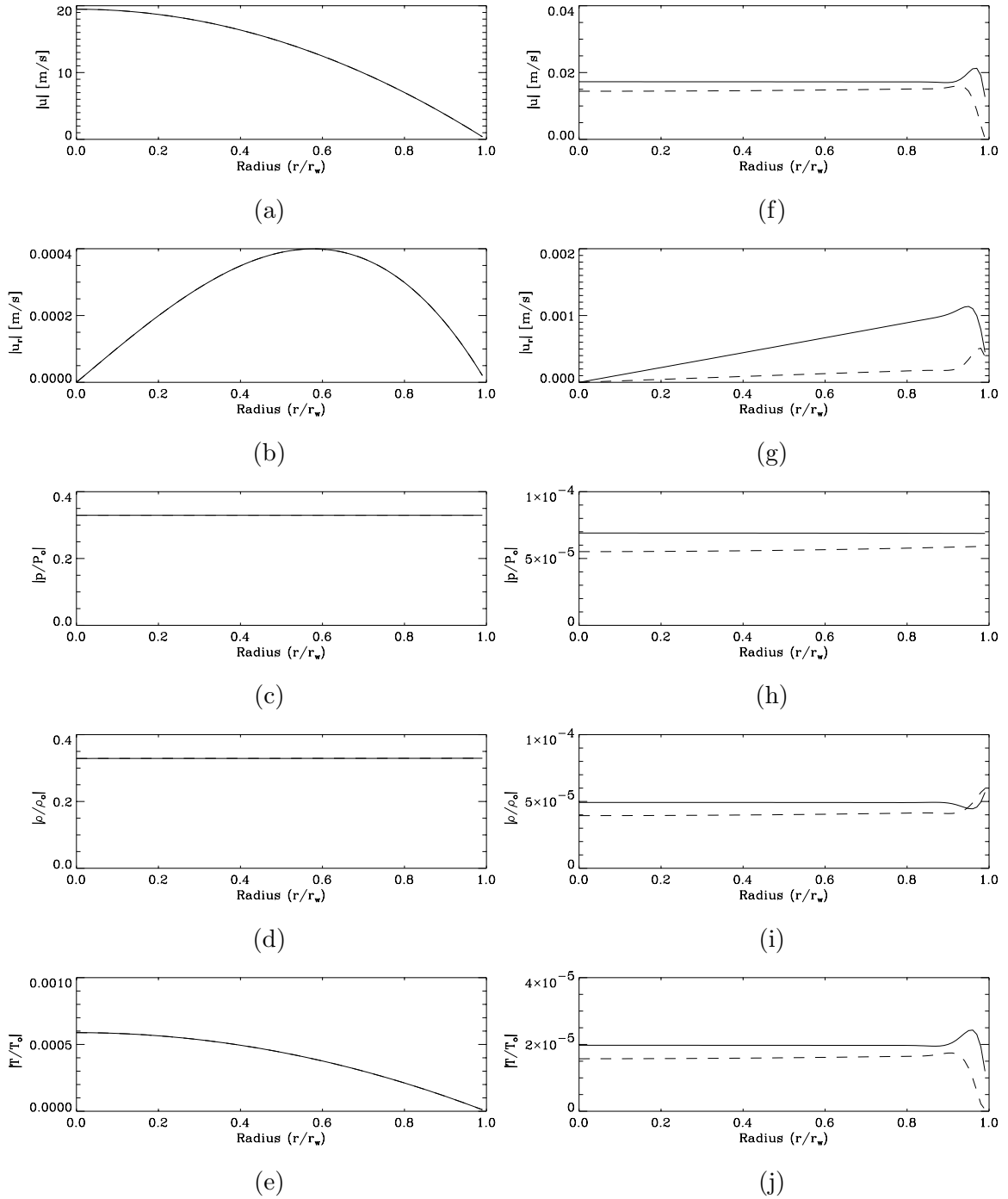


Figure 2.9: Radial variation of the magnitude of the perturbation quantities (axial velocity u , radial velocity u_r , normalized pressure p/p_o , normalized density ρ/ρ_o , and normalized temperature T/T_o) for (a)-(e) the narrow tube limit ($f = 10$ Hz, $r_w/\delta_v = 0.2$) and (f)-(g) the wide tube limit ($f = 1$ MHz, $r_w/\delta_v = 63$), respectively. In both cases $r_w = 100 \mu\text{m}$, $p_o = 100$ kPa, $T_o = 295$ K, $\rho_o = 1.1$ kg/m³, and $\nu = 1.5 \times 10^{-5}$ Ns/m². The solid line is evaluated at axial location $x = 9r_w$ and the dashed line is at $x = 10r_w$.

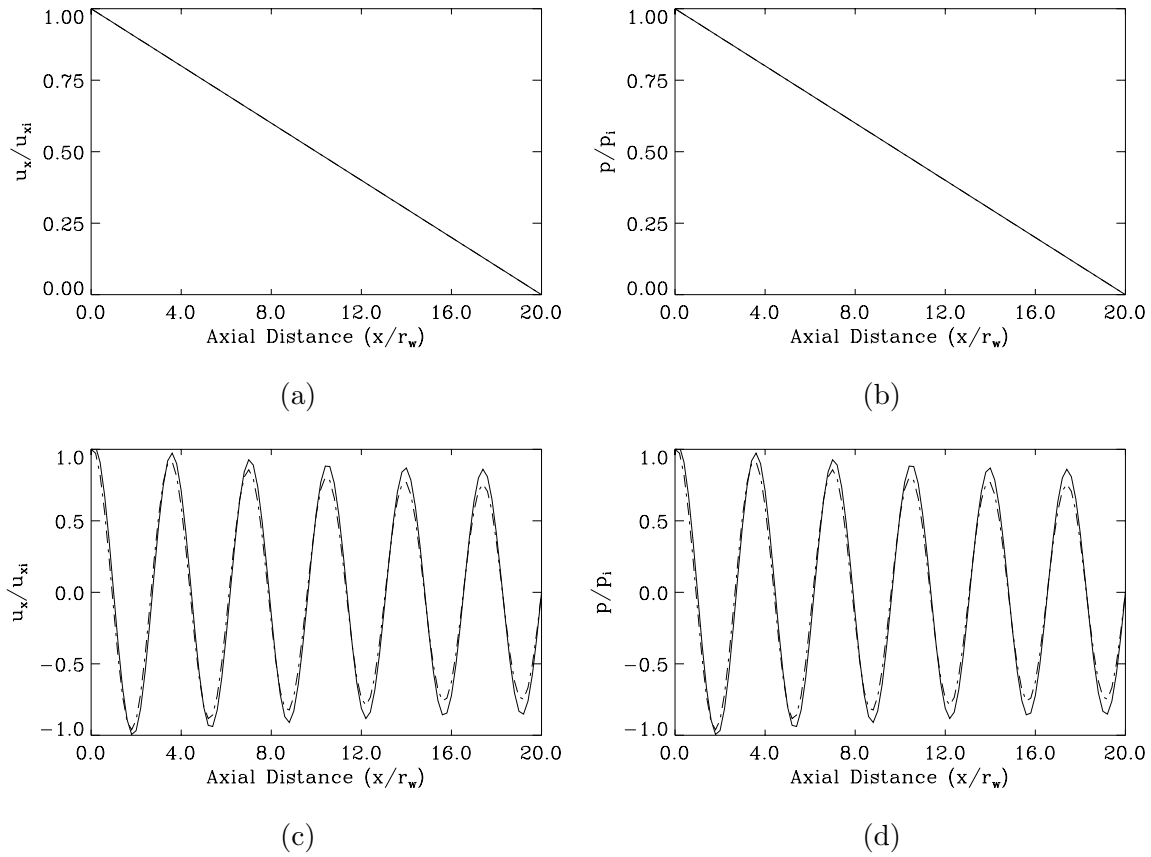


Figure 2.10: Axial variation of the particle velocity and pressure perturbation (normalized with respect to the value at the input) for the (a)-(b) narrow tube and (c)-(d) wide tube calculated using Equations 2.39 and 2.40. The solid line uses the propagation constant evaluated by the Kirchhoff solution while the dashed-dotted line uses the value obtained using the electrical analogy. All parameters are the same as used for the calculations plotted in Figure 2.9. The length of the tube is taken to be 10 diameters, and the boundary impedances were $Z_p = 0$ and $Z_L \rightarrow \infty$.

by Stinson [119]) that this ratio is approximately 1.0 for the narrow tube indicating that the sound propagation is isothermal. Similarly, for the wide tube, this ratio is 1.4 and is indicative of adiabatic sound propagation. The solid line and dashed lines correspond to two different locations along the length of the tube. The attenuation of the perturbations is clearly seen. Figure 2.10 shows the axial variation of the normalized particle velocity and pressure perturbations within the tube for the limiting cases considered above. As one might intuitively expect, the narrow tube strongly damps acoustic perturbations due to the strong viscous effects acting over the entire cross-section. Conversely, the wide tube attenuates the wave very weakly since the dissipation is limited to the very thin boundary layer region near the tube wall. In both cases, the electrical analogy is seen to compare very well with the Kirchhoff solution (the difference, in fact, in the narrow tube is not visible).

2.3.7 Limitations of the Electrical Analogy

It is now possible to re-examine the value and limitations of the electrical analogy in view of the exact Kirchhoff solution for propagation of a single acoustic wave. This solution depends primarily on the propagation constant which must be obtained numerically (see Appendix B). One immediately recognizes that the electrical analogy can be used to estimate this quantity. By comparing with the exact Kirchhoff solution, one can then determine the accuracy and validity regime of the electrical analogy.

Such calculations and comparisons have been performed in the past. The motivation at the time was somewhat different in that the main goal was to approximate the Kirchhoff solution with a simpler form. The expressions derived previously for the specific impedance and admittance per unit length are discussed extensively in Benade [6], Daniels [23], and Mawardi [73]. Benade examined the high and low frequency limits of the expressions and numerically showed that his simpler expressions compared well with the original ‘exact’ expressions previously derived. Daniels, in addition to deriving the expression for the shunt admittance in the earlier paper, also performed a numerical comparison of the characteristic impedance and propagation constant computed using the electrical analogy with the exact solution from Kirchhoff. Finally, Mawardi attempted to extend the above work to porous surfaces with different microstructure (*i.e.*, not necessarily parallel cylindrical microholes). In addition, Tijdeman [128] performed detailed numerical comparisons of the electrical analogy and other approximate methods with the exact Kirchhoff solution.

Despite the apparent success of the electrical analogy, there are some unresolved issues that need to be clarified. First, the regime of validity of the above expressions has not yet been satisfactorily addressed. So far, the equations were derived based on the vague requirement that the diameter of the tube be much smaller than the acoustic wavelength. This is, in fact, a fundamental assumption of the Kirchhoff analysis and does not give any useful information as to the validity regime of the electrical analogy. Also, during the derivation, the series impedance was derived assuming that thermal effects were negligible while the shunt admittance was derived assuming that the viscous effects were negligible. Although this uncoupling might be a reasonable assumption, it is not clear from an *a priori* examination of the underlying Kirchhoff differential equations.

Stinson [119] performed an in-depth term-by-term analysis of the exact Kirchhoff so-

lution and showed that it could be reduced to the expressions derived using the electrical analogy. The assumptions used by Stinson during his reduction of the exact Kirchhoff relation were based on Weston's classification scheme described in Section 2.3.6. Stinson rigorously showed that the expressions derived in the electrical analogy were valid for the case of the narrow tube, the wide tube and all intermediate cases, but not the very wide tube, provided that

$$r_w f^{3/2} < 10^6 \text{ cm s}^{-3/2}, \quad r_w > 10^{-3} \text{ cm.} \quad (2.110)$$

The first requirement comes from assuming that an acceptable ℓ_2 is $0.01 \text{ cm s}^{-3/2}$ in Equation 2.109 and the second comes from the requirement that the hole size be larger than the mean-free path. In the same analysis, Stinson furthermore demonstrated that the viscous effects and thermal effects were uncoupled. An assessment of Stinson's analysis indicates that his first requirement is conservative and can probably be relaxed to $r_w f^{3/2} < 10^7 \text{ cm s}^{-3/2}$.

2.3.8 Alternate Approach to the Electrical Analogy

A slightly different approach to the electrical analogy is described in Zwicker and Kosten [137], more recently by Attenborough [5], and most recently by Stinson [119, 120]. Rather than using an electrical analogy, they propose the use of a 'complex density' $\rho^\diamond(\omega)$ and a 'complex compressibility' $C^\diamond(\omega)$. The complex density is derived based on the linearized momentum equation for the propagation of a plane acoustic wave neglecting viscous effects which is

$$\rho^\diamond(\omega) \frac{\partial \bar{\xi}}{\partial t} = -\frac{\partial p}{\partial x}, \quad (2.111)$$

where $\bar{\xi}$ is the average perturbation velocity, p is the perturbation pressure, ω is angular frequency, and x is the direction of propagation. Assuming the usual time dependance of the form $e^{-j\omega t}$, the complex density is expressed as

$$\rho^\diamond(\omega) = \frac{\partial p / \partial x}{j\omega \bar{\xi}}. \quad (2.112)$$

The interpretation of the complex density is that it represents the effective increased density of the medium due to inertial and viscous effects. Comparing the above with Equation 2.84, it is clear that the series specific impedance is related to the complex density through the

relation

$$Z = j\omega\rho^\diamond(\omega). \quad (2.113)$$

Similarly, a complex compressibility is defined as

$$C^\diamond(\omega) = \rho_o \frac{p}{\bar{\rho}}, \quad (2.114)$$

where $\bar{\rho}$ is the average density perturbation, and the subscript o is used to denote the equilibrium value. Note that Stinson uses the reciprocal of this expression in his definition. Once again, a simple relation exists between the shunt specific admittance and the complex compressibility. Recognizing that the continuity equation is

$$-\frac{1}{\rho_o} \frac{\partial \bar{\rho}}{\partial t} = \frac{\partial \bar{\xi}}{\partial x}, \quad (2.115)$$

one obtains

$$C^\diamond(\omega) = j\omega \frac{p}{\partial \bar{\xi} / \partial x}, \quad (2.116)$$

where the time dependence of the form $e^{-j\omega t}$ has already been taken into account. Comparing with Equation 2.106, it is clear that

$$Y = \frac{j\omega}{C^\diamond(\omega)}. \quad (2.117)$$

The expressions for the characteristic impedance and the propagation constant become

$$Z_o = \sqrt{\rho^\diamond C^\diamond} \quad \Lambda = j\omega \sqrt{\frac{\rho^\diamond}{C^\diamond}}. \quad (2.118)$$

Although it seems that the above concepts are redundant, they are not. In fact, the idea of the complex density and complex compressibility are more general expressions that can be used to extend the Kirchhoff theory. Although Zwikker and Kosten, and Attenborough simply used the electrical analogy relations for Z and Y to obtain the required complex density and complex compressibility, Stinson took a more fundamental approach. His analysis derived the ρ^\diamond and C^\diamond starting from the fundamental Kirchhoff solution using the assumptions described in the previous section. His approach confirmed the validity of these ideas and also allowed a rational extension to tubes of arbitrary cross-section [120]

through the use of correction factors. Furthermore, the use of the complex density and complex compressibility could potentially allow the consideration of even more general porous microstructures.

2.4 Theoretical Basis for the Present Experiments

Having reviewed the theory of Fedorov and Malmuth, as well as the fundamental flow physics, it is now possible to use the theory to develop preliminary requirements for the experimental setup. In particular, it is clear that the sizing of the holes is critical for the acoustic damping to be effective. Recall from the previous chapter that the wavelength of the most unstable (Mack mode) was approximately 1 mm to 2 mm for the experimental conditions under consideration. The fundamental Kirchhoff analysis is based on the assumption that the tube size is much smaller than the acoustic wavelength, and therefore, as a bare minimum $r_w \ll 1$ mm. The previous chapter also indicated that the frequencies of the most unstable mode (Mack mode) for the experiments to be performed are of the order of 1 MHz. This being the case, Stinson's criteria is much more stringent and suggests that the hole size must be of the order of 10 μm in order for the electrical analogy, and hence the work of Fedorov and Malmuth, to be applicable. Finally, there was the practical consideration that the holes needed to be small enough (relative to the boundary layer thickness) such that they did not prematurely trip the boundary layer.

The desired parameters for the porous surface were initially determined based on the estimated wavelength of the most unstable mode (*i.e.*, twice the boundary layer thickness). Assuming 10 to 20 holes per wavelength and that they are arranged in a rectangular grid pattern (as in Figure 2.3) with a minimum distance of one hole diameter between the edges of adjacent holes (for structural integrity) results in a required hole diameter of 50 μm spaced 100 μm apart (centre-to-centre). These parameters yield an open area or porosity (n) of 20%. The required thickness of the sheet (thus the depth of the holes) was determined based on the analysis performed by Fedorov and Malmuth [32]. Figure 2.5b was a plot of the growth rate as a function of hole depth which showed that the non-dimensional hole depth (with respect to displacement thickness) should be $h^* \geq 0.3$. In dimensional terms, this requires that the hole be at least 0.1 mm deep (preferably deeper) since the displacement thickness of a laminar boundary is approximately 1/3 of the boundary layer

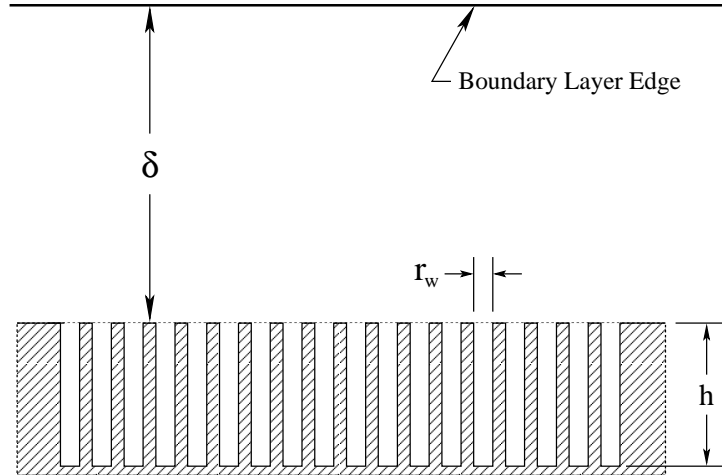


Figure 2.11: Schematic drawing showing the porous surface to scale. The holes have a diameter of $60 \mu\text{m}$ ($r_w = 30 \mu\text{m}$), a depth of $h = 450 \mu\text{m}$, and are spaced $100 \mu\text{m}$ apart arranged in a rectangular grid. The boundary layer has a thickness of about $\delta = 1 \text{ mm}$.

thickness. Also, based on calculations by Fedorov and Malmuth, it was determined that the porous surface should begin at approximately 150 mm from the leading edge or cone tip. This corresponds to the lower branch of the neutral curve of the second mode at a frequency of approximately 1 MHz . One important point not explicitly mentioned in the analysis is that it is imperative that each individual hole be unconnected from its neighbours so that there is no possible communication between holes (*i.e.*, no net suction or blowing through the holes).

As will be described in Section 3.3, the final parameters actually achieved for the present experiments were holes that were $60 \mu\text{m}$ in diameter, spaced $100 \mu\text{m}$ apart yielding a porosity of $n = 28\%$ (see Figure 2.11). As a first observation, this hole size is just within Stinson's criteria for validity of the electrical analogy model. The second observation is that the ratio $r_w/\delta_v \simeq 6$ indicating that, although the electrical analogy can be used, this does not represent either of the limiting cases of the narrow or wide tube examined earlier. Figure 2.12 shows the radial variation of the perturbation quantities evaluated at the expected experimental conditions. The solid line corresponds to the full Kirchhoff solution using the propagation constant evaluated using Kirchhoff's method. The dashed-dotted line corresponds to the Kirchhoff solution, except using the propagation constant evaluated using the electrical analogy. Note that for this case the dynamic viscosity $\mu = 2.0 \times 10^{-5} \text{ Ns/m}^2$ and the density $\rho_o \simeq 0.1 \text{ kg/m}^3$, which are representative of the conditions at the surface of the test model during an experiment. As anticipated from the ratio r_w/δ_v , the internal

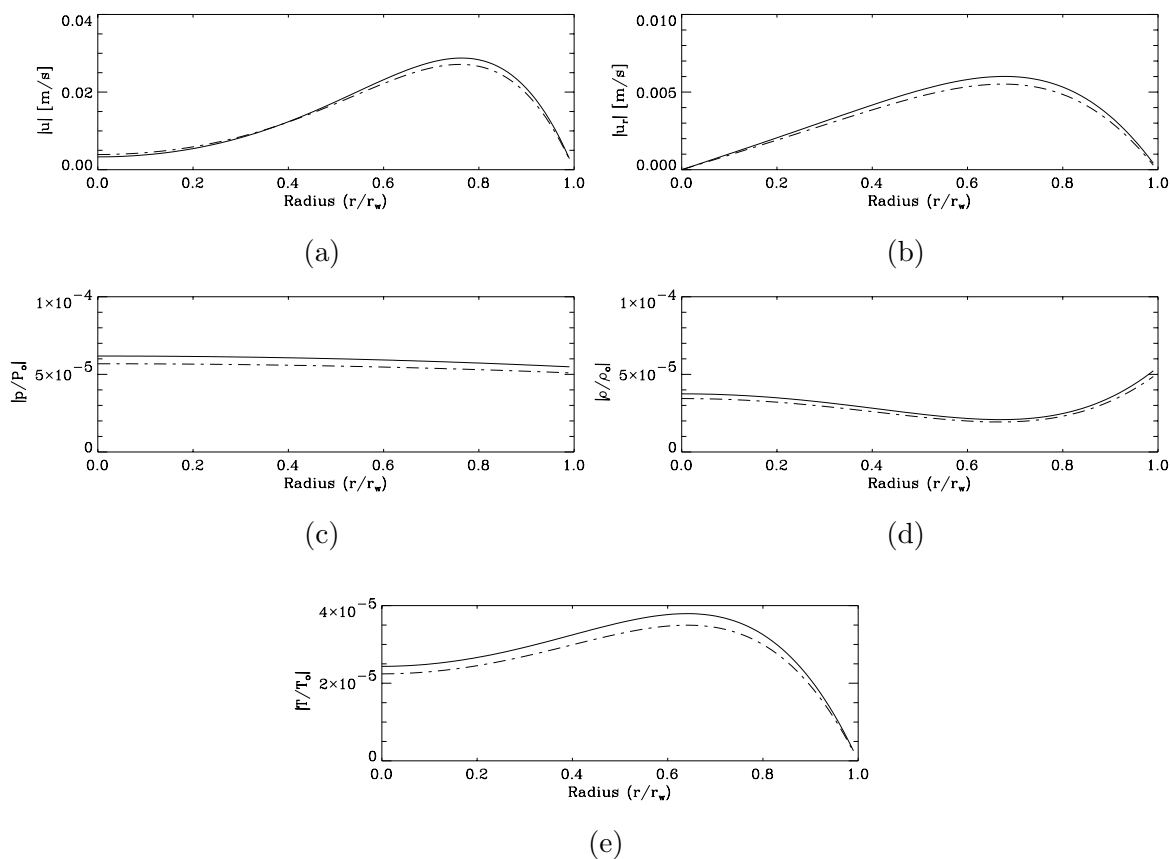


Figure 2.12: Radial variation of the magnitude of the perturbation quantities (axial velocity u , radial velocity u_r , normalized pressure p/p_o , normalized density ρ/ρ_o , and normalized temperature T/T_o) for typical expected experimental conditions; $r_w = 30 \mu\text{m}$, $f = 1 \text{ MHz}$, $p_o = 10 \text{ kPa}$, $T_o = 295 \text{ K}$, $\rho_o = 0.1 \text{ kg/m}^3$, and $\nu = 2.0 \times 10^{-4} \text{ Ns/m}^2$, $x = 10 r_w$. The solid line corresponds to the Kirchhoff solution ($\Lambda = (0.42 + j2.11) \times 10^4 \text{ m}^{-1}$) and the dashed-dotted lines corresponds to the Kirchhoff solution using the propagation constant evaluated by the electrical analogy ($\Lambda = (0.40 + j2.12) \times 10^4 \text{ m}^{-1}$).

boundary layer occupies a significant fraction of the tube, and this can be seen in the plots of the axial velocity perturbation and the temperature perturbation. It appears that only the inner 20% of the flow is approximately uniform, so both viscous and thermal effects are likely to play a role in the dissipation processes. As before, the pressure is essentially constant across the tube. Figure 2.13 shows the axial variation of the normalized particle velocity and pressure perturbation within a hole at the expected experimental conditions. As expected, there is significant damping of the acoustic waves in the tube and, once again, the electrical analogy is seen to compare favourably with the exact Kirchhoff solution.

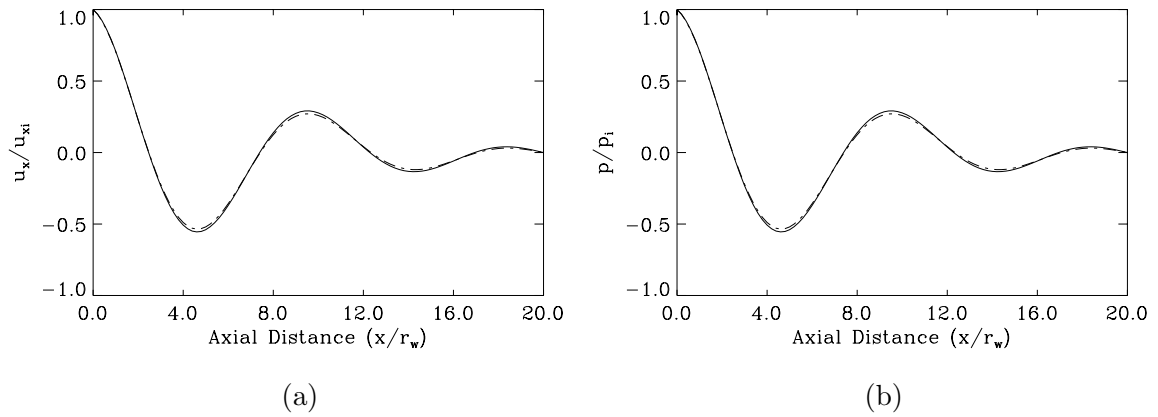


Figure 2.13: Axial variation of normalized particle velocity and pressure perturbation within a hole at the expected experimental condition. The solid line uses the propagation constant evaluated by the Kirchhoff solution while the dashed-dotted line uses the value obtained using the electrical analogy. All parameters are the same as used for the calculations plotted in Figure 2.12. The length of the tube is taken to be 10 diameters (as in the experiments), and the boundary impedances were $Z_p = 0$ and $Z_L \rightarrow \infty$.

Chapter 3 Experimental Approach

This chapter describes the overall objectives and experimental approach used to test the effectiveness of an acoustically absorptive surface in delaying transition. It then describes the facility used for these experiments, provides details of the model and instrumentation and discusses the issue of the soot generated in the tunnel. Finally, it details the theoretical models used to estimate the expected heat flux and explains the analysis required to obtain the measured heat flux from the experiments.

3.1 Experimental Objective and Method

The previous set of experiments and linear stability analyses provided the basis for the current experimental study. In particular, the large database of results from the experiments by Germain [38] and Adam [2] provided important comparison data to serve as a checkpoint for the new results. Furthermore, the linear stability calculations by Johnson *et al.* [51] indicated that the Mack mode was indeed the dominant instability mode. Finally, Fedorov and Malmuth's linear instability calculations [32] proposed a mechanism to delay the boundary layer transition which directly addressed this mode.

The broad objective was to test the effectiveness of the proposed passive hypervelocity boundary layer control scheme. This was to be accomplished by testing a nominal 5° half-angle cone with a smooth surface on one side and the ultrasonically absorbing porous surface on the other side at zero angle-of-attack in the T5 Hypervelocity Shock Tunnel. As was done in the previous experiments, the transition location was determined by the use of flush-mounted heat transfer gauges. Simultaneous comparison of the results on both surfaces allowed each experiment to be self-contained with transition Reynolds number on the smooth surface providing a direct baseline for the porous surface results.

3.2 T5 Hypervelocity Shock Tunnel

3.2.1 Description

The main purpose of this facility is to correctly simulate hypervelocity flows by matching the enthalpy similarity criteria. It is relevant to note that, when performing ground tests of scale models of flight vehicles, it is possible to match the high Mach number either by decreasing the speed of sound of the gas (by lowering the temperature) or by increasing the flow velocity. For real flight vehicles, high Mach numbers are achieved by high flight velocities. In wind tunnel testing, however, it is much easier to decrease the temperature of the test gas. This results in ‘cold’ hypersonic flows which duplicate some of the relevant physical flow phenomena, but not the proper chemical phenomena, such as molecular dissociation and recombination. It is apparent that the effects of chemistry can only be observed in test flows that match the high flight velocities and consequently the high temperatures. These flows are called ‘hot’ hypersonic flows or hypervelocity flows and can be produced in high enthalpy facilities such as the T5 Hypervelocity Shock Tunnel. Hornung [47] discusses in detail the relevant similarity criteria for hypervelocity flows and the importance of high enthalpy facilities.

This reflected shock tunnel facility consists of the six major components shown in Figure 3.1: the piston, the secondary reservoir (2R), the compression tube (CT), the shock tube (ST), the nozzle and the dump tank (DT). Prior to the shot, the various parts of the facility are filled with the appropriate gases depending on the run condition. The dump tank and nozzle sections are typically evacuated, while the secondary reservoir is filled with high pressure air ($P_{2R} \simeq 2$ MPa to 10 MPa), the compression tube is filled with a helium-argon mixture ($P_{CT} \simeq 100$ kPa), and the shock tube is filled with the desired test gas ($P_{ST} \simeq 100$ kPa or less). It is critical to tune the various pressures to carefully control the piston motion to avoid damage to the facility.

Initially a piston is loaded at the 2R-CT junction, isolating the two from each other. An experiment begins when the piston is moved slightly forward by an injection of air pressure from behind. This initial motion uncovers slots that join the secondary reservoir and the compression tube. The high pressure from the secondary reservoir then rapidly propels the piston forward in the compression tube resulting in the adiabatic compression of the helium-argon mixture. The rising pressure bursts the primary diaphragm causing a shock wave to

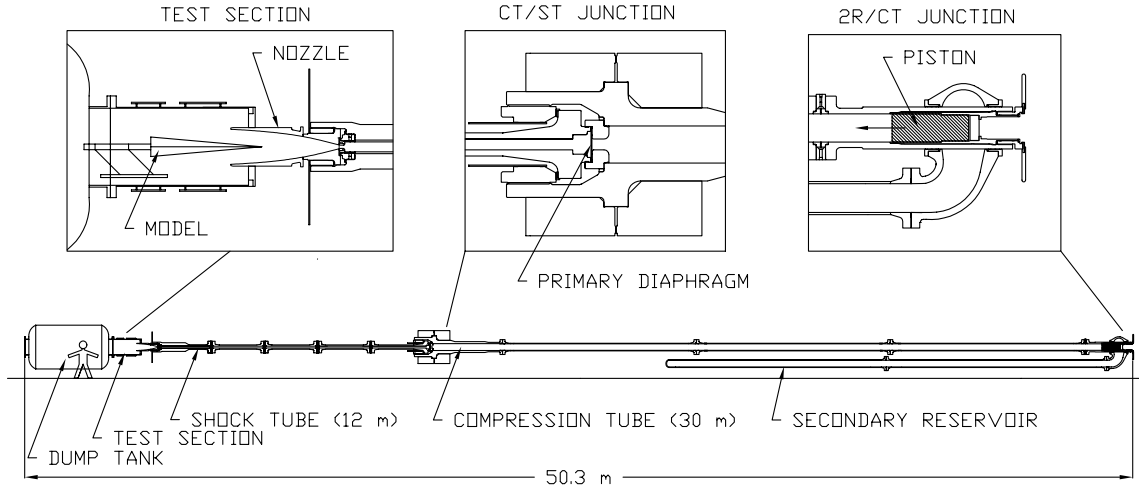


Figure 3.1: Schematic diagram of the T5 Hypervelocity Shock Tunnel. The six major components are the piston, the secondary reservoir, the compression tube, the shock tube, the test section and the dump tank. The outline of a person in front of the dump tank gives a sense of the overall size of the facility.

travel into a shock tube whose end wall is closed except for the small throat (30 mm) of the nozzle. The reflected shock from the end wall creates a quasi-constant pressure reservoir for the subsequent steady expansion through the nozzle (area ratio = 110) and into the test section. The primary diaphragm burst pressure can be varied from $P_4 \simeq 10$ MPa to 110 MPa and is controlled by using pre-scored diaphragms of different thicknesses. With air as the test gas, shock speeds of up to 5 km/s can be obtained to produce nominal Mach 5 flows with a specific reservoir enthalpy ranging from 3 MJ/kg to 25 MJ/kg, reservoir pressures from 5 MPa to 60 MPa and reservoir temperatures from 1000 K to 8000 K. Typical flow velocities are of the order of 4 to 5 km/s. Although the reservoir maintains a constant pressure for several milliseconds, the actual useful test time is limited to 1 to 2 ms due to driver gas contamination as indicated by studies by Sudani *et al.* [123, 124]. Other detailed descriptions regarding T5 operations and performance can be found in Hornung and Bélanger [48], Hornung *et al.* [49], and Hornung [46].

3.2.2 Data Acquisition System and Tunnel Diagnostic Data

The high speed data acquisition system consisted of three CAMAC-standard crates from DSP Technology capable of sampling 60 channels at 12-bit resolution. The first crate housed a GPIB crate controller module (CC-488), the trigger generator (Model 1024), an in-house manufactured laser controller and eight digitizer channels that were on four independently

controlled digitizer modules (Model 2612). These were used exclusively for tunnel diagnostic instrumentation. The other two crates housed the remaining 52 channels on 26 digitizer modules (Model 2860), 52 amplifiers (Model 1402E), the GPIB crate controllers (CC-488), the system controllers (Model 4012A/4032A) and memory modules (5200/5204). Each of these crates had a total throughput of 8 MSamples/second that was available entirely for model instrumentation. The data acquisition system was controlled using software developed in-house and run on a Sun workstation.

The tunnel diagnostic instrumentation consisted primarily of PCB piezoelectric pressure transducers located along the length of the facility. Two redundant transducers ($P_{o, \text{North}}$ and $P_{o, \text{South}}$) were located diametrically opposite each other on the shock tube at a distance of 48 mm from the shock tube end wall to measure the stagnation pressure in the reflected shock region. These transducers generated the trigger signal and thus $t = 0$ corresponds to the pressure rise in the stagnation region. Two more transducers (ST_3 and ST_4) were located at 2.37 m and 4.77 m from the shock tube end wall and were used to calculate the shock speed (u_s). Another two redundant transducers ($P_{4, \text{North}}$ and $P_{4, \text{South}}$) were located in the compression tube just upstream of the primary diaphragm in order to measure the diaphragm burst pressure. Additional diagnostic instrumentation consisted of two linear voltage displacement transducers (LVDT) to measure the tunnel recoil. Although its signal was not recorded, an accelerometer placed near the launch end of the facility was used to generate an early trigger signal (approximately 200 ms before the stagnation pressure rise) necessary for the laser used for flow visualization.

3.2.3 Calculation of Freestream Conditions in T5

The flow conditions in the freestream were computed based on the nozzle reservoir conditions (P_o , T_o) using a one-dimensional, inviscid, vibrational equilibrium, chemical non-equilibrium nozzle code (NENZF) written by Lordi *et al.* [66]. The output consisted of all relevant flow parameters including pressure (P_∞), temperature (T_∞), density (ρ_∞), velocity (u_∞), Mach number (M_∞), and chemical species concentrations. Although not used, a two-dimensional code (SURF) written by Rein [94] was also available to obtain flow profiles at the nozzle exit. This code was, in fact, used during T5 nozzle calibration studies by Rousset [98].

The nozzle reservoir pressure (P_o) was measured directly as the average of the two re-

dundant transducers ($P_{o, \text{North}}$ and $P_{o, \text{South}}$) and was used as one of the inputs for the NENZF code. The other reservoir conditions, such as temperature (T_o) and enthalpy (h_o), were computed based on the initial shock tube conditions (P_{ST}, T_{ST}) and the measured incident shock speed (u_s). This calculation was a one-dimensional equilibrium gasdynamics reflected-shock problem and was performed using the StanJan code written by Reynolds [97]. The thermodynamic properties used in StanJan were based on JANAF curve fits for each relevant species. Another program, the Equilibrium Shock Tube Calculation (ESTC) code by McIntosh [74], was also available and used a simple harmonic oscillator model to compute the relevant thermodynamic quantities. The calculated reflected-shock pressure was typically different from the measured pressure due to slightly off-tailored operation and two-dimensional effects. The mismatch between the two was resolved by assuming an isentropic expansion (or compression, as necessary) to the actual measured stagnation pressure. The enthalpy is referenced to 0 K with reference values of 0.0 MJ/kg for nitrogen and -8.93 MJ/kg for carbon dioxide.

3.2.4 Flow Visualization

The T5 test section was setup with 203 mm optical windows for flow visualization. In the past, flow visualization techniques included the use of schlieren, shadowgraphy, interferometry, and holographic interferometry. For the present series of experiments, increased sensitivity was required resulting in the use of resonantly enhanced shadowgraphy, which was initially used in T5 by Germain [37, 38] and subsequently further developed by Lemieux [65]. Further details about this technique can also be found in Bershader *et al.* [7]. In summary, this technique relies on the fact that the refractivity of a gas at its spectral line is several orders of magnitude greater than its general value at other wavelengths. This ‘enhanced refractivity’ can be used to greatly increase the sensitivity of any optical technique that relies on the index of refraction (*i.e.*, shadowgraphy, schlieren, and interferometry) by using a light source that is specifically tuned to be slightly off from the peak absorption wavelength. For work in T5, the flow was seeded with sodium, which has absorption lines in the visible spectrum (the sodium D-lines). The light source was a tunable dye laser (587-594 nm) built by Cummings [21], pumped by a 300 mJ/pulse frequency doubled Nd:YAG laser (532 nm) with a pulse width of 7 ns.

In practice, the issue of seeding the flow with sodium in a repeatable manner was quite

difficult. In Germain's experiments, it was possible to deposit small amounts of saline solution near the expected transition point and allow the water to evaporate, leaving a thin film of salt crystals. The sodium ions resulting from the dissociation of these crystals (due to the hot flow) were sufficient to produce the required image and the crystals (approximately 100 μm in height as measured by Germain [37]) were shown not to effect the transition location. For the present experiments, this technique was not possible because it would contaminate the porous surface. For this reason, it was necessary to limit the location of the salt deposition to the tip of the cone. It was found that Germain's technique was not as effective in such a situation since the sodium tended to disperse by the time it reached the typical transition point (roughly half-way along the length of the model). The resulting image was a standard shadowgraph which was not sensitive enough to highlight the boundary layer. This was rectified by ensuring a significant amount of salt crystals was present on the tip. This was done by dipping 10 mm of the cone tip into a super-saturated saline solution and then drying it with a heat gun. The result was that the first 10 mm of the cone tip was coated in fine sodium crystals in a random distributed roughness pattern. In addition, actual raw sodium was smeared circumferentially on the cone tip holder (approximately at the 100 mm location) immediately prior to closing the tunnel for the upcoming shot. This needed to be done quickly and with care since sodium reacts violently with moisture in the surrounding air. Once again, experiments were performed to verify that the increased salt and sodium deposition did not affect the transition location results.

3.3 Model and Instrumentation

3.3.1 Model Configuration

The model used for these experiments was a heavily modified version of the same model used by Germain [38] and Adam [2]. Its design and manufacture are of particular interest due to the unique challenges involved. Refer to Appendix C for the complete details.

The final configuration was a sharp 5.06° half-angle round cone consisting of five pieces with an overall length of 999 mm. It had a smooth surface over half the cone and the absorptive porous surface over the other half beginning at 148 mm from the cone tip (see Figure 3.2). The aluminum 6061 (Al 6061) 'base cone' used by Germain [38] and Adam [2]

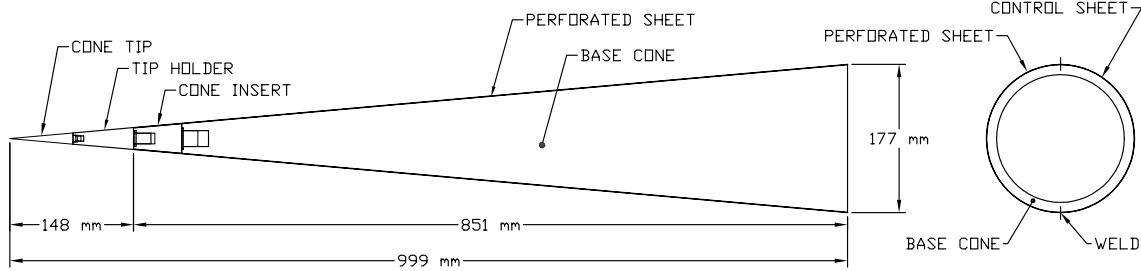


Figure 3.2: Schematic diagram of the assembled test model from the profile and rear view. The ‘cone sheet’ consisting of the perforated and solid sheets welded along the seams was attached to the base cone by means of a thermal interference fit.

was originally constructed in two halves with a ‘dove tail’ design that allowed them to be joined together without the use of mechanical fasteners that would disturb the boundary layer. It was lengthened by the ‘cone insert’ for the purposes of this project. The base cone was already hollow to allow room for instrumentation and this aspect was preserved. An intermediate piece made of stainless steel 304L (SS 304L) referred to as the ‘cone tip holder’ was screwed into this assembly. The molybdenum cone tip screwed into this intermediate piece and was replaceable in the event of excessive blunting or other damage. Extreme care was taken during the manufacturing process to minimize the steps at these junctions.

The ‘cone sheet’ was manufactured by rolling two initially flat sheets of metal (one perforated, one smooth) to form two longitudinal halves of a cone and then laser fusion welding them along the seams. Refer to Figure 3.3a for a micrograph of the weld. The resulting stainless steel cone sheet was then fitted over the aluminum base cone using a thermal interference fit that took advantage of the mismatch in thermal coefficients of expansion of the two materials. This assembly technique resulted in the cone sheet being stretched tightly over the base cone which provided the bottom for the blind microholes for the porous surface. The final porous surface had $60 \pm 4 \mu\text{m}$ diameter holes spaced $100 \pm 7 \mu\text{m}$ apart in a rectangular grid arrangement resulting in a porosity of 28%. The thickness of the sheet (thus the depth of the holes) was $450 \mu\text{m}$ (26 gauge sheet). Refer to Figure 3.3b for a micrograph of the porous surface. Due to the nature of the laser drilling process, the holes were slightly conical (taper angle of about 0.5°) with the small diameter exposed to the flow. Static acoustic absorption tests of this surface and other candidate materials that were considered during the design process are described in Appendix D. It should be noted that all surfaces that were exposed to the flow were made of SS 304L, with the exception of the removable tip which was made of molybdenum.

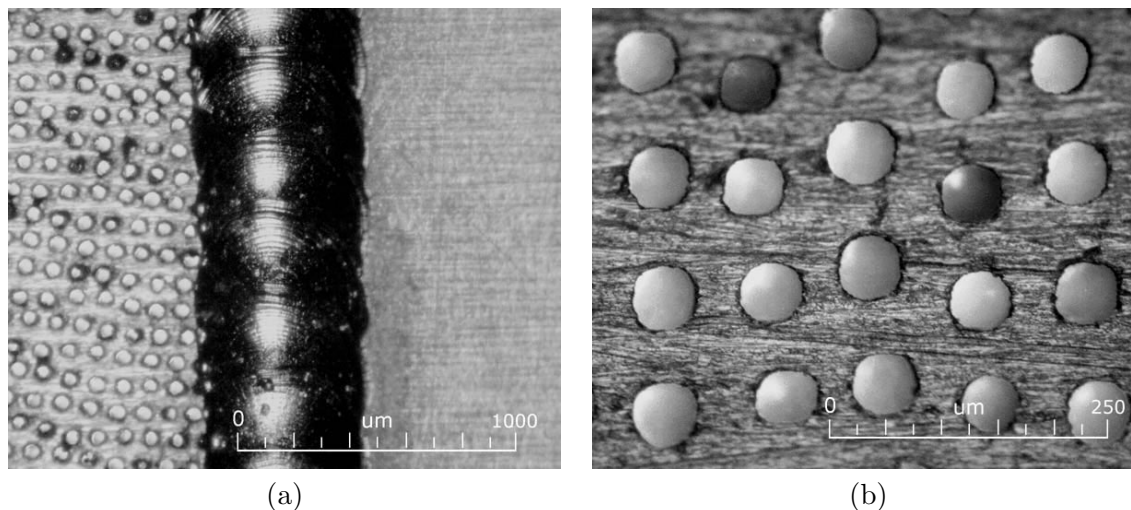


Figure 3.3: (a) Micrograph of the weld joining the perforated and solid sheet. The quality of the weld can be fully appreciated if one notes the scale on the micrograph. (b) Micrograph of the perforated sheet. The holes were measured to be $60 \pm 4 \mu\text{m}$ in diameter and spaced $100 \pm 7 \mu\text{m}$ apart (centre-to-centre).

3.3.2 Model Verification

The final fully assembled model was placed in a lathe and indicators were used to verify the geometry of the cone. In particular, the half-angle of the cone was verified to be 5.06° and the steps at the two junctions (cone tip/cone tip holder and cone tip holder/cone sheet junctions) were measured to be less than $0.038 \pm 0.006 \text{ mm}$. Table 3.1 summarizes the angular distribution of the measured step heights. It is felt that these imperfections did not affect the results since previous studies by Germain (at the same freestream conditions) using much larger roughness elements (0.1 mm) at similar axial positions showed no observable effect on the transition location (see Section 4.4.7.1). There was some concern raised by Kendall's experiment [55] on a 4° half-angle cone at Mach 2.2

Table 3.1: Measured step heights at cone tip/cone tip holder (Junction A, $x = 75 \text{ mm}$) and cone tip holder/cone sheet (Junction B, $x = 148 \text{ mm}$) interfaces, respectively. All step height measurements are $\pm 0.006 \text{ mm}$. Positive quantities indicate forward facing steps, whereas negative quantities indicate backward facing steps. The angular locations are further defined in Figure 3.6.

Angle	Junction A (mm)	Junction B (mm)
0° (Weld)	0.000	0.025
90° (Smooth Surface)	0.013	-0.013
180° (Weld)	0.013	0.025
270° (Porous Surface)	0.013	0.038

in which the 54 mm nose tip was intentionally offset by 0.05 mm, resulting in a forward facing step on one side of the cone and a backward facing step on the other side. The transition Reynolds number along the two rays with no surface discontinuity was measured to be 4.7×10^6 while the forward facing step resulted in transition moving forward to a Reynolds number of 4.2×10^6 (*i.e.*, 11% lower than the Re_{tr} along the ray with no surface discontinuity). Similarly, the backward facing step resulted in transition moving forward to a Reynolds number of 3.0×10^6 (*i.e.*, 36% lower). It should be noted that Kendall's result should not be relevant to the present case, particularly in view of the different Mach numbers. In fact, Kendall's experiments were in a regime in which the first mode was the dominant mode and may be completely inapplicable to the present experiments. Furthermore, Kendall's unit Reynolds number was an order of magnitude larger than those in the present experiments and one would, therefore, expect the present results to be significantly less sensitive to similar roughness. Even if one were to attempt to apply Kendall's results to the present case, it is clear that the effect would not be relevant as follows. Assuming that Kendall's results can be simply scaled linearly, the forward facing step on the porous surface (whose height is 75% of Kendall's step height) would move transition forward by 8% while the backward facing step on the smooth surface (whose height is 25% of Kendall's step height) would move transition forward by 9%. Based on this, one might expect that the forward and backward facing steps on the present model would cause transition to occur at roughly the same location on both sides of the cone (but upstream of where transition should occur had there been no step). In any case, the most direct evidence that the steps had no effect on the transition location comes from Germain's surface roughness experiments and the fact that the present results reproduce the previous work by Germain and Adam whose model had no significant step (see Section 4.4). Furthermore, the effect of the porous surface is to delay transition by more than 100% in nitrogen (see Section 4.4.5.1) and it seems unlikely that the phenomenon would reverse itself in carbon dioxide if the step significantly affected the results (see Section 4.4.5.2).

As expected, there were highly localized imperfections along the welded seams of the cone sheet, even after the thermal interference fit assembly process. Figure 3.4 is a schematic diagram of a typical cross-section which shows approximately symmetric bumps on either side of the welded seams. The size of the bumps was approximately constant along the length of the cone such that the local increase in diameter was about 0.3 mm. It should

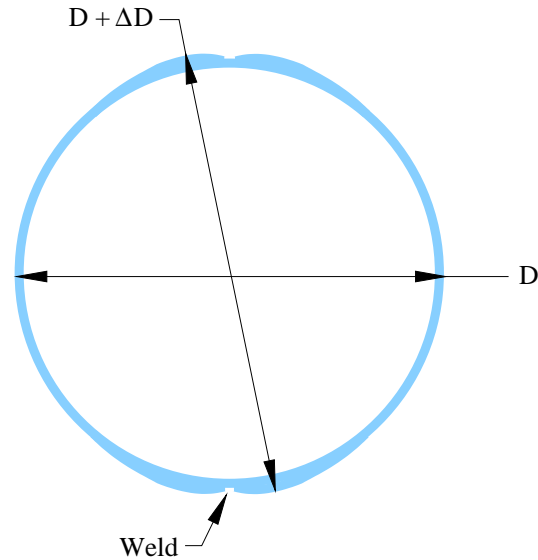


Figure 3.4: Schematic diagram showing the measured cross-section of the cone. Imperfections due to the welding process resulted in roughly symmetric bumps on either side of the welded seams (shown in exaggerated scale). The local increase in diameter (ΔD) was 0.3 mm and was approximately constant over the length of the cone.

be noted that this effect was very small. The cross-sectional diameter at the front edge of the cone sheet (where the effect was most pronounced) was 26.1 mm resulting in the bump height being less than 1% of the local diameter.

One significant imperfection was a small gap that existed between the cone sheet and the base cone. This gap was localized near the beginning edge of the cone sheet and was the result of imperfect rolling/welding of the cone sheet halves. This was of concern since the gap causes suction through the perforated sheet during the time it takes the test gas to fill the cavity between the cone sheet and the base cone. This would, of course, have a strong stabilizing effect on the boundary layer. After the pressure equalizes, however, the suction effect would no longer occur. The maximum gap height was measured to be less than 0.05 mm and extended no more than 50 mm downstream on the porous side of the cone only (*i.e.*, the affected area extended from approximately 150 mm to 200 mm as measured from the cone tip along the surface). This latter measurement was determined by pushing long, thin shims into the gap and measuring how far they could be inserted. The quoted numbers are considered to be conservative estimates and result in a maximum cavity volume of 0.3 cm³. The affected surface area was about 48 cm² resulting in approximately 480 000 holes connecting the gap to the freestream. Conservative estimates with an assumed cavity volume of 1 cm³ were performed. These calculations determined the mass flow rate through

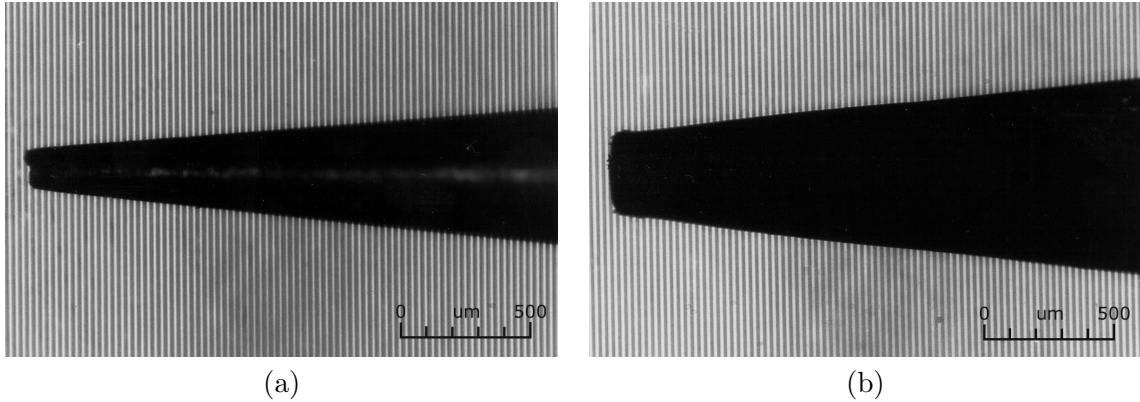


Figure 3.5: (a) Micrograph of a new, unused sharp cone tip with a measured radius of 0.076 ± 0.003 mm and (b) micrograph of a blunted cone tip with a measured radius of 0.130 ± 0.003 mm.

the holes assuming initially choked flow until the cavity pressure was raised such that the holes became unchoked. At that point, standard laminar pipe flow with an increasing back pressure was assumed and the resulting differential equation was solved. These calculations indicated that it would take approximately $25 \mu\text{s}$ to fill the gap. This is well within the 0.5 ms required for the nozzle to start and for steady flow to be established. Furthermore, data was never taken earlier than 1.0 ms after the start of the experiment allowing more than sufficient time for the gap to be filled and the pressure to be equalized. For this reason, it is felt that the small gap had no appreciable effect on the results.

The actual sharpness of the cone is an important consideration, particularly due to the sensitivity of the transition location to the nose tip radius. The tip of a sharp cone in hypervelocity flow sees extremely high heat loads at the stagnation point resulting in ablation and blunting over the course of the experiments. This blunting was noticed by Germain [38] and the use of molybdenum for the tip was an effort to minimize this effect. Measurements conducted by Germain (and independently confirmed in the present work) indicated that a new cone tip had a radius of 0.076 ± 0.003 mm and that it would stabilize to a ‘blunted’ radius of 0.130 ± 0.003 mm after several shots. Figures 3.5a and 3.5b show magnified images of new and blunted cone tips, respectively. Studies by Germain indicated that the effect of this minimal blunting on transition Reynolds number fell well within the overall error tolerance and therefore concluded that it was not relevant for this series of experiments. It should be noted that, in general, this statement is not correct and more significant nose blunting has been found to strongly affect the transition location.

3.3.3 Test Section Setup

As with Germain and Adam's experiments, the model was positioned such that the tip protruded approximately 330 mm into the nozzle during the test time. In the previous work, however, the model axis was deliberately placed approximately 64 mm above the nozzle centerline in order to maximize the length of the instrumented surface that was in the core flow (previous experiments only instrumented one longitudinal half of the model). For the present experiments, this was not acceptable since measurements were being made around the entire circumference of the model. The axis of the cone was aligned to within 1.5 mm of the centerline of the nozzle and it was at $0^\circ \pm 0.05^\circ$ angle-of-attack. Assuming a $M = 5$ flow, the expansion fan from the nozzle lip was estimated to impinge on the model at approximately 800 mm from the tip (*i.e.*, near thermocouple #25). The details of the alignment procedure are described by Germain [37].

3.3.4 Instrumentation

The model was instrumented with 56 Type E (constantan-chromel) flush-mounted coaxial thermocouples of which 52 (26 per side) were actually used to collect data since this was the maximum number of channels available on the data acquisition system. The thermocouples were arranged in a staggered pattern typically 24.5 mm apart with the first one located 255 mm and the last one located at 814 mm from the tip. All measurements of thermocouple locations are given as measurements along the surface of the cone (and not along the axial length). Figure 3.6 is a schematic diagram showing the location of the thermocouples on a developed view of half the cone (*i.e.*, the smooth surface side). The porous surface side had the mirror image of the same layout. It should be noted that the thermocouples were deliberately placed as far from the weld as possible with the closest one being placed along the 40 degree ray. This is deemed more than adequate since experiments by Mee [75] in hypervelocity flow over a flat-plate (conducted in the T4 facility at the University of Queensland) indicated that the spreading half-angle of turbulent bursts is approximately 3 to 4 degrees.

The small (2.5 mm diameter) and fast response ($1 \mu\text{s}$) thermocouples were manufactured in-house based on a modified design originally developed by Sanderson [101] and whose performance was tested in detail by Davis [24]. During the shot, the thermocouple signal

Thermocouple	Angle	Distance		Thermocouple	Angle	Distance	
		in	mm			in	mm
1	90	10.05	255.3	15	70	22.05	560.1
2	80	11.05	280.7	16	60	23.05	585.5
3	100	11.55	293.4	17	40	24.05	610.9
4	90	12.55	318.8	18	50	25.05	636.3
5	80	13.55	344.2	19	90	26.05	661.7
6	70	14.55	369.6	20	100	26.55	674.4
7	60	15.55	395.0	21	110	27.55	699.8
8	90	16.05	407.7	22	120	28.55	725.2
9	100	17.05	433.1	23	130	29.55	750.6
10	110	18.05	458.5	24	140	30.55	776.0
11	120	19.05	483.9	25	90	31.55	801.4
12	130	20.05	509.3	26	80	32.05	814.1
13	90	20.55	522.0	27	70	33.05	839.5
14	80	21.05	534.7	28	60	34.05	864.9

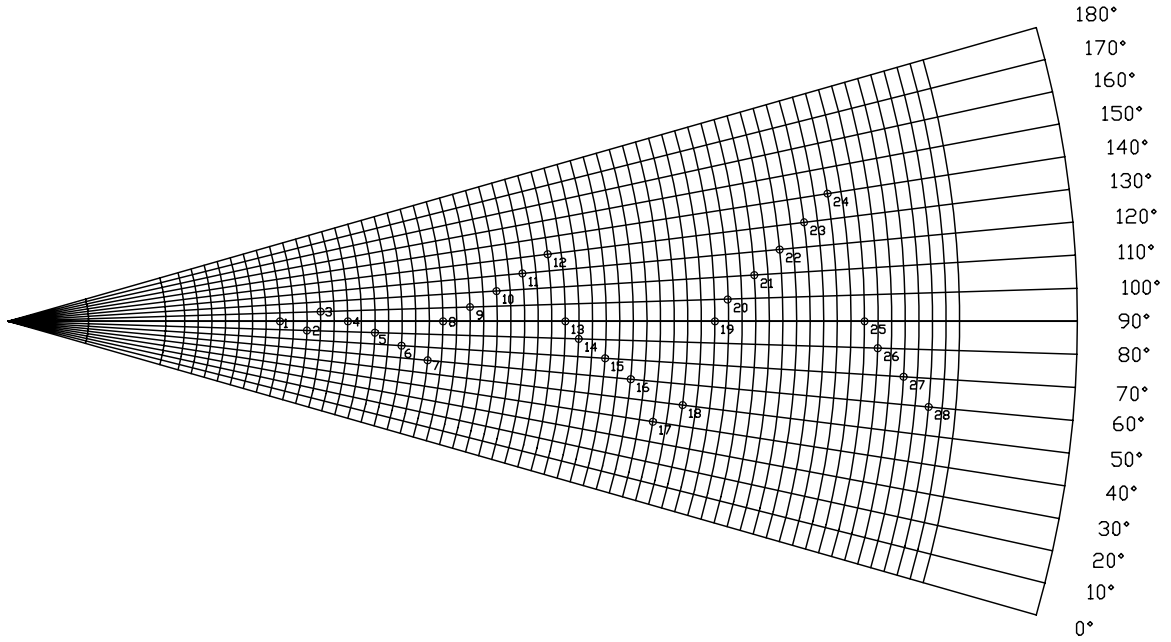


Figure 3.6: Schematic diagram showing the locations of the thermocouples on a developed view of half the cone (*i.e.*, the smooth side). The porous side has the mirror image of the same layout (*i.e.*, add 180° to the angular locations). The azimuthal lines are drawn at 12.7 mm (0.5 in) intervals with the second line located at 165 mm (6.5 in). The first line shows the location of the cone tip holder/cone sheet interface at 148 mm (5.8 in). All distances are measured along the surface of the cone (not along the axis).

was amplified by a factor of 500 and then sampled at 200 kHz. The sampled voltage levels were then converted to time histories of temperature rise using correlations for Type E thermocouples obtained from the National Institute of Standards and Technology [4].

3.4 T5 Soot Problem

One of the main concerns about this series of experiments was the fact that the model would be covered with a fine dusting of soot carried by the driver gas at the end of each shot. The soot is generated by the pyrolyzation of the polyurethane buffers used to stop the piston in this facility and arrives at the model after the useful test time. As expected, high enthalpy shots typically generate much more soot than lower enthalpy shots. This would potentially clog all the holes on the porous surface making it completely ineffective after the first experiment. If the holes didn't become clogged during the experiment, they certainly would become clogged during the traditional process of wiping the model with a towel after each shot. Preliminary test experiments performed on samples of the porous sheet were used to evaluate the effect of the particle contamination.

3.4.1 90° Flat Plate Test Piece

Worst case scenario tests were first performed by mounting a 10.2 x 7.6 cm (4.0 in x 3.0 in) sample of the porous sheet on a thick Plexiglas plate normal to the flow using the highest pressure and enthalpy conditions expected during the experiments (see Figure 3.7a). The purpose of the Plexiglas was to allow the porous sheet to be backlit so that it would be possible to determine whether the holes were clogged. After two shots, it was clear that the holes were indeed clogged and this sample was then used to evaluate different cleaning techniques including the use of solvents, commercially available degreasers, microbial enzyme cleaners designed to 'eat' carbon and high pressure blasts of air. Ultimately it was found that a commercially available water pressure washer (1300 psi) performed the best in terms of cleaning.

Figure 3.7b shows the test piece removed from the test section being backlit by natural sunlight. The left edge of the test piece was left uncleaned for comparison purposes. It was very dark because light could not pass through the piece, indicating that the holes were clogged. The right edge of the test piece was clearly allowing light to shine through and

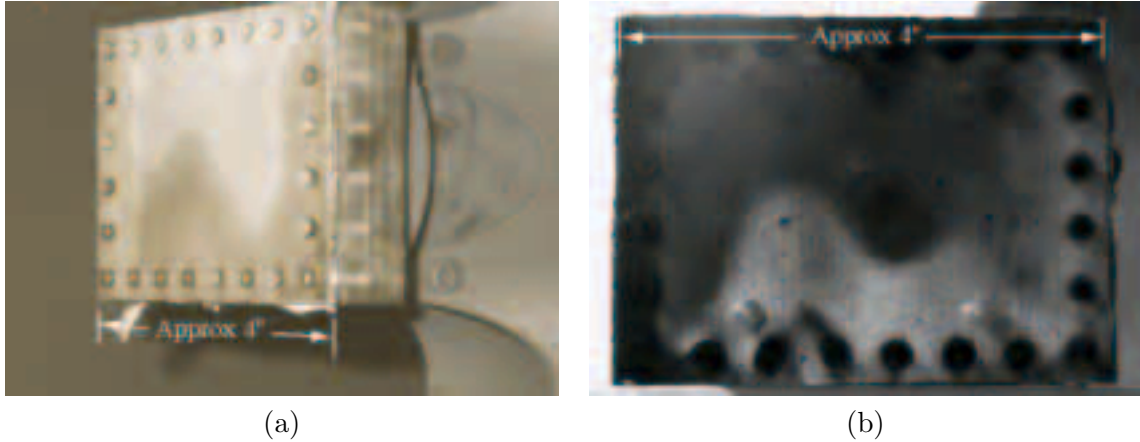


Figure 3.7: Photograph of the 90° flat plate test piece (a) mounted in the test section (b) being backlit by sunlight after two shots. The left edge of the backlit sample is dark indicating that the holes are clogged while the right edge of the sample (which has been cleaned) is bright indicating that the holes are not clogged.

provided strong evidence that the holes were not clogged. The difference was much more noticeable than indicated in this photograph. The middle of the plate appeared to allow a lot of light through (indicating that the holes were not clogged), but this section of the test piece was not usable since the porous sheet had lifted off the Plexiglas backing during the test run. The above test provided confidence since it established a procedure for cleaning the porous sheet in the event of unacceptable contamination.

3.4.2 5° Cylinder Test Piece

Further experiments were performed in which the porous sheet was mounted onto a Plexiglas cylinder angled at 5° to the flow to better simulate the conditions on the surface of the actual cone (see Figure 3.8a). Ideally, a small Plexiglas test cone should have been built, but a reasonable compromise was to use a cylinder to minimize cost. A hole was drilled down the centre of the cylinder to allow insertion of a small lightbulb to provide the backlight when viewed under a microscope. These tests revealed that there was very little clogging of the holes during the experiment and that it would be best not to clean the model after each shot. Figure 3.8b shows a micrograph of the backlit porous sheet after the test piece was subjected to two high enthalpy shots. The holes appear as white points of light, indicating that they were not clogged. This test provided reasonable evidence that the soot would most likely not be a problem on the actual cone. Based on this, it was decided to allow the soot to accumulate on the surface of the model over the course of this

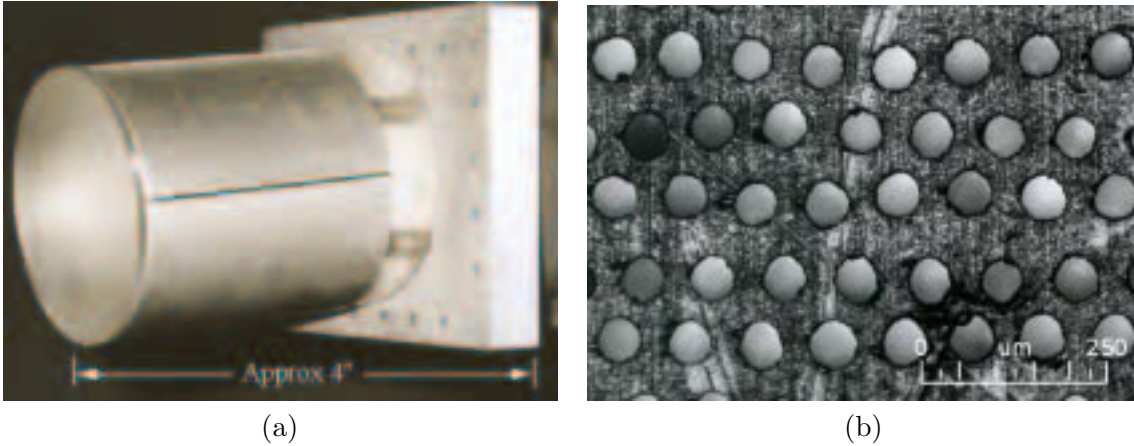


Figure 3.8: (a) Photograph of the 5° cylinder test piece mounted in the test section (b) Micrograph of the backlit sample after two high enthalpy shots showing that the holes are not clogged.

series of experiments. It will be shown in Section 4.4.6 that this minimal accumulation had no measurable effect on the transition location.

3.5 Heat Flux

A common technique for experimentally determining the state of the boundary layer is to compare the measured heat flux at each thermocouple location with values predicted by theoretical models for laminar and turbulent boundary layers. The heat flux for a turbulent boundary layer is typically significantly larger than that for a laminar boundary layer and the difference is easily noted. This is the technique that was used by both Germain [38] and Adam [2], and it was also the technique used in the present experiments.

A valid comparison can only be made if the data is reduced to suitable non-dimensional forms. The heat flux data is typically normalized into a Stanton number and the distance along the surface of the cone is typically normalized into a Reynolds number. Resulting plots of Stanton number versus Reynolds number can then be used to determine the state of the boundary layer at each thermocouple station and ultimately to determine the transition Reynolds number for a given experiment.

The Reynolds number is usually evaluated at the boundary layer edge conditions (denoted by the subscript e) and is defined as

$$Re_x = \frac{\rho_e U_e x}{\mu_e}, \quad (3.1)$$

where x is the distance measured along the surface of the cone, ρ_e is the edge density, U_e is the edge velocity, and μ_e is the edge dynamic viscosity. The Stanton number is typically defined as

$$St = \frac{\dot{q}(x)}{\rho_e U_e (h_{aw} - h_w)}, \quad (3.2)$$

where \dot{q} is the heat transfer rate, h_{aw} is the enthalpy assuming an adiabatic wall, and h_w is the enthalpy at the wall. This expression can be simplified by recognizing that the adiabatic wall enthalpy can be expressed as

$$h_{aw} = h_e + r(h_o - h_e), \quad (3.3)$$

where h_o is the stagnation enthalpy, h_e is the edge enthalpy and r is the recovery factor. In addition, recognizing that the wall enthalpy is negligible since the short test duration causes the wall temperature to remain essentially at room temperature, the final form of the Stanton number is

$$St = \frac{\dot{q}(x)}{\rho_e U_e [h_o - \frac{1}{2} U_e^2 (1 - r)]}. \quad (3.4)$$

As suggested by Anderson [3], the recovery factor is typically taken to be $r_{\text{lam}} = \sqrt{Pr}$ for laminar boundary layers and $r_{\text{turb}} \simeq \sqrt[3]{Pr}$ for turbulent boundary layers where Pr is the Prandtl number, assumed to be constant here. As reported by White [132], these approximations for the recovery factor have been experimentally shown to be valid by Mack [68].

3.5.1 Theoretical Heat Flux

The approach used to estimate the theoretical laminar and turbulent boundary layer heat flux is the same as the one used by the previous researchers. The development of these models, given in Germain [37] and Adam [1], is summarized below. Further details can also be found in White [132]. The final desired result is a $St - Re$ relationship that can be compared with experimental data on plots of Stanton number versus Reynolds number.

The starting point for both the laminar and turbulent boundary layer heat flux models is the Reynolds analogy which relates the Stanton number to the local skin friction coefficient. For a flat-plate zero-pressure gradient (laminar or turbulent) boundary layer, the Reynolds

analogy can be expressed as

$$St = \frac{1}{2}C_f Pr^{-2/3}, \quad (3.5)$$

where the skin friction coefficient (C_f) is the non-dimensional form of the wall shear stress (τ_w) and is defined as

$$C_f(x) = \frac{\tau_w(x)}{\frac{1}{2}\rho_e U_e^2}. \quad (3.6)$$

The Prandtl number is well known for the gases under consideration, so the desired Stanton number - Reynolds number relationship can be obtained by determining suitable expressions for C_f as a function of Re_x for both the laminar and turbulent boundary layers. The derivation of these expressions is described in the following sections.

3.5.1.1 Laminar Theory

The approach taken for the laminar theory is to start with the standard incompressible flat-plate boundary layer result and apply suitable modifications to extend the result to frozen, non-catalytic, compressible, and axisymmetric flow representative of the experiments. Note that the assumption of frozen flow results in a lower limit for the expected laminar heat flux since the actual chemically reacting flow can have significant additional heat flux due to recombination reactions at the wall.

The skin friction coefficient for the incompressible, flat-plate, two-dimensional, zero-pressure gradient Blasius boundary layer is well known to be

$$C_{f_{inc}}(x) = \frac{0.664}{\sqrt{Re_x}}, \quad (3.7)$$

where Re_x is the Reynolds number based on the distance x from the leading edge of the flat-plate. The effects of compressibility are typically introduced using a correction factor known as the Chapman-Rubesin parameter [15] ($C_w = \rho_w \mu_w / \rho_e \mu_e$) evaluated at the wall. The expression of the skin friction coefficient then becomes

$$C_{f_{comp}}(x) \simeq \frac{0.664}{\sqrt{Re_x}} \sqrt{C_w}. \quad (3.8)$$

As mentioned by White [132], the above relation yields good agreement for adiabatic walls, but not for hot or cold walls. The suggested correction for this is to evaluate the Chapman-

Rubesin parameter at a reference temperature (T^*) which is a better representation of the conditions in the boundary layer. The most commonly used expression for T^* was introduced by Eckert [29] as

$$\frac{T^*}{T_e} = 0.5 + 0.22 r \frac{\gamma - 1}{2} M_e^2 + 0.5 \frac{T_w}{T_e}. \quad (3.9)$$

The above was obtained as a semi-empirical correlation with exact flat-plate boundary layer solutions for air. Substituting typical values of $\gamma = 1.4$ and $Pr = 0.8$, one obtains the commonly used relation given in White [132]:

$$\frac{T^*}{T_e} = 0.5 + 0.039 M_e^2 + 0.5 \frac{T_w}{T_e}. \quad (3.10)$$

Although the above relation was obtained specifically for air, Eckert [29] suggested that it seemed reasonable to use it for other gases as well. A more general relation obtained by Dorrance [28] from similarity relations for compressible flow is

$$\frac{T^*}{T_e} = 0.5 + \frac{\gamma - 1}{2} \frac{r}{6} M_e^2 + 0.5 \frac{T_w}{T_e}. \quad (3.11)$$

For the present work, Equation 3.10 was used for air and nitrogen test gases while Equation 3.11 was used for carbon dioxide. Now, redefining the Chapman-Rubesin parameter $C^* = \rho^* \mu^* / \rho_e \mu_e$, where the * quantities are evaluated at the reference temperature, one obtains

$$C_{f_{comp}}(x) \simeq \frac{0.664}{\sqrt{Re_x}} \sqrt{C^*}. \quad (3.12)$$

As described in White [132], the above flat-plate result can be applied to a cone by using the Lees-illingworth transformation (similar to the incompressible Mangler transformation) to obtain the result

$$C_{f_{cone}} = \sqrt{3} C_{f_{plate}}. \quad (3.13)$$

This gives the final desired Stanton number - Reynolds number relationship

$$St \simeq \frac{0.664 \sqrt{3}}{2} \frac{\sqrt{C^*}}{Pr^{2/3} \sqrt{Re_x}}, \quad (3.14)$$

which is valid for a frozen, non-catalytic, compressible, laminar boundary layer on a cone.

3.5.1.2 Turbulent Theory

The approach used for the turbulent model is similar to that used for the laminar model. In this case, an exact expression for the incompressible skin friction coefficient does not exist. As described in White [132], a modified version of the ‘inner variable approach’ suggested by Kestin and Persen [57], however, yields the excellent approximate relation

$$C_{f_{inc}} \simeq \frac{0.455}{\ln^2(0.06 Re_x)}. \quad (3.15)$$

As before, the effects of compressibility are introduced by suitably modifying the incompressible result. The ‘compressibility transformation’ for a turbulent boundary layer, however, is slightly more complicated than in the laminar case. A standard form for this transformation used by many flat-plate theories was suggested by Spalding and Chi [109] and is given by

$$C_{f_{comp}} = \frac{1}{F_c} C_{f_{inc}}(Re_x F_{Re}), \quad (3.16)$$

where F_{Re} is a Reynolds number ‘stretching’ factor and F_c is an additional skin friction correction factor. Applying the above transformation to Equation 3.15, one obtains

$$C_{f_{comp}} = \frac{1}{F_c} \frac{0.455}{\ln^2(0.06 Re_x F_{Re})}. \quad (3.17)$$

The above flat-plate relationship must be modified in order to be applied to the case of flow over a cone. Once again, an exact transformation does not exist. An approximate turbulent cone rule, however, was derived by van Driest [129] by integrating the momentum equation for axisymmetric flow with the assumption that the friction coefficient and the momentum thickness were related by a power law. This analysis yielded an increase in the skin friction coefficient of about 10% for turbulent flow over a cone as opposed to a flat-plate. The final desired $St - Re$ relationship is thus given by

$$St = \frac{1}{2} \frac{1.1}{Pr^{2/3}} \frac{0.455}{F_c \ln^2(0.06 Re_x F_{Re})}, \quad (3.18)$$

where F_c and F_{Re} remain to be determined. The evaluation of these two factors is, in fact, what differentiates many of the proposed theories. The two that are considered in the present work (and were used in the previous work by Germain [38] and Adam [2]) are the

van Driest-II model [130] and the White and Christoph model [133]. A concise summary of the development of both theories is given in White [132]. The theory proposed by van Driest uses an integration of the Kármán integral relation with assumed density and velocity profiles based on an eddy viscosity model. White and Christoph's theory extends the 'inner variable approach' used earlier to compressible flow and yields more accurate results for cold-wall flows. For both theories, the resulting expression for F_c is the same and is given by

$$F_c = \frac{T_{aw}/T_e - 1}{(\sin^{-1} A + \sin^{-1} B)^2}, \quad (3.19)$$

where A and B are given by

$$A = \frac{2a^2 - b}{\sqrt{b^2 + 4a^2}}, \quad B = \frac{b}{\sqrt{b^2 + 4a^2}}, \quad (3.20)$$

and a and b are given by

$$a = \sqrt{\frac{\gamma - 1}{2} M_e^2 \frac{T_e}{T_w}}, \quad b = \frac{T_{aw}}{T_w} - 1. \quad (3.21)$$

The expression for F_{Re} , however, is different for the two theories. According to the van Driest-II theory the expression for the Reynolds number stretching factor is

$$F_{Re} = \frac{1}{F_c} \frac{\mu_e}{\mu_w}, \quad (3.22)$$

while in the White and Christoph theory it is given by

$$F_{Re} = \frac{1}{\sqrt{F_c}} \frac{\mu_e}{\mu_w} \sqrt{\frac{T_e}{T_w}}. \quad (3.23)$$

For the present work, both of the above theories were found to be in close agreement and were used throughout the analysis of the experimental data.

3.5.2 Experimental Heat Flux

In general, the heat flux to a surface can be determined at discrete locations from the time resolved temperature traces measured by thermocouples. For the present experiments, since the test time was so short, the thermal penetration depth was quite small and it was sufficient to assume one-dimensional unsteady heat conduction in a semi-infinite solid with

constant thermal properties. This is described by the following linear partial differential equation and boundary conditions:

$$\frac{\partial^2 T}{\partial y^2} = \frac{1}{\alpha} \frac{\partial T}{\partial t}, \quad (3.24)$$

$$T(y, 0) = T_i, \quad T(0, t) = T_i + \Delta T(t), \quad (3.25)$$

$$\left. \frac{\partial T(t)}{\partial y} \right|_{y \rightarrow \infty} = 0, \quad \left. \frac{\partial T(t)}{\partial y} \right|_{y=0} = \dot{q}(t), \quad (3.26)$$

where T is the temperature, y is the distance normal to the surface, $\alpha = k/\rho C_p$ is the thermal diffusivity (k is the thermal conductivity, ρ is the density, and C_p is the specific heat at constant pressure), and \dot{q} is the heat flux.

A number of approaches exist to solve the above problem and the relative merits of each are described in detail in Appendix B of Davis [24]. The first method, known as the ‘direct method’, developed by Schultz and Jones [107], uses Laplace transforms to directly obtain the heat flux as a function of surface temperature. Another technique, known as the ‘indirect method’, is attributed to Kendall *et al.* [54]. This involves first integrating the time-resolved surface temperature to obtain the total heat transferred to the surface (the ‘integrated heat’) and then taking the derivative of this to obtain the heat transfer rate. An inherent feature of this approach is that the integration automatically smooths the time-resolved data, effectively acting as a filter. This latter technique was used by both Germain [38] and Adam [2] to calculate the heat flux.

For the present experiments, a spectral deconvolution method using fast Fourier transforms implemented by Sanderson [101] was used. The advantages of this technique are that it is much faster to compute and it allows more control over the signal noise filtering. The details of this technique are given in Sanderson [101] and Davis [24], and are summarized below.

Recognizing that the governing partial differential equation is linear, the transient solution of this system can be described by the convolution integral

$$\Delta T(y, t) = \int_0^t g(y, t - \tau) \dot{q}(\tau) d\tau, \quad (3.27)$$

where the unit impulse response function, $g(x, t)$, is

$$g(y, t) = \sqrt{\frac{\alpha}{\pi k^2 t}} \exp\left(\frac{-y^2}{4\alpha t}\right); \quad t > 0. \quad (3.28)$$

Fast Fourier transform techniques described in Press *et al.* [89] allow the heat flux to be determined from the measured noisy, discrete, time-resolved surface temperature data. The measured signal, $s(t)$, is assumed to consist of the actual temperature, $\Delta T(t)$, and an uncorrelated noise component, $n(t)$. The resulting expression for the heat transfer is

$$\dot{q}(t) = FFT^{-1} \left[\frac{S(f) \Phi(f)}{G(f)} \right], \quad (3.29)$$

where capital letters are used to denote the fast Fourier transforms of the given quantities and $\Phi(f)$ is the least-squares optimal filter given by

$$\Phi(f) = \frac{|S(f)|^2 - |N(f)|^2}{|S(f)|^2}. \quad (3.30)$$

As described by Davis [24], for these experiments, it is difficult to characterize the noise spectrum, $|N(f)|^2$, and for this reason a simple low-pass filter is used with a typical cut-off frequency of 20 kHz. This is adequate since the temperature data of interest consists almost entirely of low frequencies (less than 10 kHz) and, regardless, the 3 dB bandwidth of the amplifiers is 50 kHz.

As indicated previously, the above analysis assumed constant thermal properties, but these values have yet to be defined. For the purpose of this analysis, it has been shown by Davis that it is adequate to use values of α and k that are the averages of the properties of constantan and chromel at 300 K. These average values were determined to be $\alpha = 5.49 \times 10^{-6} \text{ m}^2/\text{s}$ and $k = 20 \text{ W}/\text{m}^\circ\text{C}$ and were based on the thermal properties of constantan and chromel documented in Sundqvist [125]. The final quantity required, the thermocouple junction depth y , was measured by Davis [24] to be approximately $1 \text{ }\mu\text{m}$.

3.5.3 Heat Flux Results

A typical measured temperature data trace and its corresponding time-resolved heat flux trace are shown in Figure 3.9. The heat flux data trace shows an initial spike corresponding to the nozzle starting process and then drops to an approximately constant level

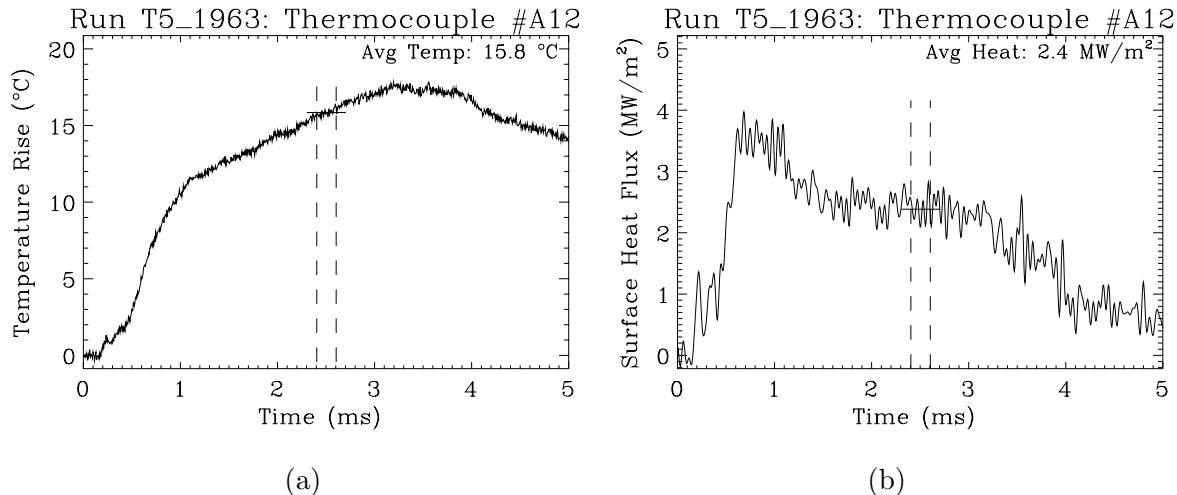


Figure 3.9: Representative time-resolved (a) temperature data trace and (b) the corresponding heat flux trace computed using the spectral method. The heat flux level was obtained by averaging over a suitable time interval during which steady flow had been established.

as the steady flow establishes itself. The time $t = 0$ corresponds to the pressure rise in the stagnation region of the shock tube as measured by the pressure transducers $P_{o, \text{North}}$ and $P_{o, \text{South}}$. Comparisons of the heat flux computed by the indirect method (used by Germain [38] and Adam [2]) and the spectral method (used for the present experiments) were performed for several experiments to verify that they were in agreement.

Spatial distributions of the heat flux along the porous and smooth surfaces of the cone were obtained by averaging the time-resolved heat flux at each thermocouple station over an appropriate interval. This interval varied from shot to shot and was selected such that it was after the nozzle starting process, before the onset of driver gas contamination, and always within the constant reservoir pressure window. The averaging window (or interval length) used was typically $200 \mu\text{s}$ at higher enthalpies and $500 \mu\text{s}$ at lower enthalpies. Note that, for a given experiment, all the thermocouples were averaged over the same time interval to insure a valid comparison.

The boundary layer edge conditions were used to compute the Stanton number in order to non-dimensionalize the heat flux data. Following the same analysis as Germain [38] and Adam [2], they were computed using the classical Taylor and Maccoll [127] solution for supersonic flow over a cone. Inherent in this calculation was the assumption that the gas composition remained frozen from the freestream, across the weak conical attached shock and to the boundary layer edge. Viscosities were calculated using a simple code based on

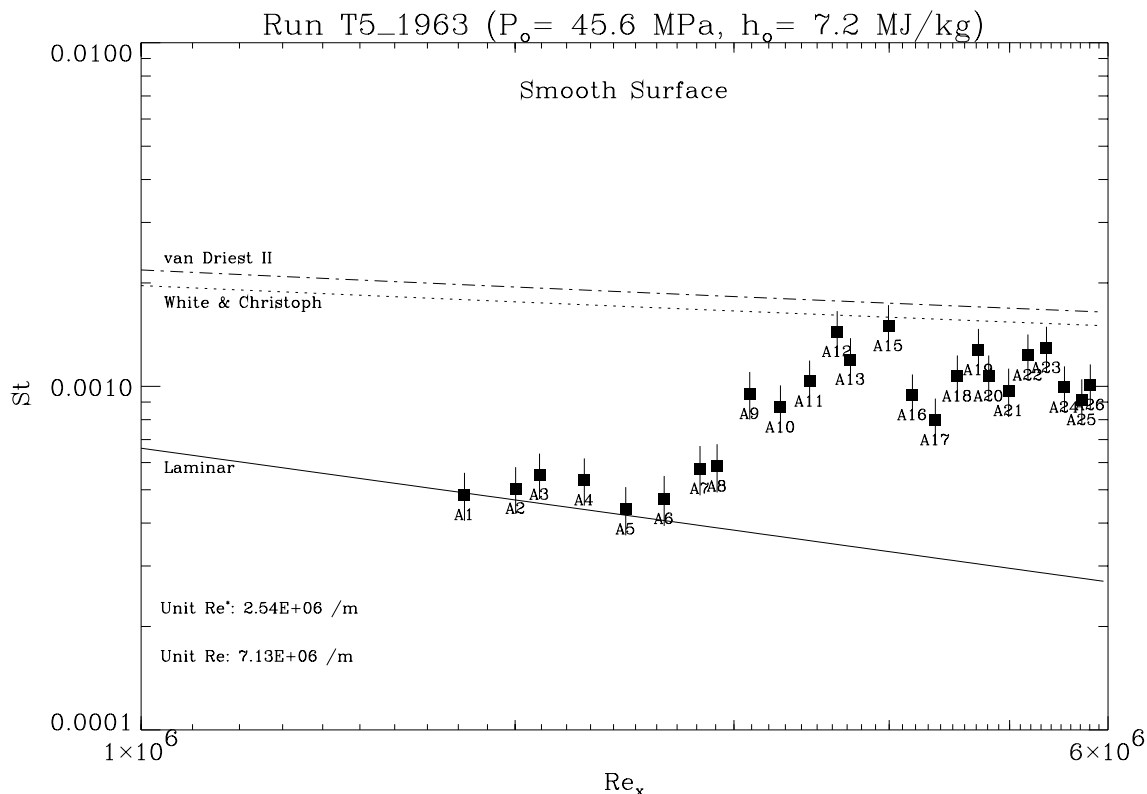


Figure 3.10: Non-dimensional plot of the spatial heat flux distribution (Stanton number versus Reynolds number) along the smooth surface during shot 1963. The solid line is the theoretical estimate for a frozen, non-catalytic laminar boundary layer. The dashed-dotted and dotted lines are the theoretical estimates for the van Driest II and White & Christoph turbulent boundary layer models, respectively. For this shot, it can be seen that the boundary layer is initially laminar and then transitions to a turbulent boundary layer.

a viscosity model for reacting gases developed by Blottner *et al.* [10] in order to determine the viscosity of each species in the gas mixture. Coefficients for the model for the different gases were obtained from Olynick *et al.* [83]. Using the computed gas composition, the code then used Wilke's [134] semi-empirical mixing rule to calculate the overall viscosity of the gas mixture.

Figure 3.10 shows the non-dimensional spatial distribution of the heat flux along the smooth surface of the cone during shot 1963 in a plot of Stanton Number versus Reynolds number. The plot also shows the theoretical estimates for the laminar and turbulent boundary layer heat flux which were computed as described in Section 3.5.1. For this particular shot, it can be seen that the boundary layer was initially laminar and then transitioned to a turbulent boundary layer further downstream.

3.5.3.1 Uncertainty Analysis

The uncertainty in the Stanton number was computed based on the uncertainty in the dimensional heat flux ($\pm 13\%$ to $\pm 18\%$), the stagnation enthalpy ($\pm 8\%$), the edge velocity ($\pm 4\%$), and the edge density ($\pm 8\%$). The details of the estimation of these uncertainties are presented below. The final uncertainty in the Stanton number for each thermocouple ranged from about $\pm 18\%$ to $\pm 22\%$.

Heat Flux (\dot{q}): The most significant contribution to the uncertainty in the heat flux was the high frequency electrical noise generated in the amplifiers that is evident in the time-resolved heat flux data trace. This became particularly severe at lower enthalpies where the signal-to-noise ratio was decreased significantly due to the lower heat flux levels. It was alleviated somewhat by using a lower cut-off frequency (15 kHz) in the low-pass filter when computing the heat flux and by increasing the averaging window to 500 μs for the lower enthalpy conditions. The uncertainty due to this noise was estimated as the error in the mean value of the heat flux using the 2σ (95%) confidence level:

$$\varepsilon_{EN} = \frac{1.96S_x}{\sqrt{n}}, \quad (3.31)$$

where ε_{EN} is the percent error, S_x is the standard deviation and n is the number of data points used in computing the average heat flux. This value was found to range from 10% to 15%, depending on the run condition. Other sources of uncertainty (also at the 95% confidence level) included the digitizer accuracy ($\pm 0.5\%$) and amplifier gain accuracy ($\pm 1.5\%$) as stated by the manufacturer, the uncertainty in the voltage-to-temperature correlations for E-type thermocouples ($\pm 1.7\%$) suggested by NIST, and the uncertainty in the thermal properties of constantan and chromel ($\pm 8\%$) suggested by Davis [24]. The resulting uncertainty for the dimensional heat flux ranged from about $\pm 13\%$ to $\pm 18\%$.

Stagnation Enthalpy (h_o): As described in Section 3.2.3, the stagnation enthalpy was calculated using the StanJan or ESTC code with shock speed (u_s), initial shock tube pressure (P_{ST}), initial shock tube temperature (T_{ST}) and measured stagnation pressure (P_o) as inputs. This can be expressed in the following functional form

$$h_o = h_o(u_s, P_{ST}, T_{ST}, P_o), \quad (3.32)$$

resulting in the following expression for the percent uncertainty

$$\varepsilon_{h_o}^2 = \left[\left(\frac{u_s}{h_o} \frac{\partial h_o}{\partial u_s} \right) \varepsilon_{u_s} \right]^2 + \left[\left(\frac{P_o}{h_o} \frac{\partial h_o}{\partial P_o} \right) \varepsilon_{P_o} \right]^2, \quad (3.33)$$

where ε is used to represent the uncertainty in the respective quantities and the contributions to the uncertainty due to P_{ST} and T_{ST} were assumed to be negligible. The ε_{u_s} was estimated to be $\pm 4\%$ based on the average decrease (over several shots) in shock velocity measured by the shock timing stations (ST_3 and ST_4) and the value measured between ST_4 and P_o . The partial derivative ($\partial h_o / \partial u_s$) was estimated based on the relation $h_o \simeq u_s^2$ resulting in

$$\frac{u_s}{h_o} \frac{\partial h_o}{\partial u_s} = 2. \quad (3.34)$$

The ε_{P_o} was estimated to be $\pm 2\%$ and included the error in the mean of the measured stagnation pressure assuming a 95% confidence level using an equation similar to Equation 3.31 ($\pm 1\%$), the voltage-to-pressure conversion ($\pm 2\%$), and the digitizer accuracy ($\pm 0.5\%$). The partial derivative ($\partial h_o / \partial P_o$) was estimated by running the ESTC code multiple times for different run conditions while slightly perturbing the input stagnation pressure (P_o). The average value of the coefficient in parentheses was 0.2, resulting in the P_o having a negligible contribution to overall uncertainty in h_o . The final uncertainty in h_o was about $\pm 8\%$.

Edge Velocity (U_e): The uncertainty in edge velocity was assumed to be the same as the uncertainty in the freestream velocity (U_∞) which, to rough estimate, is

$$U_\infty \sim \sqrt{2h_o}. \quad (3.35)$$

The resulting equation for the uncertainty is

$$\varepsilon_{U_e} \simeq \varepsilon_{U_\infty} = \frac{1}{2} \varepsilon_{h_o}. \quad (3.36)$$

Substituting in the value for ε_{h_o} determined above, the final uncertainty in U_e was estimated at $\pm 4\%$.

Edge Density (ρ_e): The uncertainty in edge density was also assumed to be the same

as the uncertainty in the freestream density (ρ_∞). The freestream density was calculated using the NENZF code using stagnation pressure (P_o), stagnation enthalpy (h_o), and area ratio as inputs. This can be expressed in the functional form

$$\rho_\infty = \rho_\infty(P_o, h_o, \text{Area Ratio}), \quad (3.37)$$

resulting in the expression for percent uncertainty

$$\varepsilon_{\rho_e}^2 \simeq \varepsilon_{\rho_\infty}^2 = \left[\left(\frac{P_o}{\rho_\infty} \frac{\partial \rho_\infty}{\partial P_o} \right) \varepsilon_{P_o} \right]^2 + \left[\left(\frac{h_o}{\rho_\infty} \frac{\partial \rho_\infty}{\partial h_o} \right) \varepsilon_{h_o} \right]^2, \quad (3.38)$$

where the uncertainty in the area ratio was assumed negligible. The coefficients in parentheses were estimated by running the NENZF code multiple times for different run conditions while slightly perturbing the input stagnation pressure (P_o) and stagnation enthalpy (h_o) to estimate the derivatives. The average values for the quantities in parentheses ranged from 0.8 to 1.1, and a value of 1.0 was deemed adequate for the purpose of this analysis. The resulting uncertainty for the edge density was approximately $\pm 8\%$.

Chapter 4 Experimental Results

This chapter details the results obtained from the present experiments. It first outlines the test conditions, details the method used to determine the transition Reynolds number and describes the effects of enthalpy on transition observed by previous researchers. These results are extended to the porous surface and its effectiveness in delaying transition is then discussed.

4.1 Test Conditions

A total of 29 shots were carried out in nitrogen and 19 shots were performed in carbon dioxide. The nitrogen shots were performed with reservoir pressures ranging from 11 MPa to 50 MPa and specific reservoir enthalpies ranging from 3.0 MJ/kg to 13 MJ/kg. Above 13 MJ/kg, the Reynolds numbers achieved in T5 were too low to observe transition on the cone. Nitrogen was selected as the initial test gas in order to minimize the effects of chemistry, which were not included in Fedorov and Malmuth's analysis. The carbon dioxide shots were performed with reservoir pressures ranging from 9.0 MPa to 40 MPa with specific reservoir enthalpies ranging from 1.3 MJ/kg to 9.0 MJ/kg. The stagnation, freestream and edge conditions for all the shots are summarized in Appendix A.

4.2 Determination of Transition Reynolds Number (Re_{tr})

As described in Section 3.5.3, the spatial heat transfer distribution on the cone was expressed in plots of Stanton number versus Reynolds number for each shot. Figure 4.1 shows such a plot for shot 1963 in nitrogen test gas. On this plot, each point represents the non-dimensional time-averaged heat flux value (or St) for the thermocouple at that particular non-dimensional location (or Re_x) with uncertainties ranging from about $\pm 18\%$ to $\pm 22\%$ as described in Section 3.5.3.1. The Reynolds number (Re_x) and Stanton number (St) used here are defined in Section 3.5. The state of the boundary layer was determined by comparing the experimental results with theoretical models. The dashed-dotted and dotted lines

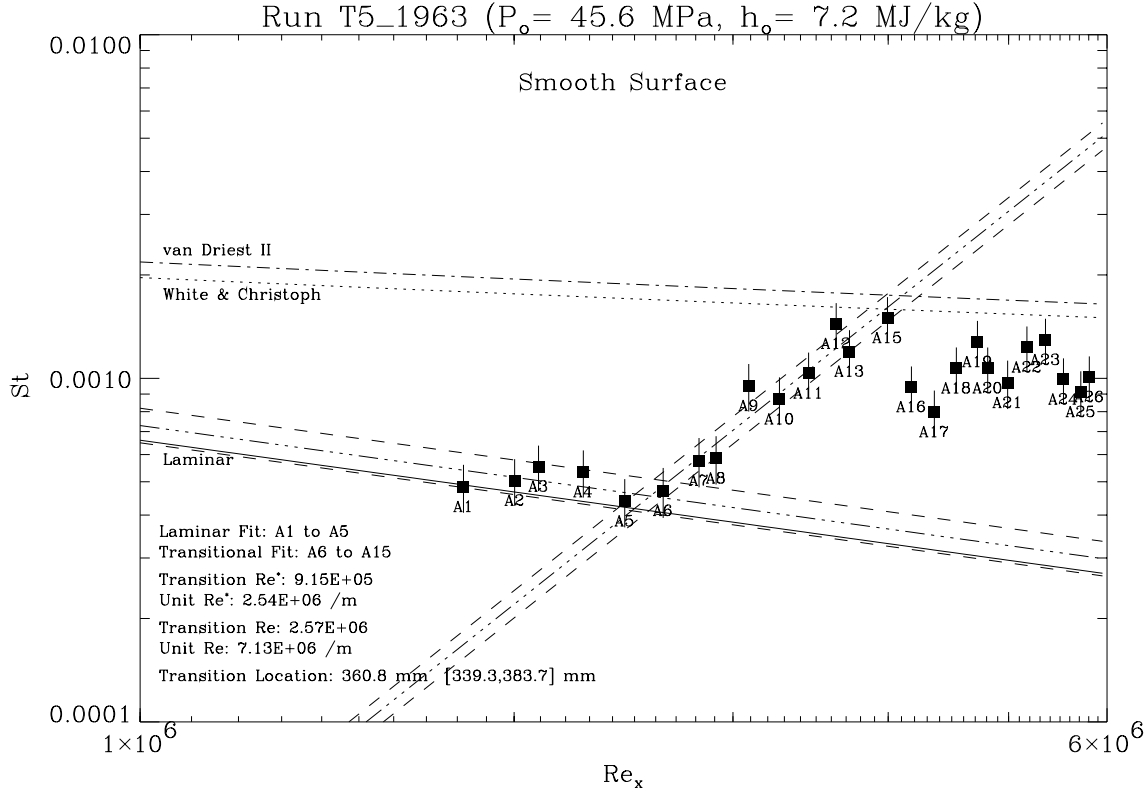


Figure 4.1: Non-dimensional plot of the spatial heat flux distribution (Stanton number versus Reynolds number) along the smooth surface during shot 1963. The solid line is the theoretical estimate for a frozen, non-catalytic laminar boundary layer. The dashed-dotted and dotted lines are the theoretical estimates for the van Driest II and White & Christoph turbulent boundary layer models, respectively. For this shot, it can be seen that the boundary layer is initially laminar and then transitions to a turbulent boundary layer. The dashed-triple-dotted lines are the fits of the experimental data and the intersection of these two lines is defined to be the transition Reynolds number. The dashed lines above and below the experimental fits are the error bounds on the lines and their intersections define an ‘error rhombus’ for the transition location.

represent the expected heat flux (or St) for a turbulent boundary layer as computed using the semi-empirical models developed by Van Driest and White & Christoph, respectively. The solid line represents the theoretical St versus Re_x relationship for a frozen, non-catalytic laminar boundary layer. These theoretical models are detailed in Section 3.5.1.

The transition location was determined by first fitting a line through the data points in the laminar region (the dashed-triple dotted line just above solid (laminar) line) while enforcing the $Re_x^{-0.5}$ law expected for a zero-pressure gradient laminar boundary layer. The parallel dashed lines above and below the fitted laminar line represent the uncertainty in the fit which was determined assuming the 95% confidence level using the small sample T-distribution. A positive slope line was then fitted through the data points in the transi-

tional region (the other dashed-triple dotted line) and once again, the dashed lines above and below the fitted transition line represent the uncertainty in the fit. The intersection of the fitted laminar and transitional lines was defined as being the transition Reynolds number and the intersection of the dashed lines (uncertainties in the experimental fits) defined the ‘error rhombus’. Note that the error rhombus actually sets the bounds on the transition location, and not the transition Reynolds number, since the uncertainties in density, velocity and viscosity have not been explicitly accounted for at this point. The minimum and maximum vertices (in terms of abscissa coordinates) of the error rhombus were used as the lower and upper uncertainty bounds for the transition location. The average percent error of these two values was used as the estimate for uncertainty in transition location. This uncertainty varied from shot to shot, but it ranged from $\pm 3\%$ to $\pm 15\%$, depending on the slope of the transitional fit. Factoring in the additional uncertainty (refer to Section 3.5.3.1) due to density ($\pm 8\%$), velocity ($\pm 4\%$) and viscosity ($\pm 5\%$), the overall uncertainty in transition Reynolds number ranged from $\pm 11\%$ to $\pm 19\%$, with a median of $\pm 13\%$. The information in the bottom left corner of the plot indicates which points were used for the laminar and transitional fits, as well as the estimated transition Reynolds number and transition location. The values in square brackets after the transition location are the minimum and maximum vertices for the error rhombus.

The points included in the laminar and transitional fits were chosen by inspection using the theoretical heat flux models as rough guides. The selection of the points for the laminar fit was additionally aided by the use of plots of the cumulative sum of recursive residuals (W_t). A residual is the error between the actual data point and the predicted value based on a linear regression using all the desired data points. The recursive residual (w_r) is the prediction error for the t^{th} data point when the regression coefficients are computed using only the first $t - 1$ data points. This technique is known as the ‘Cumulative Sum (CUSUM)’ technique and is used in time-series analysis of economic data to detect the data point at which a change in slope occurs in the underlying data. It is analogous to the present case where time is replaced by the Reynolds number. Details of this approach can be found in Greene [42]; however, the general idea is that the cumulative sum of recursive residuals will deviate from zero when the ‘change point’ is detected. A proper statistical test was devised by Brown *et al.* [12], but it has very low statistical power and is generally not useful. In fact, Brown indicates that the main value of this approach is

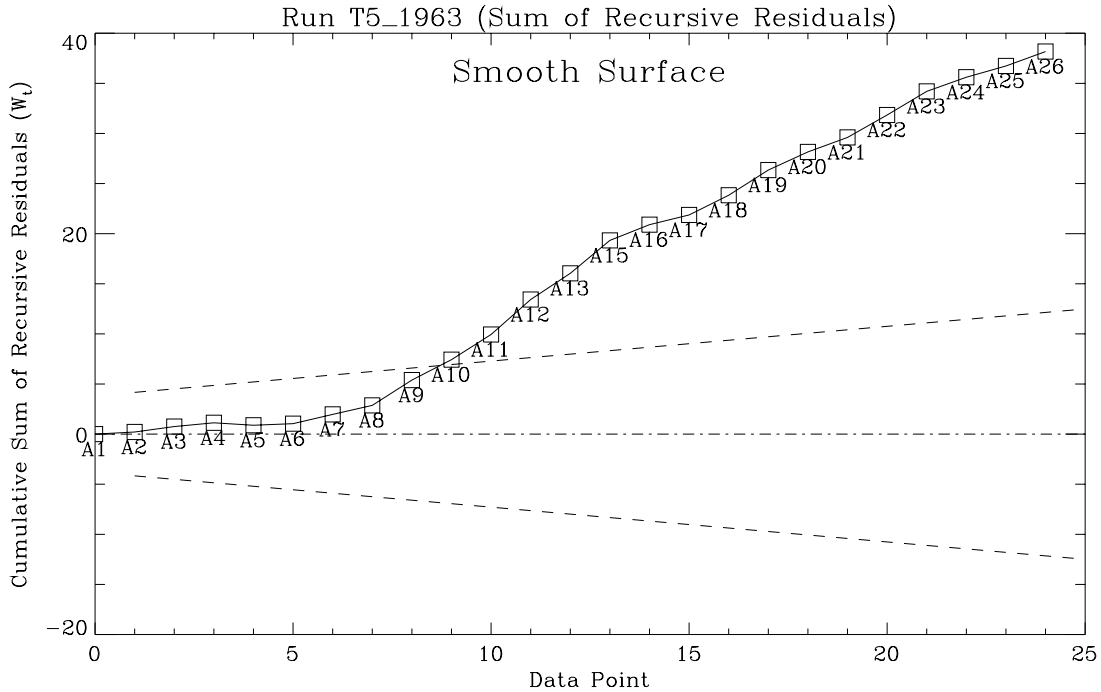


Figure 4.2: Plot of cumulative sum of recursive residuals for the smooth surface for shot 1963. The dashed lines represent the 90% confidence interval using the test proposed by Brown [12].

to simply examine the plot of the cumulative sum of recursive residuals to determine the change point by inspection. Figure 4.2 shows such a plot for shot 1963. The change point is clearly seen to occur near thermocouple A6. The dashed lines represent the 90% confidence interval determined using the test proposed by Brown [12]. As indicated previously, this test has low power and is only able to indicate that the slope has changed (in a statistically significant sense) after thermocouple A10. It should be noted that including fewer or more points in the laminar fit did not significantly change the transition location.

4.3 Enthalpy Effects on Transition

Up until now, the non-dimensional quantities have been evaluated at the boundary layer edge conditions. In particular, the transition Reynolds number has been calculated as

$$Re_{tr} = \frac{\rho_e U_e x_{tr}}{\mu_e}. \quad (4.1)$$

This approach was adequate for determining the transition location using the method outlined in Section 4.2. One of the main results, however, obtained by Germain [38] and

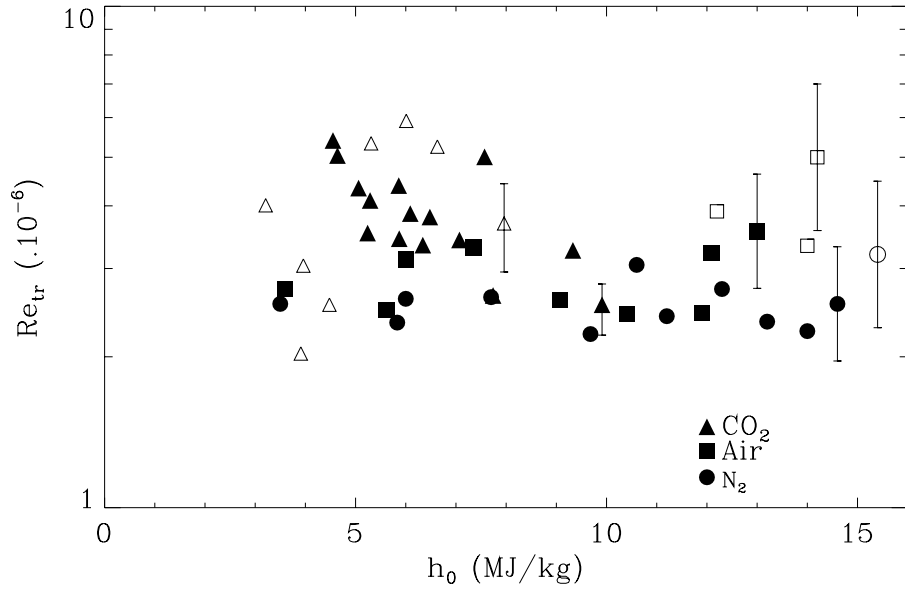


Figure 4.3: Plot of transition Reynolds number versus stagnation enthalpy. Open symbols indicate flows that were almost fully laminar with a hint of transition. Error bars are representative indications of the uncertainty. No clear relationship appears to exist between Re_{tr} and h_o . (Reproduced from Adam [1])

confirmed by Adam [2], is that the correct scaling to observe the effects of enthalpy is obtained when the transition Reynolds number is evaluated at the reference temperature as defined in Section 3.5.1. The resulting equation for the reference transition Reynolds number is

$$Re_{tr}^* = \frac{\rho^* U_e x_{tr}}{\mu^*}, \quad (4.2)$$

where the * quantities are evaluated at the reference temperature assuming constant pressure and frozen composition within the boundary layer. Assuming an ideal gas, the reference density is calculated as

$$\rho^* = \rho_e \frac{T_e}{T^*}. \quad (4.3)$$

Figure 4.3 obtained from Adam [1] shows a plot of Re_{tr} versus h_o and it shows that there is no discernable relationship between Re_{tr} and h_o . It should be noted that the carbon dioxide shots were limited to lower enthalpies since the Reynolds number attainable in T5 at higher enthalpies was too low to observe transition on the cone. Figure 4.4 is a plot of Re_{tr}^* versus h_o which shows that the reference temperature concept brings out a very clear trend with the enthalpy having a strong stabilizing effect on the boundary layer (thereby

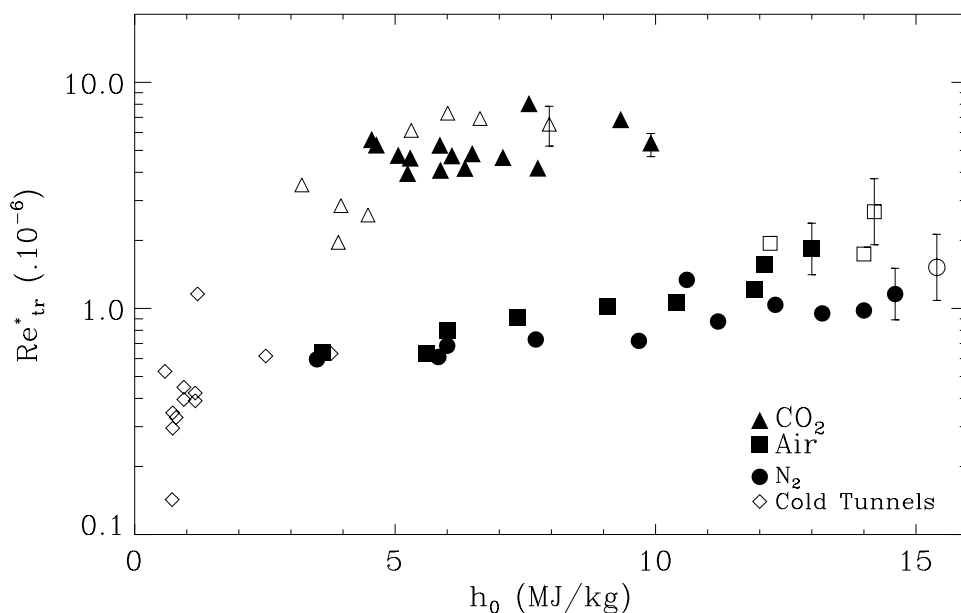


Figure 4.4: Plot of reference transition Reynolds number versus stagnation enthalpy. Open symbols indicate flows that were almost fully laminar with a hint of transition. Error bars are representative indications of the uncertainty. A clear stabilization effect with increasing enthalpy is observed, with the effect being most pronounced in carbon dioxide which has the smallest dissociation energy. (Reproduced from Adam [1])

delaying transition). Furthermore, different gases were found to be stabilized by different amounts (*i.e.*, they had different slopes). For example, the carbon dioxide measurements fell on a steeper line and were more strongly stabilized than the air or nitrogen measurements. This trend correlated with the dissociation energies of the respective gases. Of the three gases, nitrogen had the highest dissociation energy at 33.7 MJ/kg and exhibited the least amount of stabilization with increasing enthalpy (*i.e.*, had the shallowest slope). Air, which includes a strong oxygen component with a dissociation energy of 15.6 MJ/kg, had a slightly larger slope exhibiting a slightly stronger stabilizing effect. Finally, carbon dioxide, which dissociates readily into CO and O with a dissociation energy of about 12.0 MJ/kg, had the steepest slope and exhibited strong stabilization at lower enthalpies. Recall that the dominant instability leading to transition at the T5 conditions is the acoustic Mack mode. This stabilization effect is, therefore, attributed to the increased chemistry in the flow since acoustic waves have been shown to be attenuated by chemical activity [18].

4.4 Effectiveness of the Porous Surface

The previous experiments indicated that there is a strong relationship between reference transition Reynolds number and stagnation enthalpy. This was of particular interest since this trend was attributed to chemical damping of the Mack mode which was the mode the porous surface was seeking to control. There was further evidence to believe that the effectiveness of the porous surface would scale in a similar manner since calculations by Johnson *et al.* [51] in air indicated that the most unstable mode frequencies varied with stagnation enthalpy. For these reasons, the current tests were performed over a range of enthalpies. Before extending the results to the porous surface, however, it was necessary to validate the present results of the smooth surface with similar experiments performed by previous researchers. Three representative cases at high, mid, and low enthalpies are described below, with detailed comparisons to previous experiments by Germain [38]. This is followed by summary data plots for the nitrogen and carbon dioxide shots in order to perform general comparisons with previous results obtained by Germain [38] and Adam [2], and to elucidate any observable trends with stagnation enthalpy.

4.4.1 Case I: Both Sides Laminar

Figure 4.5 shows plots of St versus Re_x obtained from shot 1960, a high enthalpy shot ($h_o = 12.8$ MJ/kg) in nitrogen. The plots show that the boundary layer was laminar over the entire length of the cone for both the smooth and porous surfaces. Furthermore, the results obtained on the smooth surface are shown to be in excellent agreement with previous results obtained by Germain for essentially the same run condition. Note that Germain's data indicates that the boundary layer is just beginning to transition towards the back of the model, while this effect is not evident in the present experiment. This is attributed to the slight differences in the freestream conditions between Germain's and the present experiments.

4.4.2 Case II: Both Sides Transitional

Figure 4.6 shows plots of St versus Re_x for shot 1963, which was a mid-enthalpy shot ($h_o = 7.2$ MJ/kg) in nitrogen. These plots show typical transition behaviour with the data following the theoretical laminar curve at low Reynolds number and moving to the expected

turbulent curve further downstream. A comparison of the two plots shows that the boundary layer on the smooth surface transitions before the porous surface boundary layer. This appears to validate the prediction by Fedorov and Malmuth. Once again, Germain's data for a similar run condition is shown for comparison with excellent agreement as to the transition location.

4.4.3 Case III: Porous Surface Laminar, Smooth Surface Transitional

Figure 4.7 shows plots of St versus Re_x obtained from shot 1976, a low-enthalpy shot ($h_o = 5.0$ MJ/kg) in nitrogen. In this particular case, the smooth surface boundary layer transitions roughly at the half way point on the cone while the porous sheet boundary layer is laminar all the way to the end of the cone. This shot clearly demonstrates the dramatic effect of the porous surface in delaying boundary layer transition. Once again, notice the good agreement with the previous experiment performed by Germain.

4.4.4 Laminar Heat Flux

Figures 4.5 to 4.7 suggest interesting trends with respect to the laminar heat flux levels. Note, for a given shot, the theoretical laminar line plotted on both the smooth and porous surface plots is the same line and can be used as a visual reference to qualitatively compare the relative magnitudes of the heat flux levels on both surfaces.

On the smooth surface, the experimentally fitted laminar line was typically close to the theoretical laminar line and, although not shown in the present figures, it tended to be above the theoretical line at higher enthalpies. This trend was also observed in the experiments by the previous researchers and was found to be more pronounced in gases which had lower dissociation energies, such as carbon dioxide. For these reasons, it is attributed to an increase in the local heat flux level due to non-equilibrium chemistry, specifically the exothermic recombination reactions that occur at the wall.

In the present experiments, the laminar heat flux level on the porous surface tended to be lower than on the smooth surface. This would be possible if the porous surface thickened the boundary layer relative to the smooth surface. Approximate measurements of the boundary layer thickness from a shadowgraph image (see Section 4.5), however, show no measurable difference between the thicknesses on the two surfaces. Another possible explanation is that the porous surface somehow modifies the effective catalyticity of the

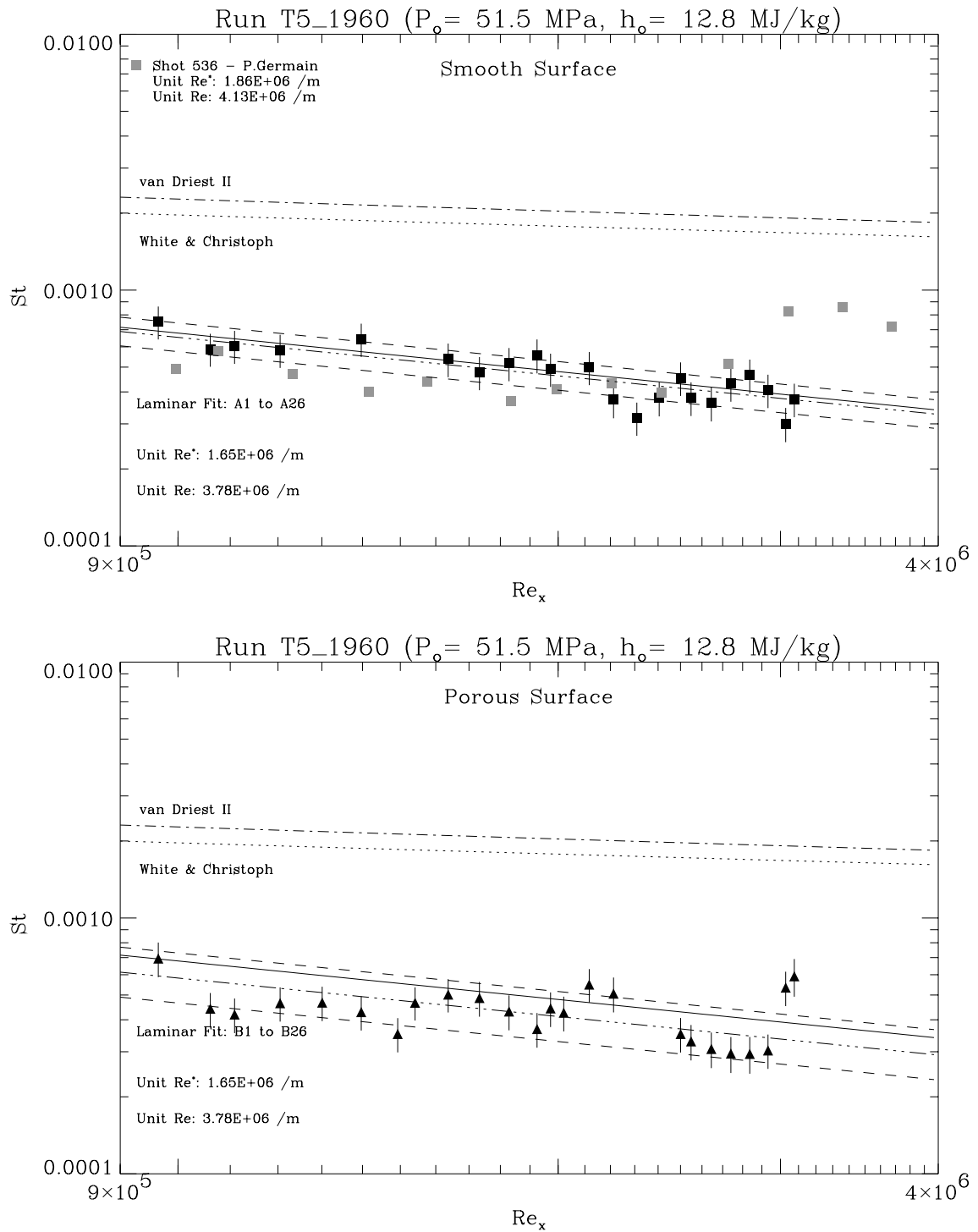


Figure 4.5: St versus Re_x plots obtained for shot 1960 ($P_o = 51.5$ MPa, $h_o = 12.8$ MJ/kg) in nitrogen test gas. The top and bottom plots show the data (obtained from the same shot) for the smooth and porous surfaces, respectively. The dark black symbols correspond to the present experiment and the grey symbols correspond to a previous experiment by Germain for essentially the same run condition. Note that both the smooth and porous surface boundary layers are laminar.

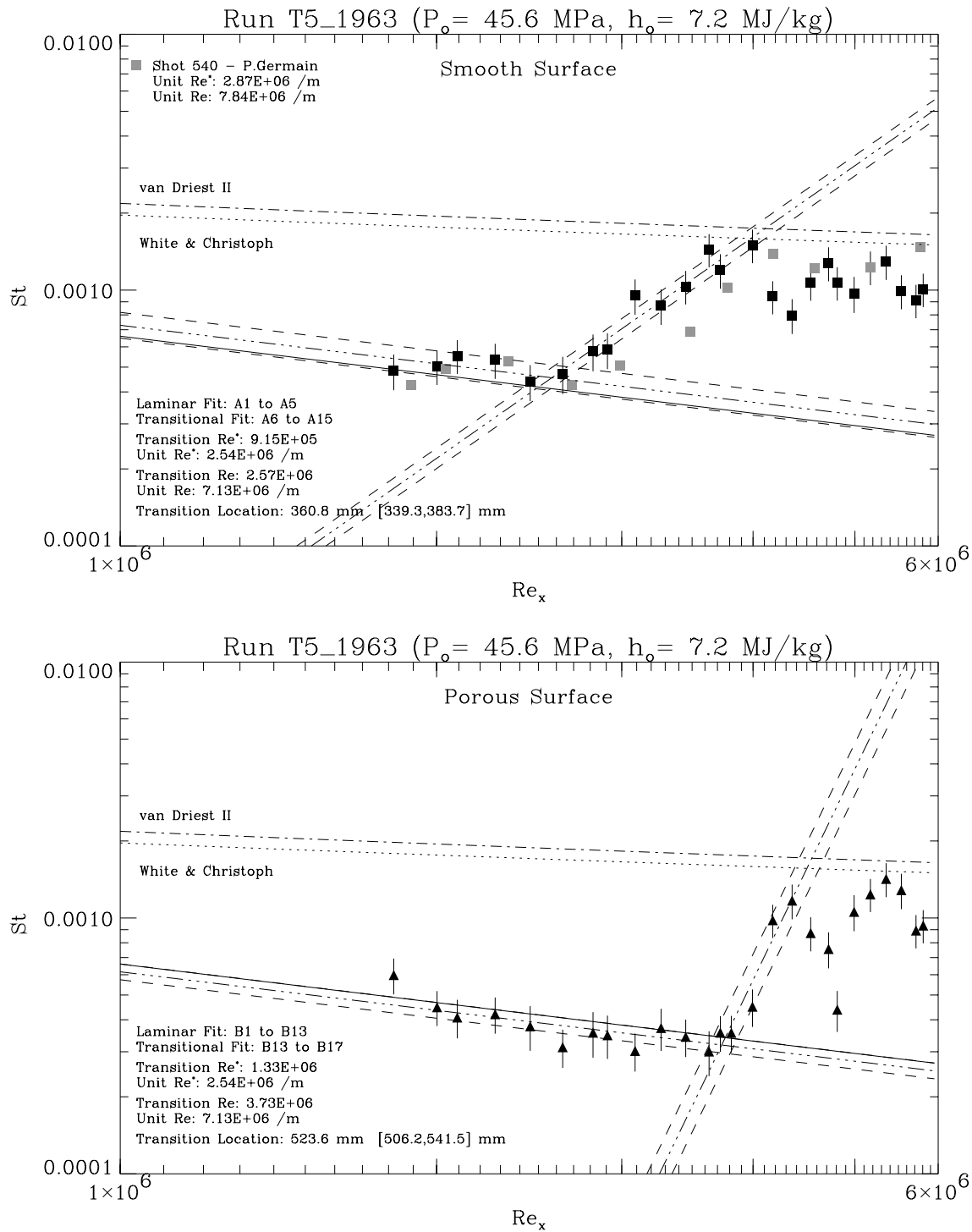


Figure 4.6: St versus Re_x plots obtained for shot 1963 ($P_o = 45.6$ MPa, $h_o = 7.2$ MJ/kg) in nitrogen test gas. The top and bottom plots show the data (obtained from the same shot) for the smooth and porous surfaces, respectively. The dark black symbols correspond to the present experiment and the grey symbols correspond to a previous experiment by Germain for essentially the same run condition. Note that both the smooth and porous surface boundary layers are transitional.

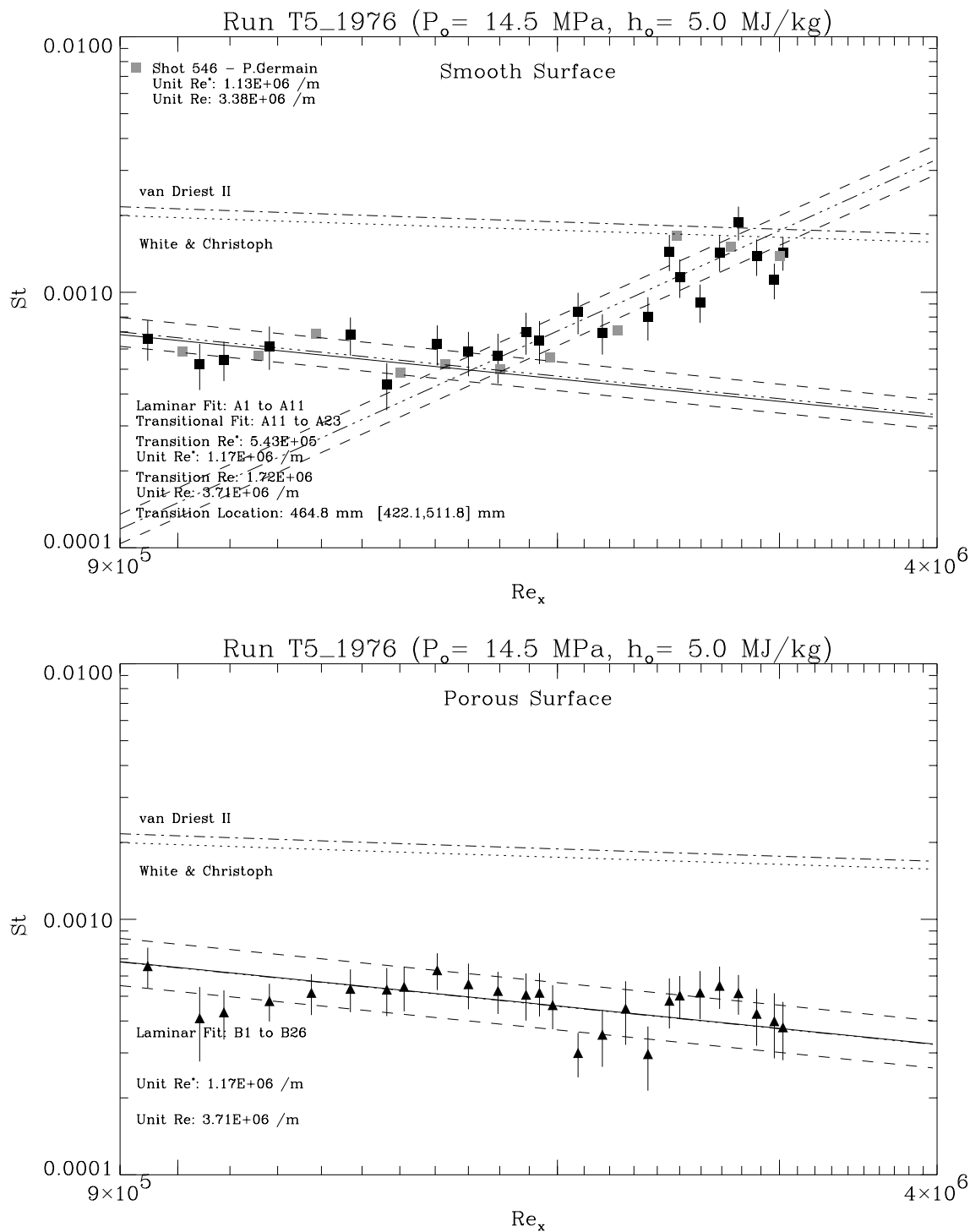


Figure 4.7: St versus Re_x plots obtained for shot 1976 ($P_o = 14.5$ MPa, $h_o = 5.0$ MJ/kg) in nitrogen test gas. The top and bottom plots show the data (obtained from the same shot) for the smooth and porous surfaces, respectively. The dark black symbols correspond to the present experiment and the grey symbols correspond to a previous experiment by Germain for essentially the same run condition. Note that the smooth surface boundary layer transitions to turbulent boundary layer, but the porous surface remains laminar.

wall and suppresses the wall recombination reactions. In addition, it was observed that the laminar heat flux level tended to be lower than the theoretical estimate. This trend is even more puzzling since the theoretical laminar line should represent the lower bound on the heat flux level as discussed in Section 3.5.1.1. It should be added that it is difficult to say with absolute certainty that the observed differences are real since the theoretical line falls within the uncertainty bounds of the experimental fit.

4.4.5 Summary Data

4.4.5.1 Nitrogen Shots

Figure 4.8 gives a summary of the data for the nitrogen shots. The first observation is that the present experimental results agree fairly well with the previous results obtained by Germain. The second observation is that, in all cases, the porous surface delayed transition by a significant amount. The open diamonds with an upwards facing arrow (\uparrow) indicate that the porous surface boundary layer was laminar to the very end of the cone. The value plotted assumes that transition occurred at the last thermocouple (*i.e.*, unit Reynolds number multiplied by the last thermocouple location). This is not a valid data point, but rather a manner in which to show that the boundary layer was entirely laminar. The same discussion applies for the open square symbols with a (\uparrow) for the smooth surface side. The two data points at 13 MJ/kg are actually open diamonds superimposed on open squares with an \uparrow , indicating that both the smooth and porous surface boundary layers were entirely laminar. It is interesting to note that the porous sheet appears to be less effective at mid-enthalpies as compared to low and high enthalpies.

4.4.5.2 Carbon Dioxide Shots

An analysis similar to that performed for the nitrogen shots was also performed for each carbon dioxide shot. The resulting summary plot of Re_{tr}^* versus h_o is shown in Figure 4.9. Once again there is fairly good agreement between the present smooth surface results and those obtained in previous experiments by Adam, although there is much more scatter. This plot shows that the porous sheet was, in fact, detrimental at higher enthalpies, but was effective at lower enthalpies with a cross-over point at roughly 3.0 MJ/kg. The reason for this will be addressed in Section 4.4.7.

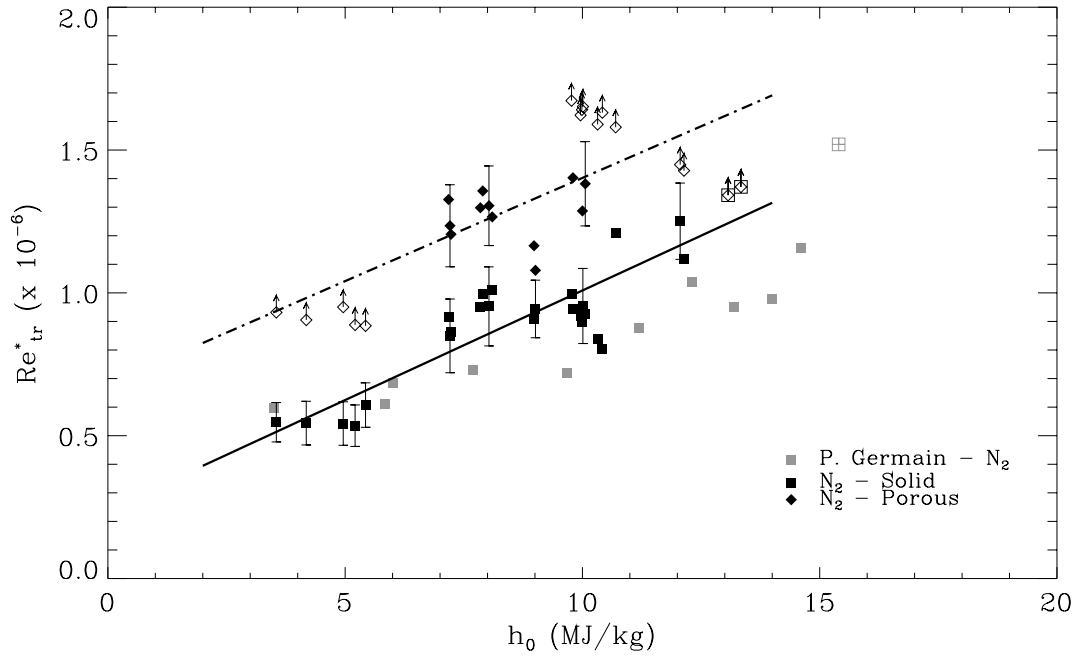


Figure 4.8: Plot of Re_{tr}^* versus h_o showing a summary of the nitrogen data. The dark data points are for the present experiments. The diamonds represent the Re_{tr}^* on the porous surface, while the squares represent the Re_{tr}^* on the smooth surface for the same shot. The grey squares represent the data obtained in previous experiments for a smooth surface at similar run conditions by Germain. The open symbols with upward facing arrows are used to indicate cases where the boundary layer was laminar over the entire length of the cone (they mark the last thermocouple location as being the transition location). The lines are linear curve fits to help guide the eye (dashed-dotted for porous, solid for smooth).

4.4.6 Elimination of Other Causes for the Observed Effectiveness of the Porous Surface

As mentioned previously, the main objective of these experiments was to broadly test the computational prediction of Fedorov and Malmuth [32] by comparing the transition Reynolds number on the smooth surface versus the porous surface for each shot. The previous sections partially validated the present results since transition on the smooth surface successfully reproduced the previous experiments by Germain [38] and Adam [2]. In order to completely confirm the effectiveness of the porous surface, however, it is necessary to eliminate other spurious effects. In particular, one must check the repeatability of the experiments, as well as verify that non-axisymmetry and angle-of-attack issues were not affecting the results.

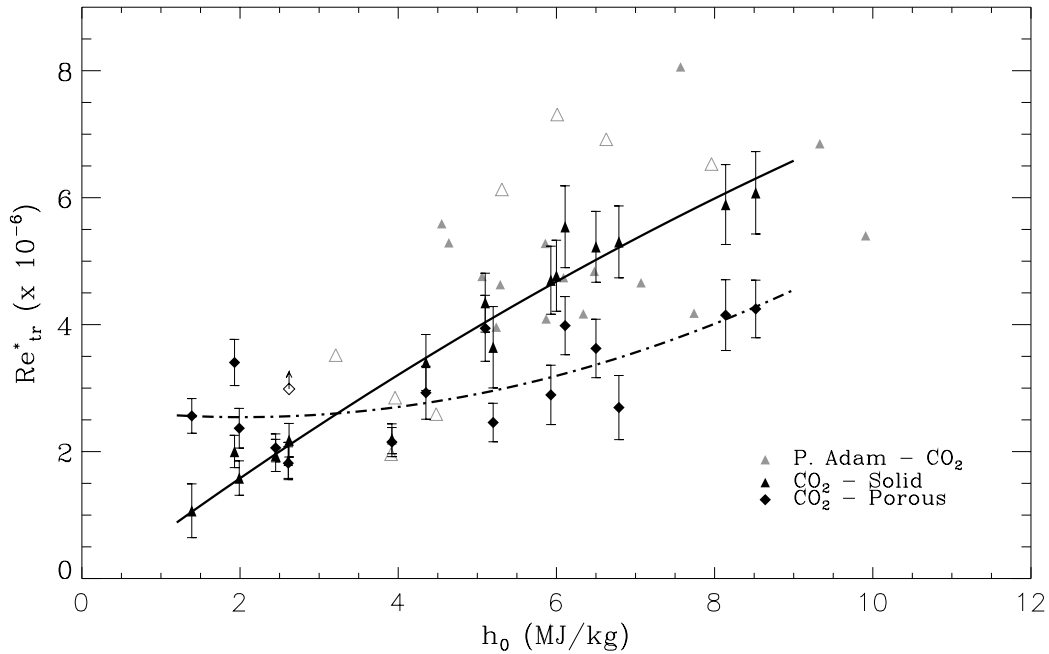


Figure 4.9: Plot of Re_{tr}^* versus h_o showing a summary of the carbon dioxide data. The dark data points are for the present experiments. The diamonds represent the Re_{tr}^* on the porous surface, while the triangles represent the Re_{tr}^* on the smooth surface for the same shot. The grey triangles represent the data obtained in previous experiments for a smooth surface at similar run conditions by Adam. The lines are 2^{nd} order curve fits to help guide the eye (dashed-dotted for porous, solid for smooth).

4.4.6.1 Repeatability

Repeatability was tested by repeating selected experimental run conditions at various stages in the test program and noting that there was no observable effect on transition location. This was of particular importance since it confirmed that the accumulation of soot on the surface of the model had no effect on the experimental results. This observation is also an indication of the robustness of this boundary layer control scheme to small amounts of contamination.

4.4.6.2 Angle-of-attack

The effects of angle-of-attack on transition Reynolds number in hypersonic flow over a cone have been studied extensively. Previous experiments indicated that transition Reynolds number was a strong function of angle-of-attack near 0° . Stetson [110] performed experiments at Mach 6 on a 8° half-angle cone and compared his results with other researchers

including DiCristina (8° cone, M=10) [27], Holden (6° cone, M=13.3) [45], and Krogmann (5° cone, M=5) [62]. This last set of experiments by Krogmann most closely resembled the present experimental test conditions and, incidentally, demonstrated the most sensitivity of transition Reynolds number with angle-of-attack. In fact, an interpolation from his results revealed that transition Reynolds number varied by as much as 5% if the angle-of-attack varied by as little as 0.1°. For the present experiments, angle-of-attack was eliminated as a cause for the delayed transition by carefully aligning the model to within $\pm 0.05^\circ$ of the tunnel axis. Furthermore, it was noted that the observed effect was to delay transition anywhere from 15% to 100% (or more since the cone was not long enough). This is significantly larger than the 5% variation attributable to angle-of-attack alone.

4.4.6.3 Axisymmetry

Non-axisymmetry issues were addressed by rotating the model to the 0°, 90° and 180° orientations and repeating the experiments. In particular, two run conditions were repeated and can be seen in Figure 4.8 as the three data points clustered at 5 MJ/kg and 8 MJ/kg, respectively. Clearly, there is excellent agreement and there appears to be no observable effects from lack of axial symmetry.

4.4.7 Effects of Surface Roughness

As mentioned previously, for the nitrogen experiments, the porous surface was effective over the whole enthalpy range tested; though it was more effective at low and high enthalpy conditions than at mid-enthalpy conditions. For the carbon dioxide shots, however, the porous surface was only effective at very low enthalpy conditions and was counter-productive at mid to high enthalpies. This interesting behaviour suggested that another parameter was important in the carbon dioxide flows.

An explanation for the observed behaviour lies in the expectation that the porous surface must be hydraulically smooth (*i.e.*, hole size must be sufficiently small in relation to the viscous length scale) in order for the proposed mechanism to effectively delay transition. If this were not the case, then the holes would act as distributed surface roughness and prematurely trip the boundary layer. A plot of $Re_{tr,porous}^* - Re_{tr,smooth}^*$ versus Re_D^* (Reynolds number based on hole diameter) clearly shows that the delay in transition becomes much smaller as Re_D^* increases (see Figure 4.10). It should be noted that no such trend was

observed when the results were plotted using the Reynolds number evaluated at the edge conditions (Re_D) and it is, therefore, concluded that the reference Reynolds number is the proper Reynolds number to use in this analysis for these flows. The graph also shows that the mechanism becomes less effective at an Re_D^* of about 130 and actually prematurely trips the boundary layer at an Re_D^* greater than 300. For comparison, the Reynolds number evaluated at the viscous length scale was estimated at $Re^+ \simeq 800$. The most relevant experiment (to the present case) regarding distributed surface roughness effects was performed by Germain (see Section 4.4.7.1), who found that 0.1 mm salt crystals ($Re_k^* = 220$) randomly distributed over the first 206 mm of the model tripped the boundary layer. No attempt was made to identify the ‘critical’ roughness Reynolds number below which the surface roughness had no effect on transition. For such a comparison, it is useful to recognize that the present results correspond reasonably well with experiments in incompressible flow by Feindt (as reported by Schlichting [104]) who examined the effect of distributed surface roughness (in the form of sand grains) on transition Reynolds number. Although the type of roughness was different from the current experiments (sand grains versus porous surface), Feindt also found that the surface roughness became important when Re_h (based on the sand grain height) was greater than 120. Similarly, Pfenninger [85] reported that surface roughness issues became important in laminar flow control experiments (suction through slots) when Re_s (based on slot width) was approximately greater than 100.

More recently, Reda [91] reviewed the effects of distributed surface roughness in hypersonic flows on nosetips, attachment lines and lifting entry vehicles. Reda concluded that there exists no universal value for critical Re_k (based on roughness height) for transition to turbulence and that this critical roughness Reynolds number was highly dependent on the particular flow field and roughness characteristics. Despite this observation, a number of different experiments indicate that the critical roughness Reynolds number is approximately 100 to 200. Reda’s experiments [90] on nose tip transition in a ballistic range yielded values for the critical Re_k of 192. In other experiments, Bertin *et al.* [8] found $Re_k = 110$ was the critical value at which roughness effects began to dominate in wind tunnel tests of a 0.0175 scale model of the Space Shuttle Orbiter at Mach 8 to 12. Furthermore, analysis by Goodrich *et al.* [41] (as reported by Reda [91]) of transition data on the windward centreline of the Space Shuttle Orbiter during reentry for missions STS-1 to STS-5 suggest a critical Re_k of 120. It should be noted that in the above cases, the Re_k values were for surface

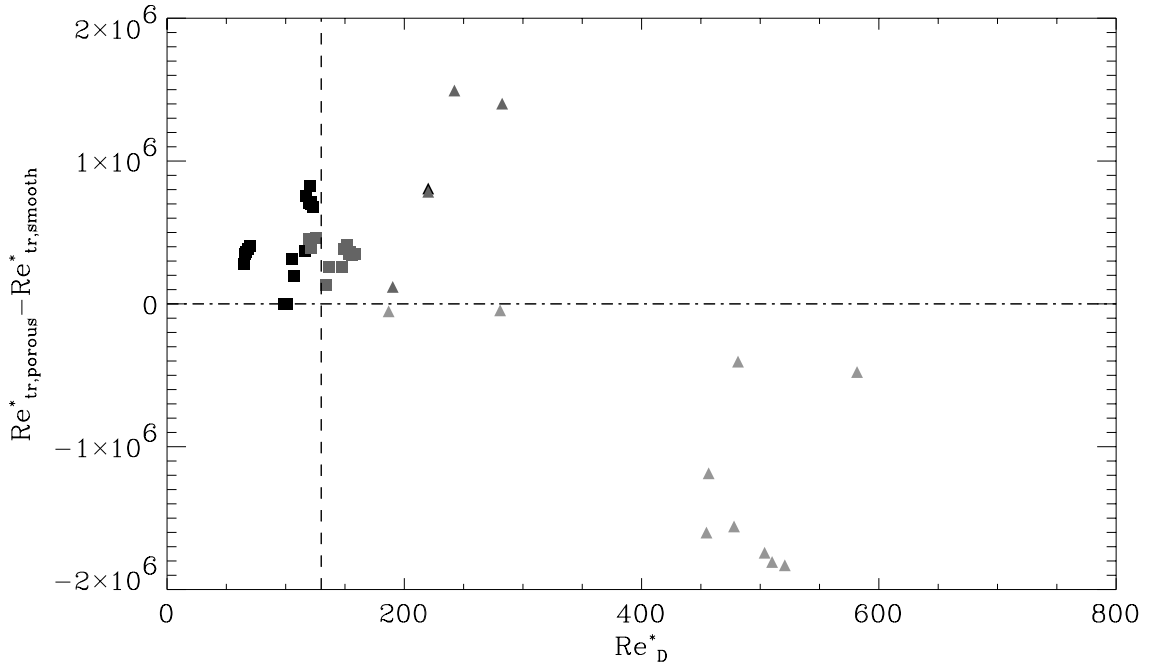


Figure 4.10: Plot showing the decreased effectiveness as Re_D^* increases beyond 130 (vertical line). The greyscale indicates the qualitative effectiveness of the porous surface. Black indicates laminar over the entire length of the cone on the porous side, medium grey indicates delayed transition was observed on the cone and light grey indicates premature transition. Squares and triangles correspond to N_2 and CO_2 , respectively.

bumps (as opposed to holes in the present work) and were calculated using the conditions in the boundary layer at the roughness height. This may or may not allow direct comparison with the Re_D^* used to analyse the present results, but it is clear that the critical Re_D^* is in the same range as previous experiments.

Finally, it should be noted that closer examination of Figure 4.10 also indicates that some parameter is still not fully accounted for since the effectiveness of the porous sheet does not decrease monotonically with increasing Re_D^* . Specifically, the porous sheet appeared to be more effective in the carbon dioxide shots at $Re_D \simeq 200$ than the nitrogen shots at $Re_D \simeq 130$. It is not surprising that nitrogen and carbon dioxide behave slightly differently because the different chemistry involved affects the second mode amplification. In fact, this difference is probably the effect of enthalpy that had been noted earlier.

4.4.7.1 Previous Surface Roughness Experiments in T5

Germain [37] previously performed extensive tests examining the effects of roughness near the cone tip region on the transition location. These tests were performed at Mach 5.5 in nitrogen test gas at nominal $P_o = 60$ MPa and $h_o = 10$ MJ/kg. The typical unit Reynolds number was 5.5×10^6 1/m and the unit reference Reynolds number was 2.2×10^6 1/m. These conditions correspond approximately to shots 1965, 1966 and 1973 from the present experiments. The first test examined three-dimensional randomly distributed surface roughness in the form of salt crystals (which Germain measured to be 0.1 mm in height) covering the first 203 mm of the cone. This distributed roughness was found to trip the boundary layer; an observation that is not surprising based on the discussion in the previous section since the computed Re_k^* value for this case was 220.

The second series of experiments examined the effects of circumferentially distributed three-dimensional elements at two axial locations. This was performed by clamping small bits of 0.125 mm diameter copper wire between the removable cone tip pieces on Germain's model at the 76 mm and 203 mm locations (measured from the cone tip along the cone axis). The pieces of wire were placed circumferentially at approximately 3 to 4 mm intervals (measured along the circumference) and formed small 'spikes' or protuberances into the flow. Although not reported by Germain, it is estimated from the above information that there were approximately 10 spikes (*i.e.*, approximately every 36°) at the 76 mm location and 30 spikes (*i.e.*, approximately every 12°) at the 203 mm location. Germain varied the height of the spikes and found that a spike height of 0.1 mm did not affect the transition location, whereas a spike height of 0.25 mm caused premature transition.

Germain did a further test using a single three-dimensional roughness element that was clamped at the downstream cone junction (at the 203 mm location). This roughness element was a 0.1 mm thick shim that was 1 mm wide and 1 mm high (*i.e.*, approximately the same height as the boundary layer thickness) and was placed along the 90 degree ray. This large single three-dimensional roughness element did not trip the boundary layer and there was no observable effect on the transition location (with respect to the smooth wall case). It should be noted that this experiment was performed at the same nominal conditions as above; however, the unit reference Reynold's number achieved was slightly lower at 1.7×10^6 1/m.

These above tests performed by Germain highlight the fact that the hypervelocity boundary layer is extremely insensitive to surface roughness. Furthermore, there is a clear trend that randomly distributed surface roughness is the most effective way to trip the boundary layer, followed by circumferentially distributed surface roughness. Finally, the boundary layer appears to be extremely insensitive to even large scale isolated three-dimensional disturbances.

4.5 Resonantly Enhanced Shadowgraph

Further evidence of the effectiveness of the porous sheet is seen in Figure 4.11, which is a resonantly enhanced shadowgraph showing the boundary layer transitioning on the smooth surface while remaining laminar on the porous surface. This shadowgraph is from shot 2008 ($P_o = 48.2$ MPa, $h_o = 9.8$ MJ/kg) and was obtained by seeding the flow with sodium and tuning the frequency of the dye laser light source to the sodium D-line as described in Section 3.2.4. The transition location on the smooth surface identified by the analysis of the heat transfer data is approximately at the left edge of the magnified image of the smooth surface. These magnified images were also used to measure the laminar boundary layer thickness at the $x = 495$ mm location. This boundary layer thickness was independently measured on both the smooth and porous surface, and both were found to be approximately 1.2 ± 0.15 mm which is in agreement with Adam's computations [1]. It should be noted that these measurements are only approximate due to difficulties in accurately identifying the edge of the cone in the images and due to distortions from the optical integration across the test section and through the shear layer of the free-jet from the nozzle.

4.6 Limitations of the Experiments

4.6.1 Comparison with Linear Stability

The single most important limitation of the present experimental work is the lack of detailed information available with regards to the transition process. Because of the extremely harsh conditions in the freestream, it is simply not presently possible to perform a detailed stability experiment in a hypervelocity shock tunnel. Delicate instrumentation

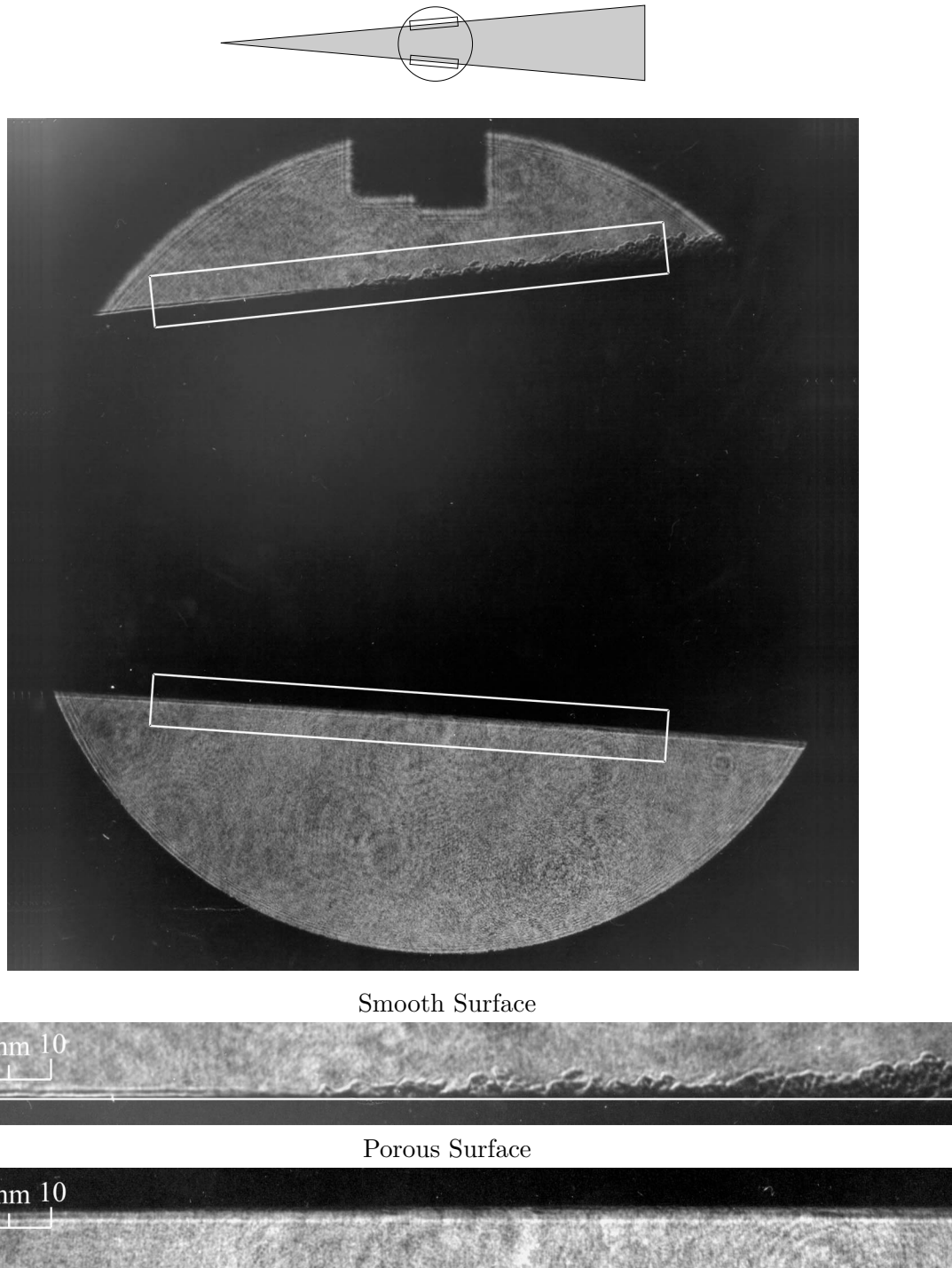


Figure 4.11: Resonantly enhanced shadowgraph for shot 2008 ($P_o=48.2$ MPa, $h_o=9.8$ MJ/kg) showing the boundary layer transitioning on the smooth surface (top) while remaining laminar on the porous surface (bottom). Flow is left to right and the schematic at the top indicates the window position relative to the model. The rectangular boxes in the main image indicate the location of the magnified images whose left and right edges are 495 mm and 615 mm from the cone tip, respectively (as measured along the surface of the cone). The white line on the magnified image of the smooth surface was digitally added to indicate the approximate surface of the model.

such as hot-wire probes traditionally used to measure boundary layer profiles and the tiny fluctuations of the instability waves would be destroyed during the experiment. Attempts were made by Adam [1] to obtain the frequency of the instability waves from thermocouple data traces recorded using a high frequency oscilloscope, but these efforts were unsuccessful.

From the computational point of view, the linear stability analysis performed by Fedorov and Malmuth assumed a perfect gas. As shown by the previous work by Stuckert and Reed [93], Bertolotti [9], Hudson *et al.* [50] and Johnson *et al.* [51], it is clear that real gas effects have a strong bearing on the results of linear stability analysis at these conditions. In fact, preliminary calculations by Fedorov using ‘effective ratios of specific heat’ to represent the T5 conditions showed that the length of the laminar run on the porous surface extended several model lengths. Obviously, in these cases, comparisons simply can not be made with experiment.

4.6.2 Lack of Noise Spectrum Information

An issue related to the limitation discussed in the previous section is the lack of knowledge of the noise spectrum generated by the tunnel. The frequency spectrum of the noise radiated by the nozzle wall boundary layer in T5 is unknown. If noise measurements were available, however, they might add to the evidence that the most unstable mode is indeed the high frequency Mack mode. So far, this statement is made based on the linear stability calculations by Johnson *et al.* [51] and their strong agreement with the experimentally observed trends in transition delay as a function of increasing enthalpy. To some extent, one could even argue that the current set of experiments is further evidence of the dominance of the second mode. For now, one can make an educated guess as to an upper bound of the frequencies of the noise generated. It is known that the source of the noise is the nozzle wall boundary layer which is approximately 10 mm thick. Assuming that the turbulent structures responsible for aerodynamic noise generation are an order of magnitude smaller (*i.e.*, 1 mm), taking a freestream velocity of 5 km/s, and noting that $f = U_\infty/\delta_{\text{Nozzle}}$, then the tunnel probably generates noise at a frequency of about 5 MHz, although the magnitude of this noise is unknown. As recently reviewed by Schneider [105], the tunnel noise level is known to have a strong effect on the transition Reynolds number. Schneider [105] reports that freestream turbulence levels measured in shock tunnels at lower frequencies (hundreds of kilohertz) are typically of the order of 1% to 3%. Stetson [111]

proposed that shock tunnels might be relatively quiet at the high second mode frequencies that are of interest, but this conjecture has yet to be tested.

4.6.3 Model and Flow Imperfections

Obviously, great care was taken to minimize imperfections during the construction of the model. In the worst case scenarios, efforts were taken to make sure the imperfections were symmetric to affect both the smooth and porous surfaces equally. This being said, Section 3.3 discussed some of the imperfections that arose during the manufacturing process. These were reasonably demonstrated to be inconsequential; however, it is possible that they were not. In particular, the imperfection of most concern was the small gap that existed towards to the front of the model between the cone sheet and the base cone. There is also the question of the welded seams whose effect on the boundary layer is entirely unknown. Even if the welds had no effect on the flow, one wonders about the structure of the boundary layer in the region near the interface between the smooth and porous surfaces. This question is particularly interesting in the case where the boundary layer transitioned mid-way along the length of the cone on the smooth surface, yet remained completely laminar to the end of the cone just 180° away on the porous surface.

Another issue that has not been addressed so far is the issue of freestream flow quality. Significant effort was spent early on by Rousset [98] to characterize the flow uniformity across the nozzle plane and it was found to be excellent. It should be noted, however, that the contour nozzle used for the present experiments is designed for high pressure ($P_o = 60$ MPa), high enthalpy ($h_o = 25$ MJ/kg) shots. The current series of experiments were operated at much lower pressures and enthalpies in order to attain high enough Reynolds number to observe transition on the cone. As such, the nozzle was sometimes operated at grossly off-design conditions. This issue was a problem in the helium experiments previously performed by Germain. In that case, the expansion fan from the nozzle lip impinged mid-way along the length of the cone, immediately causing transition and invalidating the results of the experiment. Neither Germain nor Adam found evidence of this phenomena in the nitrogen, air or carbon dioxide tests and no evidence of this was found in the present work. Furthermore, great effort was spent to insure that the model was lined up with the centre axis of the nozzle so that any flow non-uniformities, which presumably would be axisymmetric, would affect both the smooth and porous surface equally.

4.7 Summary

Keeping in mind the above limitations, based on the compilation of all the previous experimental and computational results, in addition to the results obtained from this study, the following statements can be made with reasonable certainty:

1. The boundary layer transition process in the T5 experiments by Germain, Adam and in the present work is dominated by the high frequency, acoustic Mack mode.
2. Real gas effects have a strong damping effect on the Mack mode and are subsequently responsible for the delay in transition observed with increased enthalpy.
3. Acoustic absorption by the porous surface is highly effective in damping the Mack mode and ultimately delaying transition.

As with all experiments, there are still many unknowns and unanswered questions. Attempts have been made to address all of the concerns, and within this context, the present series of experiments have conclusively shown the effectiveness of the proposed passive boundary layer control scheme.

Chapter 5 Conclusions

Extensive experiments testing a novel passive hypervelocity boundary layer transition control scheme have been carried out in the T5 Hypervelocity Shock Tunnel on a sharp 5.06° half-angle round cone with a smooth surface over half the cone and an ultrasonically absorptive porous surface over the other half. This boundary layer scheme was based on the results of a linear stability analysis whose details have been presented. In addition, the detailed flow physics responsible for the acoustic damping mechanism were examined. The experiments, performed in nitrogen and carbon dioxide, used heat transfer measurements to simultaneously determine the transition location on the smooth and porous surfaces for each shot. These new measurements for the smooth surface transition location compared very well with experimental results obtained by previous researchers in the same facility. The theoretical result that transition may be delayed by suitable wall porosity has been confirmed convincingly in nitrogen flows and the reversal of the phenomenon in carbon dioxide flows appears to be due to the chosen wall porosity scale being too coarse relative to the viscous length scale for high enthalpy run conditions. The results were tested for repeatability and were checked to insure that they were not induced by angle-of-attack or other effects. Finally, the effectiveness of the porous sheet was further evidenced by a resonantly enhanced shadowgraph that clearly showed transition occurring over the smooth surface but not on the porous surface.

5.1 Recommendations for Future Work

The present work represents an exploratory proof-of-concept study of a new idea to passively control a hypervelocity boundary layer. As such, this work should be viewed as laying the foundation for more detailed studies, experimental and computational, to better understand the mechanisms involved. Some suggestions are provided here in order to guide future efforts.

5.1.1 Experimental

Stability Experiments: Ideally, a detailed stability experiment should be performed. For now, this capability in hypervelocity flow does not exist; however, progress is being made in this area. Recent work by Salyer *et al.* [100] has successfully demonstrated the use of laser differential interferometry to perform receptivity experiments in quiet supersonic flow. The system is able to measure extremely small changes in density with a spatial resolution of 0.1 mm at a frequency of 400 kHz, although apparently higher frequencies are attainable. The main drawback of this technique is that, like most optical techniques, it performs line-of-sight integration across the test section. It will, therefore, not be able to resolve the instability waves on a cone, but there is some potential for use on a flat-plate. Even in this case, however, there is still the issue that this technique will also be measuring the density fluctuations across the shear layer of the free-jet from the nozzle.

In the mean time, it is possible to perform stability experiments in hypersonic tunnels as has been done in the past. An advantage is that the thicker boundary layers typical of these experiments will make it easier to manufacture the porous surface since the wavelength of the second mode will be much larger. In fact, parametric studies can then be performed examining the effect of differently sized and spaced holes. Such efforts, of course, must be guided by suitable computations. It would also be interesting to perform such experiments on a flat-plate to see if there are any differences. In principle, one would not expect significant changes in behaviour. Previous experiments, however, have documented the fact that transition Reynolds numbers on flat-plates tend to be lower than those on cones.

Freestream Noise Measurements: This recommendation is the same as the one put forth by Adam [1] for the very same reasons. To date, there is no direct knowledge of the freestream noise levels in T5. These measurements are now, in principle, possible using the laser differential interferometry technique described earlier. The issue of line-of-sight integration is still relevant, although at worst this technique will still be able to provide order of magnitude estimates for the freestream noise levels. One minor disadvantage is that such a system is not necessarily easy to set up.

Acoustic Properties Characterization: Attempts were made to characterize the acoustic properties of the porous surface used in the current experiments. This effort, however,

was severely limited and the results could only be interpreted in a qualitative sense. Ideally, a setup should be constructed to perform these static benchmark tests at the low density and pressure typical of hypersonic conditions. For the present experiments in hypervelocity flow, the frequencies were of the order of megahertz. Performing air-coupled acoustic tests at such high frequencies is not possible since the current limit in air-coupled transducers appears to be 400 kHz. This limit, however, is within the range of the Mack mode frequencies seen in standard hypersonic stability experiments and such benchmark tests would be relevant. Ideally, a correlation between static benchmark tests and the estimated acoustic absorption during the experiment would be determined.

Alternate Materials: As identified in Appendix C, there is at least one other candidate material for use as an acoustically absorbing surface. Such materials are much easier to manufacture and are, therefore, strong candidates for future investigation. Once again, any such efforts must be guided by linear stability calculations. The acoustic characterization of these materials in static benchmark tests takes on an even more important role in this case since there will be very little theoretical guidance for developing the required boundary conditions.

Three-Dimensional Effects: Ultimately, if such a boundary layer control scheme is ever intended to be used on a flight vehicle, strong consideration must be given to three-dimensional effects. It is likely that near the leading edge of any realistic vehicle these will be important and the Mack mode may not be the dominant mode. In such cases, the use of an acoustically absorptive surface might not be effective, and in fact, might destabilize the boundary layer even further. Experiments to examine such concepts are very far in the future since the issue of cross-flow instability in hypersonic flow is only starting to be addressed and there is still much to be learned.

5.1.2 Computational

Thermochemical Non-Equilibrium Calculations: As a first suggestion, it is recommended that calculations similar to those done by Johnson *et al.* [51] be performed using appropriate boundary conditions to directly simulate the current experiments. The strong effect of thermochemical non-equilibrium effects on linear stability is well documented and

it is important to understand these effects in the context of the current experiments.

Hole Interaction Effects: The boundary conditions used in the linear stability analysis were derived for a single hole and then applied to the overall porous surface through the porosity coefficient. This approach neglects any interactions between the holes and is valid if the holes are widely spaced. In the present case, however, where the hole spacing is the same order as the hole diameter, such interactions may not be negligible. Melling [77] suggested that closely spaced holes are likely to exhibit a slightly lower input impedance based on physical arguments. Fedorov [30] imagined another scenario where a cumulative effect of disturbances emanating from the holes would significantly modify the external boundary layer downstream. In either case, the issue of hole interactions should be pursued.

Alternate Materials: The current boundary conditions used in the linear stability analysis were developed for a very specific surface microstructure. The theoretical models used to simulate the acoustic absorption properties of this specific microstructure can be extended somewhat to more general random porosity surfaces using correction factors. This work should be pursued. Ideally, a more general approach is desirable, perhaps one that somehow can make use of the results of static benchmark tests.

5.2 Final Word

The present work is one small step in gaining a better understanding of the complicated problem of boundary layer transition and control in hypervelocity flow. There is still much more work that needs to be done in this area from both the fundamental physics and the more practical engineering aspects. It is hoped that on-going experimental, computational and theoretical investigations will continue to push back the frontiers of knowledge in the realm of hypervelocity aerodynamics for applications on Earth and on other planets.

Bibliography

- [1] ADAM, P., *Enthalpy Effects on Hypervelocity Boundary Layers*, PhD thesis, California Institute of Technology, 1997.
- [2] ADAM, P. AND HORNUNG, H.G., “Enthalpy Effects on Hypervelocity Boundary Layer Transition: Ground Test and Flight Data,” *Journal of Spacecraft and Rockets*, 34(5):614–619, 1997.
- [3] ANDERSON, J.D., *Hypersonic and High Temperature Gas Dynamics*, McGraw-Hill Book Company, 1989.
- [4] ASTM, *Manual on the Use of Thermocouples in Temperature Measurement*, Fourth edition, 1993.
- [5] ATTENBOROUGH, K., “Acoustical Characteristics of Porous Materials,” *Physics Reports*, 82(3):179–227, 1982.
- [6] BENADE, A.H., “On the Propagation of Sound Waves in a Cylindrical Conduit,” *Journal of the Acoustical Society of America*, 44(2):616–623, 1968.
- [7] BERSHADER, D., PRAKASH, S.G., AND HUHN, G., “Improved Flow Visualization by Use of Resonant Refractivity,” *Progress in Astronautics and Aeronautics*, 53:595–609, 1977.
- [8] BERTIN, J.J., HAYDEN, T.E., AND GOODRICH, W.D., “Shuttle Boundary-Layer Transition Due to Distributed Surface Roughness and Surface Cooling,” *Journal of Spacecraft and Rockets*, 19(5):389–396, 1982.
- [9] BERTOLOTTI, F.P., “The Influence of Rotational and Vibrational Energy Relaxation on Boundary-Layer Stability,” *Journal of Fluid Mechanics*, 372:93–118, 1998.
- [10] BLOTTNER, F.G., JOHNSON, M., AND ELLIS, M.G., “Chemically Reacting Viscous Flow Program for Multi-Component Gas Mixtures,” Technical Report SC-RR-70-754, Sandia Laboratories, Albuquerque, N.M., December 1971.
- [11] BRASLOW, A.L., *A History of Suction-Type Laminar-Flow Control with Emphasis on Flight Research*, NASA History Division, 1999.
- [12] BROWN, R., DURBIN, J., AND EVANS, J., “Techniques for Testing the Constancy of Regression Relationships Over Time,” *Journal of the Royal Statistical Society*, 36:149–172, 1975.

- [13] CARMICHAEL, R.H., WHITES, R.C., AND PFENNINGER, W., “Low Drag Boundary Layer Suction Experiments in Flight on the Wing Glove of an F94A Airplane, Phase III: Laminar Suction Airfoil Tolerances,” Technical Report BLC-101 (NAI-57-1163), Northrop Aircraft Inc., 1957.
- [14] CARMICHAEL, R.H., WHITES, R.C., AND WISMA, R.E., “Low Drag Boundary Layer Suction Experiments in Flight on the Wing Glove of an F94A Airplane, Phase IV: Suction Through 81 Slots Between 8% Chord and 95% Chord,” Technical Report BLC-102 (NAI-57-1025), Northrop Aircraft Inc., 1957.
- [15] CHAPMAN, D.R. AND RUBESIN, M.W., “Temperature and Velocity Profiles in the Compressible Laminar Boundary Layer with Arbitrary Distribution of Surface Temperature,” *Journal of the Aeronautical Sciences*, 16:547–565, 1949.
- [16] CHEN, F.-J., MALIK, M.R., AND BECKWITH, I.E., “Boundary-Layer Transition on a Cone and a Flat Plate at Mach 3.5,” *AIAA Journal*, 27(6):687–693, 1989.
- [17] CHEN, F.-J., WILKINSON, S.P., AND BECKWITH, I.E., “Görtler Instability and Hypersonic Quiet Nozzle Design,” *AIAA Journal*, 30(2):170–175, 1993.
- [18] CLARKE, J.F. AND MCCHESENEY, M., *The Dynamics of Real Gases*, Butterworths, 1964.
- [19] COLLIER, F.S. “An Overview of Recent Subsonic Laminar Flow Control Flight Experiments,” AIAA Paper 93-2987, 1993 (21st AIAA Aerospace Sciences Meeting, January 10-13, Reno, NV, USA).
- [20] CRANDALL, I.B., *Theory of Vibrating Systems and Sound*, D. Van Nostrand Company, 1926.
- [21] CUMMINGS, E.B., *Laser-Induced Thermal Acoustics*, PhD thesis, California Institute of Technology, 1995.
- [22] DANIELS, F.B., “Acoustical Impedance of Enclosures,” *Journal of the Acoustical Society of America*, 19(4):569–571, 1947.
- [23] DANIELS, F.B., “On the Propagation of Sound Waves in a Cylindrical Conduit,” *Journal of the Acoustical Society of America*, 22(5):563–564, 1950.
- [24] DAVIS, J.P., *High-Enthalpy Shock/Boundary-Layer Interaction on a Double Wedge*, PhD thesis, California Institute of Technology, 1999.
- [25] DEMETRIADES, A., “An Experiment on the Stability of Hypersonic Laminar Boundary Layers,” *Journal of Fluid Mechanics*, 7(3):385–396, 1960.

- [26] DEMETRIADES, A. "Hypersonic Viscous Flow over a Slender Cone. Part III: Laminar Instability and Transition," AIAA Paper 74-535, 1974 (7th Fluid and Plasma Dynamics Conference, June 17-19, Palo Alto, CA, USA).
- [27] DICRISTINA, V., "Three Dimensional Laminar Boundary Transition on a Sharp 8 deg Cone at Mach 10," *AIAA Journal*, 8(5):852-856, 1970.
- [28] DORRANCE, W.H., *Viscous Hypersonic Flow*, McGraw-Hill Book Company, 1962.
- [29] ECKERT, E.R.G., "Engineering Relations for Friction and Heat Transfer to Surfaces in High Velocity Flow," *Journal of the Aeronautical Sciences*, 22:585-587, August 1955.
- [30] FEDOROV, A.V. Private Communication, 2000.
- [31] FEDOROV, A.V. AND MALMUTH, N.D., "Hypersonic Flow Stabilization by Ultrasonically Transparent Wall," Technical Report SCNM96-1, Rockwell Science Center, 1996.
- [32] FEDOROV, A.V., MALMUTH, N.D., RASHEED, A., AND HORNING, H.G. "Stabilization of Hypersonic Boundary Layer by Porous Coatings," AIAA Paper 2001-0891, 2001 (39th AIAA Aerospace Sciences Meeting and Exhibit, January 8-11, Reno, NV, USA).
- [33] FEDOROV, A.V., MALMUTH, N.D., SHALAEV, V., COLE, J., AND KHOKHLOV, A. "Problems in High Speed Flow Prediction Relevant to Control," AIAA Paper 98-2995, 1998 (2nd Theoretical Fluid Mechanics Meeting, June 15-18, Albuquerque, NM, USA).
- [34] GAPONOV, S.A., "Effect of the Behaviour of a Porous Covering on Boundary Layer Stability," *Izv. SO AN SSSR, Ser. Tech. Nauk*, 1(3):21-23, 1971 (in Russian).
- [35] GAPONOV, S.A., "Effect of Gas Compressibility on the Stability of a Boundary Layer Above a Permeable Surface at Subsonic Velocities," *Journal of Applied Mechanics and Technical Physics*, 16(1):95-99, 1975 (Translated from Zhurnal Prikladnoi Mekhaniki i Tekhnicheskoi Fiziki, Volume 16, Number 1, pp 121-125, January-February 1975).
- [36] GAPONOV, S.A., "Stability of a Supersonic Boundary Layer on a Permeable Surface with Heat Transfer," *Fluid Dynamics*, 12(1):33-37, 1977 (Translated from Izvestiya Akademiia Nauk SSSR, Mekhanika Zhidkosti i Gaza, Volume 12, Number 1, pp 41-46, January-February 1977).
- [37] GERMAIN, P., *The Boundary Layer on a Sharp Cone in High-Enthalpy Flow*, PhD thesis, California Institute of Technology, 1994.
- [38] GERMAIN, P. AND HORNING, H.G., "Transition on a Slender Cone in Hypervelocity Flow," *Experiments in Fluids*, 22:183-190, 1997.

- [39] GOLDSMITH, J., “Critical Suction Quantities and Pumping Losses Associated with Laminar Boundary Layer Suction Through Rows of Closely-Spaced Holes,” Technical Report BLC-72 (NAI-55-287), Northrop Aircraft Inc., February 1955.
- [40] GOLDSMITH, J., “Critical Laminar Suction Parameters for Suction into an Isolated Hole or a Single Row of Holes,” Technical Report BLC-95 (NAI-57-529), Northrop Aircraft Inc., 1957.
- [41] GOODRICH, W.D., DERRY, S.M., AND BERTIN, J.J., “Shuttle Orbiter Boundary Layer Transition at Flight and Wind Tunnel Conditions,” In *Shuttle Performance: Lessons Learned*, March 1983 (NASA Conference Publication 2283, Part 2).
- [42] GREENE, W.H., *Econometric Analysis*, Prentice Hall, 1997.
- [43] GROTH, E., CARMICHAEL, R.H., WHITES, R.C., AND PFENNINGER, W., “Low Drag Boundary Layer Suction Experiments in Flight on the Wing Glove of an F94A Airplane, Phase II: Suction Through 69 Slots,” Technical Report BLC-94 (NAI-57-318), Northrop Aircraft Inc., 1957.
- [44] HE, Y. AND MORGAN, R.G., “Transition of Compressible High Enthalpy Boundary Layer Flow over a Flat Plate,” *The Aeronautical Journal*, 98(971):25–34, 1994.
- [45] HOLDEN, M., “Studies of the Effects of Transitional and Turbulent Boundary Layers on the Aerodynamic Performance of Hypersonic Re-Entry Vehicles in High Reynolds Number Flows,” Technical Report AFOSR-TR-79-0125, Airforce Office of Scientific Research, 1978.
- [46] HORNUNG, H.G. “Performance Data of the new Free-Piston Shock Tunnel T5 at GALCIT,” AIAA Paper 92-3943, 1992 (17th Aerospace Ground Testing Conference, July 6-8, Nashville, TN, USA).
- [47] HORNUNG, H.G., “Experimental Hypervelocity Flow Simulation, Needs, Achievements and Limitations,” In *Proceedings of the Pacific International Conference on Aerospace Sciences and Technology (PICAST)*, volume 1, pages 1–10, 1993 (National Cheng Kung University, Tainan, Taiwan, China).
- [48] HORNUNG, H.G. AND BÉLANGER, J. “Role and Techniques of Ground Testing for Simulation of Flows up to Orbital Speed,” AIAA Paper 90-1377, 1990 (16th Aerodynamic Ground Testing Conference, June 18-20, Seattle, WA, USA).
- [49] HORNUNG, H.G., STURTEVANT, B., BÉLANGER, J., SANDERSON, S., AND BROUILLETTE, M., “Performance Data of the New Free-Piston Shock Tunnel T5 at GALCIT,” In *Proceedings of the 18th International Symposium on Shock Waves*, 1991 (Sendai, Japan).

- [50] HUDSON, M.L., CHOKANI, N., AND CANDLER, G., “Linear Stability of Hypersonic Flow in Thermochemical Nonequilibrium,” *AIAA Journal*, 35(6):958–964, 1997.
- [51] JOHNSON, H.B., SEIPP, T., AND CANDLER, G.V., “Numerical Study of Hypersonic Reacting Boundary Layer Transition on Cones,” *Physics of Fluids*, 10(10):2676–2685, October 1998.
- [52] JOSLIN, R.D., “Aircraft Laminar Flow Control,” *Annual Review of Fluid Mechanics*, 30:1–29, 1998.
- [53] KARAKASH, J.J., *Transmission Lines and Filter Networks*, The MacMillan Company, 1950.
- [54] KENDALL, D., DIXON, W.P., AND SCHULTE, E.H., “Semiconductor Surface Thermocouples for Determining Heat-Transfer Rates,” *IEEE Transactions on Aerospace and Electronic Systems*, 3(4):596–602, July 1967.
- [55] KENDALL, J.M. “Wind Tunnel Experiments Relating to Supersonic and Hypersonic Boundary-Layer Transition,” AIAA Paper 74-133, 1974 (12th AIAA Aerospace Sciences Meeting, January 30 - February 1, Washington, D.C., USA).
- [56] KENDALL, J.M., “Wind Tunnel Experiments Relating to Supersonic and Hypersonic Boundary-Layer Transition,” *AIAA Journal*, 13(3):290–299, 1975.
- [57] KESTIN, J. AND PERSEN, L.N., “The Transfer of Heat Across a Turbulent Boundary Layer at Very High Prandtl Numbers,” *International Journal of Heat and Mass Transfer*, 5:355–371, 1962.
- [58] KIMMEL, R., DEMETRIADES, A., AND DONALDSON, J., “Space-Time Correlation Measurements in a Hypersonic Transitional Boundary Layer,” *AIAA Journal*, 34(12):2484–2489, 1996.
- [59] KIMMEL, R.L. AND POGGIE, J., “Laminar-Turbulent Transition in a Mach 8 Elliptic Cone Flow,” *AIAA Journal*, 37(9):1080–1087, 1999.
- [60] KINSLER, L.E., FREY, A.R., COPPENS, A.B., AND SANDERS, J.V., *Fundamentals of Acoustics*, John Wiley and Sons, 2000.
- [61] KIRCHHOFF, G., “Über den Einfluss der Wärmeleitung in einem Gase auf die Schallbewegung,” *Poggendorfer Annalen*, 134:177–193, 1868.
- [62] KROGMANN, P., “Experimentelle Untersuchungen über Strömung an Kegeln,” *Z. Flugwiss. Weltraumforsch.*, 2:108–115, 1977.
- [63] LACHOWICZ, J.T., CHOKANI, N., AND WILKINSON, S.P., “Boundary-Layer Stability Measurements in a Hypersonic Quiet Tunnel,” *AIAA Journal*, 34(12):2496–2500, 1996.

- [64] LEES, L. AND LIN, C.C., "Investigation of the Stability of the Laminar Boundary Layer in a Compressible Fluid," Technical Report NACA TN-1115, National Advisory Committee for Aeronautics (NACA), 1946.
- [65] LEMIEUX, P., *The Instability of Shear Layers Produced by Curved Shocks*, PhD thesis, California Institute of Technology, 1999.
- [66] LORDI, J.A., MATES, R.E., AND MOSELLE, J.R., "Computer Program for the Numerical Solution of Nonequilibrium Expansions of Reacting Gas Mixtures," Technical Report NASA CR-472, National Aeronautics and Space Administration (NASA), 1966.
- [67] MACK, L., "Linear Stability Theory and the Problem of Supersonic Boundary-Layer Transition," *AIAA Journal*, 13(3):278–289, 1975.
- [68] MACK, L.M., "An Experimental Investigation of the Temperature Recovery Factor," Technical Report 20-80, Jet Propulsion Laboratory, California Institute of Technology, 1954.
- [69] MACK, L.M., "Boundary-Layer Stability Theory," In *Special Course on Stability and Transition of Laminar Flow*, AGARD Report Number 709, 1984.
- [70] MALIK, M.R., "Prediction and Control of Transition in Supersonic and Hypersonic Boundary Layers," *AIAA Journal*, 27(11):1487–1493, 1989.
- [71] MALIK, M.R. AND ANDERSON, E.C., "Real Gas Effects on Hypersonic Boundary-Layer Stability," *Physics of Fluids A*, 3(5):803–821, 1991.
- [72] MALMUTH, N.D., "Stability of the Inviscid Shock Layer in Strong Interaction Flow Over a Flat Plate," In *Instabilities and Turbulence in Engineering Flows*, pages 189–223. Kluwer Academic Publishers, 1993.
- [73] MAWARDI, O.K., "On the Propagation of Sound Waves in Narrow Conduits," *Journal of the Acoustical Society of America*, 21(5):482–486, 1949.
- [74] MCINTOSH, M.K., "A Computer Program for the Numerical Calculation of Equilibrium and Perfect Gas Conditions in Shock Tunnels," Technical Report CPD 169, Australian Defence Scientific Service, 1970.
- [75] MEE, D.J. "Boundary Layer Transition Measurements in Hypervelocity Flows in a Shock Tunnel," AIAA Paper 2001-0208, 2001 (39th AIAA Aerospace Sciences Meeting and Exhibit, January 8-11, Reno, NV, USA).
- [76] MEE, D.J. AND GOYNE, C.P., "Turbulent Spots in Boundary Layers in a Free-Piston Shock-Tunnel Flow," *Shock Waves*, 6:337–343, 1996.

- [77] MELLING, T.H., “The Acoustic Impedance of Perforates at Medium and High Sound Pressure Levels,” *Journal of Sound and Vibration*, 29(1):1–65, 1973.
- [78] MORKOVIN, M.V., “Viscous Drag Reduction,” In WELLS, C.S., editor, *On the Many Faces of Transition*, pages 1–31. Plenum Books, 1969.
- [79] MORSE, P.M. AND INGARD, K.U., *Theoretical Acoustics*, McGraw-Hill, 1968.
- [80] NORRIS, G., “Laminar Flow Control - Smooth and Supersonic,” *Flight International*, 145(4421):32–33, May 18-24 1994.
- [81] OLSON, H.F., *Dynamical Analogies*, D. Van Nostrand Company, 1943.
- [82] OLSON, H.F., *Elements of Acoustical Engineering*, D. Van Nostrand Company, 1947.
- [83] OLYNICK, D., CHEN, Y.-K., AND TAUBER, M., “Aerothermodynamics of the Stardust Sample Return Capsule,” *Journal of Spacecraft and Rockets*, 36(3):442–462, 1999.
- [84] PATE, S.R. AND SCHUELER, C.J., “Radiated Aerodynamic Noise Effects on Boundary-Layer Transition in Supersonic and Hypersonic Wind Tunnels,” *AIAA Journal*, 7(2):450–457, 1969.
- [85] PFENNINGER, W., “Laminar Flow Control,” In *Special Course on Concepts for Drag Reduction*, AGARD Report Number 654, 1977.
- [86] PFENNINGER, W., GROTH, E., CARMICHAEL, R.H., AND WHITES, R.C., “Low Drag Boundary Layer Suction Experiments in Flight on the Wing Glove of an F94A Airplane, Phase I: Suction Through 12 Slots,” Technical Report BLC-77 (NAI-55-458), Northrop Aircraft Inc., 1955.
- [87] PIERCE, A.D., *Acoustics: An Introduction to its Physical Principles and Applications*, Acoustical Society of America, 1989.
- [88] POGGIE, J. AND KIMMEL, R.L., “Traveling Instability Waves in a Mach 8 Flow over an Elliptic Cone,” *AIAA Journal*, 38(2):251–253, 2000.
- [89] PRESS, W.H., TEUKOLSKY, S.A., VETTERLING, W.T., AND FLANNERY, B.P., *Numerical Recipes in FORTRAN: The Art of Scientific Computing*, Cambridge University Press, 1992.
- [90] REDA, D.C., “Correlation of Noretip Boundary-Layer Transition Data Measured in Ballistics-Range Experiments,” *AIAA Journal*, 19(3):329–339, 1981.
- [91] REDA, D.C. “Roughness-Dominated Transition on Noretips, Attachment Lines and Lifting-Entry Vehicles,” AIAA Paper 2001-0205, 2001 (39th AIAA Aerospace Sciences Meeting and Exhibit, January 8-11, Reno, NV, USA).

- [92] REED, H., KIMMEL, R., SCHNEIDER, S., AND ARNAL, D. “Drag Prediction and Transition in Hypersonic Flow,” AIAA Paper 1997-1818, 1997 (28th Fluid Dynamics Conference, June 29-July 2, Snowmass Village, CO, USA).
- [93] REED, H.L., SARIC, W.S., AND ARNAL, D., “Linear Stability Theory Applied to Boundary Layers,” *Annual Review of Fluid Mechanics*, 28:389–428, 1996.
- [94] REIN, M., “SURF: A Program for Calculating Inviscid Supersonic Reacting Flows in Nozzles,” Technical Report FM 89-1, GALCIT, California Institute of Technology, 1989.
- [95] RESHOTKO, E., “Transition Reversal and Tollmien-Schlichting Instability,” *Physics of Fluids*, 6(3):335–342, 1963.
- [96] RESHOTKO, E., “Boundary-Layer Stability and Transition,” *Annual Review of Fluid Mechanics*, 8:311–349, 1976.
- [97] REYNOLDS, W.C., “The Element Potential Method of Chemical Equilibrium Analysis: Implementation in the Interactive Program STANJAN,” Technical report, Department of Mechanical Engineering, Stanford University, 1986.
- [98] ROUSSET, B., *Calibration and Study of the Contoured Nozzle of the T5 Free-Piston Hypervelocity Shock Tunnel*, Engineer’s thesis, California Institute of Technology, 1995.
- [99] RSHEVSKIN, S.N, *A Course of Lectures on the Theory of Sound*, The MacMillan Company, 1963 (Translated from Kurs Lektsii po Teorii Zvuka, Moscow State University, 1960).
- [100] SALYER, T.R., COLLICOTT, S.H., AND SCHNEIDER, S.P. “Feedback Stabilized Laser Differential Interferometry for Supersonic Blunt Body Receptivity Experiments,” AIAA Paper 2000-0416, 2000 (38th Aerospace Sciences Meeting and Exhibit, January 10-13, Reno, NV, USA).
- [101] SANDERSON, S.R., *Shock Wave Interaction in Hypervelocity Flow*, PhD thesis, California Institute of Technology, 1995.
- [102] SARIC, W.S., “Görtler Vortices,” *Annual Review of Fluid Mechanics*, 26:379–409, 1994.
- [103] SARIC, W.S., “Physical Description of Boundary-Layer Transition: Experimental Evidence,” Technical Report AG-793, AGARD, 1994.
- [104] SCHLICHTING, H., *Boundary Layer Theory*, McGraw-Hill Company, 1987.
- [105] SCHNEIDER, S. “Effects of High-Speed Tunnel Noise on Laminar-Turbulent Transition,” AIAA Paper 2000-2205, 2000 (21st Aerodynamic Measurement Technology and Ground Testing Conference, June 2000, Denver, CO, USA).

- [106] SCHUBAUER, G.B. AND SKRAMSTAD, H.K., “Laminar-Boundary-Layer Oscillations and Transition on a Flat Plate,” Technical Report NACA Report 909, National Advisory Committee for Aeronautics (NACA), 1948.
- [107] SCHULTZ, D.L. AND JONES, T.V., “Heat Transfer Measurements in Short Duration Hypersonic Facilities,” Technical Report AG-165, AGARD, 1973.
- [108] SMITH, A.M.O. AND CAMBERONI, N., “Transition, Pressure Gradient and Stability Theory,” Technical Report ED 26388, Douglas Aircraft Company, 1956.
- [109] SPALDING, D.B. AND CHI, S.W., “The Drag of a Compressible Turbulent Boundary Layer on a Smooth Flat Plate with and without Heat Transfer,” *Journal of Fluid Mechanics*, 18:117–143, 1964.
- [110] STETSON, K.F., “Mach 6 Experiments of Transition on a Cone at Angle of Attack,” *Journal of Spacecraft and Rockets*, 19(5):397–403, 1982.
- [111] STETSON, K.F., “Hypersonic Boundary-Layer Transition,” In BERTIN, J.J., PERIAUX, J., AND BALLMANN, J., editors, *Advances in Hypersonics: Volume I, Defining the Environment*, pages 324–417. Birkhäuser Boston, 1992.
- [112] STETSON, K.F. AND KIMMEL, R.L. “On Hypersonic Boundary-Layer Stability,” AIAA Paper 92-0737, 1992 (30th Aerospace Sciences Meeting and Exhibit, January 6-9, Reno, NV, USA).
- [113] STETSON, K.F. AND RUSHTON, G.H., “Shock Tunnel Investigation of Boundary-Layer Transition,” *AIAA Journal*, 5(5):899–906, 1967.
- [114] STETSON, K.F., THOMPSON, E.R., DONALDSON, J.C., AND SILER, L.G. “Laminar Boundary Layer Stability Experiments on a Cone at Mach 8. Part I: Sharp Cone,” AIAA Paper 83-1761, 1983 (16th Fluid and Plasma Dynamics Conference, July 12-14, Danvers, MA, USA).
- [115] STETSON, K.F., THOMPSON, E.R., DONALDSON, J.C., AND SILER, L.G. “Laminar Boundary Layer Stability Experiments on a Cone at Mach 8. Part II: Blunt Cone,” AIAA Paper 84-0006, 1984 (22nd Aerospace Sciences Meeting and Exhibit, January 9-12, Reno, NV, USA).
- [116] STETSON, K.F., THOMPSON, E.R., DONALDSON, J.C., AND SILER, L.G. “Laminar Boundary Layer Stability Experiments on a Cone at Mach 8. Part III: Sharp Cone at Angle of Attack,” AIAA Paper 85-0492, 1985 (23rd Aerospace Sciences Meeting and Exhibit, January 14-17, Reno, NV, USA).
- [117] STETSON, K.F., THOMPSON, E.R., DONALDSON, J.C., AND SILER, L.G. “Laminar Boundary Layer Stability Experiments on a Cone at Mach 8. Part IV: On Unit Reynolds Number and

- Environmental Effects,” AIAA Paper 86-1087, 1986 (4th Fluid Mechanics, Plasma Dynamics and Laser Conference, May 12-14 Atlanta, GA, USA).
- [118] STETSON, K.F., THOMPSON, E.R., DONALDSON, J.C., AND SILER, L.G. “Laminar Boundary Layer Stability Experiments on a Cone at Mach 8. Part V: Tests With a Cooled Model,” AIAA Paper 89-1895, 1989 (20th Fluid Mechanics, Plasma Dynamics and Laser Conference, June 12-14, Buffalo, NY, USA).
- [119] STINSON, M.R., “The Propagation of Plane Sound Waves in Narrow and Wide Circular Tubes, and Generalization to Uniform Tubes of Arbitrary Cross-Sectional Shape,” *Journal of the Acoustical Society of America*, 89(2):550–559, 1991.
- [120] STINSON, M.R. AND CHAMPOUX, Y., “Propagation of Sound and the Assignment of Shape Factors in Model Porous Materials Having Simple Pore Geometries,” *Journal of the Acoustical Society of America*, 91(2):685–695, 1992.
- [121] STRUTT, J. (LORD RAYLEIGH), *Theory of Sound*, volume 2, Dover, 1894.
- [122] STUCKERT, G. AND REED, H., “Linear Disturbances in Hypersonic, Chemically Reacting Shock Layers,” *AIAA Journal*, 32(7):1384–1393, 1994.
- [123] SUDANI, N. AND HORNUNG, H.G., “Gasdynamical Detectors of Driver Gas Contamination in a High-Enthalpy Shock Tunnel,” *AIAA Journal*, 36(3):313–319, 1998.
- [124] SUDANI, N., VALIFERDOWSI, B., AND HORNUNG, H.G., “Test Time Increase by Delaying Driver Gas Contamination for Reflected Shock Tunnels,” *AIAA Journal*, 38(9):596–600, September 2000.
- [125] SUNDQVIST, B., “Thermal Diffusivity and Thermal Conductivity of Chromel, Alumel, and Constantan in the Range 100-450 K,” *Journal of Applied Physics*, 72(2):539–545, 1972.
- [126] TAUBER, M.E., “Aerothermodynamics of Transatmospheric Vehicles,” *Journal of Aircraft*, 24(9):594–602, 1987.
- [127] TAYLOR, G.I. AND MACCOLL, J.W., “The Air Pressure on a Cone Moving at High Speed,” *Proceedings of the Royal Society of London*, 139, 1933.
- [128] TIJDEMAN, H., “On the Propagation of Sound Waves in Cylindrical Tubes,” *Journal of Sound and Vibrations*, 39(1):1–33, 1975.
- [129] VAN DRIEST, E.R., “Turbulent Boundary Layer on a Cone in a Supersonic Flow at Zero Angle of Attack,” *Journal of the Aeronautical Sciences*, pages 55–57, 72, 1952.

- [130] VAN DRIEST, E.R., "The Problem of Aerodynamic Heating," *Aeronautical Engineering Review*, 15(10):26–41, October 1956.
- [131] WESTON, D.E., "The Theory of the Propagation of Plane Sound Waves in Tubes," *Proceedings of the Physics Society of London, Section B*, 66:695–709, 1953.
- [132] WHITE, F.M., *Viscous Fluid Flow*, McGraw-Hill, Inc., Second edition, 1991.
- [133] WHITE, F.M. AND CHRISTOPH, G.H., "A Simple Theory for The Two-Dimensional Compressible Turbulent Boundary Layer," *Journal of Basic Engineering*, 94:636–642, September 1972.
- [134] WILKE, C.R., "A Viscosity Equation for Gas Mixtures," *Journal of Chemical Physics*, 18(4):517–519, April 1950.
- [135] WRIGHT, R.L. AND ZOBY, E.V. "Flight Boundary Layer Transition Measurements on a Slender Cone at Mach 20," AIAA Paper 77-719, 1977 (10th Fluid and Plasma Dynamics Conference, June 1977, Albuquerque, NM, USA).
- [136] ZURIGAT, Y.H., NAYFEH, A.H., AND MASAD, J.A., "Effect of Pressure Gradient on the Stability of Compressible Boundary Layers," *AIAA Journal*, 30(9):2204–2211, 1992.
- [137] ZWIKKER, C. AND KOSTEN, C.W., *Sounds Absorbing Materials*, Elsevier Publishing Company, 1949.

Appendix A Test Conditions

Table A.1: Summary of the freestream conditions for the N₂ shots. These were computed using the NENZF non-equilibrium nozzle code as described in Section 3.2.3.

Shot	P_o (MPa)	h_o (MJ/kg)	T_o (K)	P_∞ (kPa)	T_∞ (K)	ρ_∞ (kg/m ³)	u_∞ (m/s)	M_∞
1959	45.0	7.2	5601	15.1	889	5.72×10^{-2}	3537	5.9
1960	51.5	13.1	8081	22.4	1858	4.05×10^{-2}	4661	5.5
1961	52.0	13.3	8153	22.9	1909	4.03×10^{-2}	4702	5.5
1962	47.0	7.2	5617	15.7	892	5.94×10^{-2}	3542	5.9
1963	45.6	7.2	5585	15.3	885	5.82×10^{-2}	3531	5.9
1964	48.4	9.0	6633	17.8	1154	5.19×10^{-2}	3935	5.8
1965	49.9	10.4	7235	19.3	1380	4.71×10^{-2}	4211	5.7
1966	48.1	10.3	7197	18.6	1363	4.59×10^{-2}	4191	5.7
1967	49.2	8.0	6113	17.9	1025	5.87×10^{-2}	3720	5.8
1968	13.7	5.2	4218	4.5	600	2.50×10^{-2}	3026	6.1
1969	10.3	3.5	2959	3.0	372	2.73×10^{-2}	2514	6.4
1970	11.6	4.2	3443	3.5	458	2.59×10^{-2}	2721	6.3
1971	49.2	9.0	6619	18.0	1149	5.29×10^{-2}	3929	5.8
1972	50.5	12.1	7799	21.0	1669	4.23×10^{-2}	4500	5.6
1973	49.5	10.7	7347	19.4	1427	4.58×10^{-2}	4263	5.7
1974	48.6	7.9	6035	17.6	1003	5.89×10^{-2}	3688	5.8
1975	50.0	12.1	7820	20.9	1684	4.17×10^{-2}	4513	5.6
1976	14.5	5.0	4030	4.5	567	2.68×10^{-2}	2954	6.1
1977	48.2	8.1	6153	17.2	1017	5.69×10^{-2}	3742	5.9
1978	14.4	5.4	4387	4.7	634	2.45×10^{-2}	3088	6.1
1981	49.6	7.8	6008	17.9	998	6.04×10^{-2}	3680	5.8
1999	48.6	10.0	7075	18.5	1311	4.75×10^{-2}	4132	5.8
2000	49.1	9.8	6996	18.6	1279	4.89×10^{-2}	4095	5.8
2003	48.0	10.1	7096	18.3	1320	4.68×10^{-2}	4143	5.8
2004	48.3	10.0	7071	18.4	1310	4.73×10^{-2}	4131	5.8
2006	47.6	10.0	7055	18.1	1305	4.67×10^{-2}	4124	5.8
2007	49.1	7.7	5935	17.3	963	6.06×10^{-2}	3659	5.9
2008	48.2	9.8	6977	18.2	1273	4.81×10^{-2}	4087	5.8
2009	48.7	10.0	7079	18.6	1313	4.76×10^{-2}	4134	5.8

Table A.2: Summary of the edge and reference conditions for the N₂ shots. These were computed by solving the Taylor-Maccoll equations and assuming frozen composition from the freestream, through the weak attached shock, and to the boundary layer edge. The reference conditions were computed at the reference temperature assuming constant pressure and frozen composition within the boundary layer.

Shot	P_e (kPa)	T_e (K)	ρ_e (kg/m ³)	u_e (m/s)	M_e	Unit Re _e (1/m)	T^* (K)	ρ^* (kg/m ³)	Unit Re [*] (1/m)
1959	23.2	1005	7.76×10^{-2}	3566	5.5	7.01×10^6	1845	4.23×10^{-2}	2.49×10^6
1960	33.0	2077	5.35×10^{-2}	4804	5.2	3.78×10^6	3346	3.23×10^{-2}	1.65×10^6
1961	33.7	2132	5.31×10^{-2}	4851	5.2	3.83×10^6	3415	3.37×10^{-2}	1.68×10^6
1962	24.2	1008	8.06×10^{-2}	3572	5.5	7.28×10^6	1850	4.40×10^{-2}	2.59×10^6
1963	23.4	1002	7.89×10^{-2}	3560	5.5	7.13×10^6	1838	4.30×10^{-2}	2.54×10^6
1964	27.0	1301	6.99×10^{-2}	4000	5.4	5.92×10^6	2299	3.96×10^{-2}	2.23×10^6
1965	29.1	1551	6.31×10^{-2}	4302	5.4	5.08×10^6	2659	3.68×10^{-2}	2.00×10^6
1966	28.0	1532	6.14×10^{-2}	4281	5.4	4.96×10^6	2630	3.58×10^{-2}	1.95×10^6
1967	27.2	1156	7.92×10^{-2}	3767	5.4	6.86×10^6	2056	4.45×10^{-2}	2.56×10^6
1968	7.0	682	3.43×10^{-2}	3018	5.7	3.42×10^6	1342	1.75×10^{-2}	1.09×10^6
1969	4.9	426	3.84×10^{-2}	2493	5.9	4.29×10^6	943	1.73×10^{-2}	1.14×10^6
1970	5.6	523	3.60×10^{-2}	2702	5.8	3.81×10^6	1093	1.72×10^{-2}	1.11×10^6
1971	27.4	1295	7.13×10^{-2}	3990	5.4	6.04×10^6	2288	4.04×10^{-2}	2.27×10^6
1972	31.2	1870	5.62×10^{-2}	4623	5.2	4.24×10^6	3085	3.41×10^{-2}	1.78×10^6
1973	29.1	1604	6.12×10^{-2}	4359	5.3	4.87×10^6	2731	3.59×10^{-2}	1.94×10^6
1974	26.7	1131	7.95×10^{-2}	3733	5.4	6.92×10^6	2020	4.45×10^{-2}	2.57×10^6
1975	31.0	1886	5.54×10^{-2}	4637	5.2	4.17×10^6	3105	3.36×10^{-2}	1.75×10^6
1976	7.1	645	3.69×10^{-2}	2942	5.7	3.71×10^6	1281	1.85×10^{-2}	1.17×10^6
1977	26.3	1148	7.70×10^{-2}	3789	5.5	6.74×10^6	2068	4.28×10^{-2}	2.46×10^6
1978	7.3	720	3.41×10^{-2}	3084	5.6	3.34×10^6	1399	1.75×10^{-2}	1.09×10^6
1981	27.2	1125	8.16×10^{-2}	3724	5.4	7.12×10^6	2011	4.56×10^{-2}	2.64×10^6
1999	28.0	1476	6.38×10^{-2}	4216	5.4	5.21×10^6	2552	3.69×10^{-2}	2.03×10^6
2000	28.1	1440	6.56×10^{-2}	4174	5.4	5.40×10^6	2502	3.78×10^{-2}	2.09×10^6
2003	27.7	1486	6.28×10^{-2}	4227	5.4	5.10×10^6	2566	3.63×10^{-2}	1.99×10^6
2004	27.8	1474	6.35×10^{-2}	4214	5.4	5.18×10^6	2550	3.67×10^{-2}	2.02×10^6
2006	27.4	1469	6.27×10^{-2}	4207	5.4	5.13×10^6	2542	3.63×10^{-2}	1.99×10^6
2007	26.5	1088	8.21×10^{-2}	3698	5.5	7.29×10^6	1974	4.52×10^{-2}	2.63×10^6
2008	27.5	1434	6.46×10^{-2}	4166	5.4	5.32×10^6	2491	3.72×10^{-2}	2.06×10^6
2009	28.0	1477	6.39×10^{-2}	4217	5.4	5.21×10^6	2554	3.70×10^{-2}	2.03×10^6

Table A.3: Summary of the transition data for the N₂ shots.

Shot	h_o (MJ/kg)	Smooth Surface			Porous Surface			Comments
		x_{tr} (mm)	Re_{tr}	Re_{tr}^*	x_{tr} (mm)	Re_{tr}	Re_{tr}^*	
1959	7.2	341	2.39×10^6	8.50×10^5	496	3.48×10^6	1.24×10^6	
1960	13.1	814	3.08×10^6	1.34×10^6	814	3.08×10^6	1.34×10^6	S1, P1
1961	13.3	814	3.11×10^6	1.37×10^6	814	3.11×10^6	1.37×10^6	S1, P1
1962	7.2	333	2.42×10^6	8.63×10^5	465	3.38×10^6	1.20×10^6	
1963	7.2	361	2.57×10^6	9.15×10^5	524	3.73×10^6	1.33×10^6	
1964	9.0	424	2.51×10^6	9.44×10^5	484	2.87×10^6	1.08×10^6	
1965	10.4	401	2.04×10^6	8.04×10^5	814	4.13×10^6	1.63×10^6	P1
1966	10.3	429	2.13×10^6	8.38×10^5	814	4.04×10^6	1.59×10^6	P1
1967	8.0	372	2.55×10^6	9.53×10^5	510	3.50×10^6	1.30×10^6	
1968	5.2	491	1.68×10^6	5.35×10^5	814	2.78×10^6	8.88×10^5	P1
1969	3.5	478	2.05×10^6	5.47×10^5	814	3.49×10^6	9.32×10^5	P1
1970	4.2	489	1.87×10^6	5.44×10^5	814	3.10×10^6	9.05×10^5	P1
1971	9.0	400	2.42×10^6	9.09×10^5	512	3.10×10^6	1.16×10^6	
1972	12.1	702	2.98×10^6	1.25×10^6	814	3.46×10^6	1.45×10^6	P1
1973	10.7	624	3.04×10^6	1.21×10^6	814	3.96×10^6	1.58×10^6	P1
1974	7.9	387	2.68×10^6	9.95×10^5	528	3.66×10^6	1.36×10^6	
1975	12.1	637	2.66×10^6	1.12×10^6	814	3.39×10^6	1.43×10^6	P1
1976	5.0	465	1.72×10^6	5.43×10^5	814	3.02×10^6	9.50×10^5	P1
1977	8.1	410	2.76×10^6	1.01×10^6	514	3.47×10^6	1.27×10^6	
1978	5.4	559	1.87×10^6	6.07×10^5	814	2.72×10^6	8.85×10^5	P1
1981	7.8	361	2.57×10^6	9.51×10^5	492	3.50×10^6	1.30×10^6	
1999	10.0	443	2.31×10^6	8.98×10^5	635	3.31×10^6	1.29×10^6	
2000	9.8	453	2.44×10^6	9.44×10^5	673	3.63×10^6	1.40×10^6	
2003	10.1	466	2.38×10^6	9.28×10^5	695	3.55×10^6	1.38×10^6	
2004	10.0	461	2.39×10^6	9.29×10^5	814	4.22×10^6	1.64×10^6	P1
2006	10.0	461	2.36×10^6	9.18×10^5	814	4.18×10^6	1.62×10^6	P1
2007	7.7	N/A	N/A	N/A	N/A	N/A	N/A	S2, P2
2008	9.8	485	2.58×10^6	9.98×10^5	814	4.33×10^6	1.67×10^6	P1
2009	10.0	470	2.45×10^6	9.54×10^5	814	4.24×10^6	1.65×10^6	P1

S1: Smooth surface was fully laminar. S2: Smooth surface was fully turbulent. P1: Porous surface was fully laminar. P2: Porous surface was fully turbulent.

Table A.4: Freestream molecular weight (g/mol) and species concentrations (mole fractions) for the N₂ shots as computed by NENZF.

Shot	MW	[N ₂]	[N]
1959	28.0	1.00	0.00
1960	27.9	1.00	0.00
1961	27.9	0.99	0.01
1962	28.0	1.00	0.00
1963	28.0	1.00	0.00
1964	28.0	1.00	0.00
1965	28.0	1.00	0.00
1966	28.0	1.00	0.00
1967	28.0	1.00	0.00
1968	28.0	1.00	0.00
1969	28.0	1.00	0.00
1970	28.0	1.00	0.00
1971	28.0	1.00	0.00
1972	28.0	1.00	0.00
1973	28.0	1.00	0.00
1974	28.0	1.00	0.00
1975	28.0	1.00	0.00
1976	28.0	1.00	0.00
1977	28.0	1.00	0.00
1978	28.0	1.00	0.00
1981	28.0	1.00	0.00
1999	28.0	1.00	0.00
2000	28.0	1.00	0.00
2003	28.0	1.00	0.01
2004	28.0	1.00	0.00
2006	28.0	1.00	0.00
2007	28.0	1.00	0.00
2008	28.0	1.00	0.00
2009	28.0	1.00	0.00

Table A.5: Summary of the freestream conditions for the CO₂ shots. These were computed using the NENZF non-equilibrium nozzle code as described in Section 3.2.3.

Shot	P_o (MPa)	h_o (MJ/kg)	T_o (K)	P_∞ (kPa)	T_∞ (K)	ρ_∞ (kg/m ³)	u_∞ (m/s)	M_∞
1979	40.5	6.0	3637	28.8	1516	9.66×10^{-2}	2749	4.6
1982	40.7	6.8	3835	30.6	1734	8.85×10^{-2}	2887	4.5
1983	42.6	4.8	4242	35.0	2183	7.73×10^{-2}	3158	4.5
1984	41.6	5.9	3621	29.4	1497	1.00×10^{-1}	2736	4.6
1985	38.5	4.3	3134	23.9	1058	1.17×10^{-1}	2405	4.8
1986	10.1	2.0	1927	4.7	444	5.65×10^{-2}	1756	5.4
1987	12.9	1.9	1889	5.9	429	7.31×10^{-2}	1736	5.3
1988	39.4	6.5	3758	29.0	1647	8.89×10^{-2}	2835	4.5
1989	34.2	5.1	3368	22.6	1257	9.25×10^{-2}	2568	4.7
1990	9.5	2.5	2224	4.8	557	4.51×10^{-2}	1901	5.1
1991	42.2	8.1	4155	34.3	2104	7.93×10^{-2}	3101	4.5
1992	39.8	6.1	3663	28.5	1543	9.38×10^{-2}	2768	4.6
1993	33.9	5.2	3397	22.6	1284	9.05×10^{-2}	2589	4.7
1994	42.2	3.9	2993	25.2	954	1.38×10^{-1}	2313	4.9
1995	11.2	2.6	2325	5.8	596	5.10×10^{-2}	1949	5.1
1997	11.8	3.9	2904	6.8	893	3.95×10^{-2}	2277	4.9
1998	14.3	2.6	2324	7.4	596	6.51×10^{-2}	1948	5.1
2001	14.4	1.3	1426	5.4	257	1.11×10^{-1}	1479	5.7
2002	10.3	1.4	1496	4.0	282	7.51×10^{-2}	1521	5.6

Table A.6: Summary of the edge and reference conditions for the CO₂ shots. These were computed by solving the Taylor-Maccoll equations and assuming frozen composition from the freestream, through the weak attached shock, and to the boundary layer edge. The reference conditions were computed at the reference temperature assuming constant pressure and frozen composition within the boundary layer.

Shot	P_e (kPa)	T_e (K)	ρ_e (kg/m ³)	u_e (m/s)	M_e	Unit Re_e (1/m)	T^* (K)	ρ^* (kg/m ³)	Unit Re^* (1/m)
1979	37.4	1586	1.20×10^{-1}	2720	4.4	6.84×10^6	1431	1.33×10^{-1}	8.19×10^6
1982	39.4	1808	1.09×10^{-1}	2856	4.3	5.89×10^6	1565	1.26×10^{-1}	7.58×10^6
1983	44.2	2227	9.57×10^{-2}	3124	4.4	4.77×10^6	1577	1.35×10^{-1}	8.68×10^6
1984	38.3	1567	1.25×10^{-1}	2707	4.4	7.13×10^6	1418	1.38×10^{-1}	8.50×10^6
1985	31.8	1115	1.48×10^{-1}	2380	4.7	9.76×10^6	1120	1.48×10^{-1}	9.69×10^6
1986	6.7	483	7.34×10^{-2}	1738	5.0	6.87×10^6	685	5.18×10^{-2}	3.67×10^6
1987	8.4	468	9.51×10^{-2}	1719	5.0	9.04×10^6	672	6.62×10^{-2}	4.71×10^6
1988	37.6	1720	1.10×10^{-1}	2805	4.4	6.06×10^6	1514	1.25×10^{-1}	7.58×10^6
1989	30.2	1345	1.16×10^{-1}	2626	4.5	7.25×10^6	1270	1.23×10^{-1}	8.02×10^6
1990	6.6	601	5.81×10^{-2}	1882	4.9	4.94×10^6	769	4.54×10^{-2}	3.17×10^6
1991	43.4	2157	9.81×10^{-2}	3067	4.4	4.93×10^6	1588	1.33×10^{-1}	8.40×10^6
1992	37.0	1614	1.17×10^{-1}	2738	4.4	6.59×10^6	1448	1.30×10^{-1}	7.97×10^6
1993	29.7	1348	1.13×10^{-1}	2561	4.5	6.90×10^6	1253	9.27×10^{-2}	7.61×10^6
1994	33.8	1009	1.75×10^{-1}	2290	4.7	1.20×10^7	1049	1.68×10^{-1}	1.12×10^7
1995	8.0	640	6.56×10^{-2}	1929	4.9	5.43×10^6	797	5.27×10^{-2}	3.67×10^6
1997	9.2	948	5.02×10^{-2}	2254	4.7	3.54×10^6	1018	4.67×10^{-2}	3.11×10^6
1998	10.2	640	8.37×10^{-2}	1929	4.9	6.93×10^6	797	6.72×10^{-2}	4.68×10^6
2001	8.1	288	1.48×10^{-1}	1465	5.3	1.78×10^7	534	7.99×10^{-2}	5.82×10^6
2002	5.9	315	9.95×10^{-2}	1506	5.2	1.14×10^7	560	5.60×10^{-2}	4.04×10^6

Table A.7: Summary of the transition data for the CO₂ shots.

Shot	h_o (MJ/kg)	Smooth Surface			Porous Surface			Comments	
		x_{tr} (mm)	Re_{tr}	Re_{tr}^*	x_{tr} (mm)	Re_{tr}	Re_{tr}^*		
1979	6.0	591	3.99×10^6	4.77×10^6	N/A	N/A	N/A	P2	
1982	6.8	700	4.12×10^6	5.30×10^6	356	2.09×10^6	2.69×10^6		
1983	8.5	700	3.34×10^6	6.08×10^6	489	2.33×10^6	4.25×10^6		
1984	5.9	553	3.94×10^6	4.70×10^6	340	2.43×10^6	2.89×10^6		
1985	4.3	351	3.43×10^6	3.40×10^6	302	2.95×10^6	2.93×10^6		
1986	2.0	432	2.97×10^6	1.58×10^6	645	4.43×10^6	2.37×10^6		
1987	1.9	425	3.85×10^6	2.00×10^6	723	6.54×10^6	3.40×10^6		
1988	6.5	690	4.18×10^6	5.23×10^6	478	2.90×10^6	3.62×10^6		
1989	5.1	542	3.93×10^6	4.35×10^6	491	3.56×10^6	3.94×10^6		
1990	2.5	612	3.02×10^6	1.94×10^6	649	3.21×10^6	2.06×10^6		
1991	8.1	702	3.46×10^6	5.89×10^6	494	2.44×10^6	4.15×10^6		
1992	6.1	696	4.58×10^6	5.54×10^6	500	3.30×10^6	3.98×10^6		
1993	5.2	479	3.31×10^6	3.64×10^6	323	2.23×10^6	2.46×10^6		
1994	3.9	N/A	N/A	N/A	N/A	N/A	N/A		S2, P2
1995	2.6	594	3.22×10^6	2.18×10^6	814	4.42×10^6	2.99×10^6		P1
1997	3.9	707	2.50×10^6	2.20×10^6	691	2.44×10^6	2.15×10^6		
1998	2.6	398	2.76×10^6	1.86×10^6	388	2.69×10^6	1.82×10^6		
2001	1.3	N/A	N/A	N/A	N/A	N/A	N/A		S2, P2
2002	1.4	265	3.02×10^6	1.07×10^6	635	7.26×10^6	2.56×10^6		

S1: Smooth surface was fully laminar. S2: Smooth surface was fully turbulent. P1: Porous surface was fully laminar. P2: Porous surface was fully turbulent.

Table A.8: Freestream molecular weight (g/mol) and species concentrations (mole fractions) for the CO₂ shots as computed by NENZF.

Shot	MW	[CO ₂]	[O ₂]	[CO]	[O]	[C]
1979	42.4	0.89	0.04	0.08	0.00	0.00
1982	41.7	0.84	0.05	0.10	0.00	0.00
1983	40.1	0.74	0.08	0.17	0.01	0.00
1984	42.4	0.89	0.04	0.07	0.00	0.00
1985	43.3	0.95	0.02	0.03	0.00	0.00
1986	44.0	1.00	0.00	0.00	0.00	0.00
1987	44.0	1.00	0.00	0.00	0.00	0.00
1988	41.9	0.86	0.05	0.09	0.00	0.00
1989	42.9	0.92	0.03	0.05	0.00	0.00
1990	43.8	0.99	0.00	0.00	0.00	0.00
1991	42.9	0.76	0.08	0.16	0.00	0.00
1992	42.3	0.88	0.04	0.08	0.00	0.00
1993	42.8	0.92	0.03	0.05	0.00	0.00
1994	43.5	0.97	0.01	0.02	0.00	0.00
1995	43.8	0.99	0.00	0.01	0.00	0.00
1997	43.1	0.94	0.02	0.04	0.00	0.00
1998	43.8	0.99	0.00	0.01	0.00	0.00
2001	44.0	1.00	0.00	0.00	0.00	0.00
2002	44.0	1.00	0.00	0.00	0.00	0.00

Appendix B Kirchhoff Solution for Acoustic Propagation in an Infinite Tube

A concise summary of the analysis by Kirchhoff [61] is also provided in Rayleigh [121], Stinson [119], and Zwikker and Kosten [137]. The analysis begins by considering a tube of general constant cross-section containing a perfect gas with viscosity (μ) and thermal conductivity (k). For the case of an acoustic plane wave, the linearized continuity, momentum and energy equations are

$$\frac{\partial \rho}{\partial t} = -\rho_o \nabla \cdot \mathbf{V}, \quad (\text{B.1})$$

$$\rho_o \frac{\partial \mathbf{V}}{\partial t} = -\nabla p + \frac{4}{3} \mu \nabla (\nabla \cdot \mathbf{V}) - \mu \nabla \times \nabla \times \mathbf{V}, \quad (\text{B.2})$$

$$k \nabla^2 T = \frac{T_o}{P_o} \left(\rho_o C_v \frac{\partial p}{\partial t} - P_o C_p \frac{\partial \rho}{\partial t} \right), \quad (\text{B.3})$$

where p , T , ρ , \mathbf{V} are the disturbance pressure, temperature, density and vector particle velocity, respectively. The subscript o is used to denote equilibrium values. C_v and C_p are the specific heats at constant volume and pressure, respectively. At this point, it may seem restrictive to limit the analysis to plane waves. It, however, can be shown that for the case where the acoustic wavelength is much larger than the tube cross-section, any non-uniformities in the acoustic wave will quickly damp out. This is indeed the case for most practical applications; therefore, this assumption does not restrict the usefulness of this analysis. The equation of state is

$$\frac{\partial p}{\partial t} = \frac{P_o}{\rho_o T_o} \left(\rho_o \frac{\partial T}{\partial t} + T_o \frac{\partial \rho}{\partial t} \right). \quad (\text{B.4})$$

Assuming complex time-dependant disturbances of the form

$$p = p e^{j\omega t}, \quad T = T e^{j\omega t}, \quad \rho = \rho e^{j\omega t}, \quad \mathbf{V} = \mathbf{v} e^{j\omega t}, \quad (\text{B.5})$$

where ω is the angular frequency and t is time. Substituting into Equations B.1 - B.4, one then obtains

$$j\omega\rho = -\rho_o\nabla \cdot \mathbf{v}, \quad (\text{B.6})$$

$$j\omega\rho_o\mathbf{v} = -\nabla p + \frac{4}{3}\mu\nabla(\nabla \cdot \mathbf{v}) - \mu\nabla \times \nabla \times \mathbf{v}, \quad (\text{B.7})$$

$$k\nabla^2 T = j\omega\frac{T_o}{P_o}(\rho_o C_v p - P_o C_p \rho), \quad (\text{B.8})$$

$$p = \frac{P_o}{\rho_o T_o}(\rho_o T + T_o \rho). \quad (\text{B.9})$$

Since the boundary conditions require that the disturbance velocity and temperature be zero at the tube walls, the above system of equations can be simplified and expressed in terms of T and \mathbf{v} as

$$j\omega\rho_o\mathbf{v} = -\frac{P_o}{T_o}\nabla T + \left(\frac{P_o}{j\omega} + \frac{4}{3}\mu\right)\nabla(\nabla \cdot \mathbf{v}) - \mu(\nabla \times \nabla \times \mathbf{v}), \quad (\text{B.10})$$

$$k\nabla^2 T = j\omega\rho_o C_v T + \rho_o T_o(C_p - C_v)\nabla \cdot \mathbf{v}. \quad (\text{B.11})$$

Defining the constants $\nu = \mu/\rho_o$ and $\nu' = k/(\rho_o C_v)$ and making use of the following relations for ideal gases

$$C_p - C_v = \frac{P_o}{\rho_o T_o}, \quad (\text{B.12})$$

$$c^2 = \frac{\gamma P_o}{\rho_o}, \quad (\text{B.13})$$

where γ is the ratio of specific heats and c is the adiabatic speed of sound, the final equations to be solved are

$$j\omega\mathbf{v} = -\frac{c^2}{\gamma T_o}\nabla T + \left(\frac{c^2}{j\omega\gamma} + \frac{4}{3}\nu\right)\nabla(\nabla \cdot \mathbf{v}) - \nu(\nabla \times \nabla \times \mathbf{v}), \quad (\text{B.14})$$

$$\nu'\nabla^2 T = j\omega T + (\gamma - 1)T_o\nabla \cdot \mathbf{v}. \quad (\text{B.15})$$

The above equations are general for any constant cross-sectional shape. The solution by Kirchhoff was for a tube of circular cross-section with radius r_w and assumed the vector velocity of the form $\mathbf{v} = u_x\hat{x} + u_r\hat{r}$ where \hat{x} and \hat{r} are unit vectors along the axis of propagation and the radial direction, respectively. The solutions, given by Kirchhoff, are

then

$$u_x = [AQ - A_1\Lambda\left(\frac{j\omega}{\lambda_1} - \nu'\right)Q_1 - A_2\Lambda\left(\frac{j\omega}{\lambda_2} - \nu'\right)Q_2]e^{\Lambda x}, \quad (\text{B.16})$$

$$u_r = \left[-\frac{A\Lambda}{(j\omega/\nu) - \Lambda^2} \frac{dQ}{dr} - A_1 \left(\frac{j\omega}{\lambda_1} - \nu' \right) \frac{dQ_1}{dr} - A_2 \left(\frac{j\omega}{\lambda_2} - \nu' \right) \frac{dQ_2}{dr} \right] e^{\Lambda x}, \quad (\text{B.17})$$

$$T = (\gamma - 1)T_o(A_1Q_1 + A_2Q_2)e^{\Lambda x}, \quad (\text{B.18})$$

where A , A_1 , A_2 are unknown quantities still to be determined and where

$$Q = J_0[r(\Lambda^2 - \frac{j\omega}{\nu})^{1/2}], \quad (\text{B.19})$$

$$Q_1 = J_0[r(\Lambda^2 - \lambda_1)^{1/2}], \quad (\text{B.20})$$

$$Q_2 = J_0[r(\Lambda^2 - \lambda_2)^{1/2}], \quad (\text{B.21})$$

where Λ is the propagation constant, J_0 is the Bessel function of the first kind of order zero and where λ_1 and λ_2 are the roots of

$$\lambda^2 \left(\frac{c^2\nu'}{j\omega\gamma} + \frac{4}{3}\nu\nu' \right) - \lambda \left[c^2 + j\omega \left(\frac{4}{3}\nu + \nu' \right) \right] - \omega^2 = 0. \quad (\text{B.22})$$

The following expression for the propagation constant can be obtained by applying the boundary conditions (*i.e.*, setting the determinant of the coefficients to zero):

$$\frac{j\omega\Lambda^2}{(j\omega/\nu) - \Lambda^2} \left(\frac{1}{\lambda_1} - \frac{1}{\lambda_2} \right) \left[\frac{d \ln Q}{dr} \right]_{r=r_w} + \left(\frac{j\omega}{\lambda_1} - \nu' \right) \left[\frac{d \ln Q_1}{dr} \right]_{r=r_w} - \left(\frac{j\omega}{\lambda_2} - \nu' \right) \left[\frac{d \ln Q_2}{dr} \right]_{r=r_w} = 0, \quad (\text{B.23})$$

which must be solved numerically. It is the estimation of this propagation constant that is typically calculated using the electrical analogy. Rewriting Equations B.16 - B.18 in terms of the ratios A/A_1 and A_2/A_1 , using the boundary conditions $u_x(r_w) = T(r_w) = 0$, and choosing the expression for A , one obtains

$$A = \frac{j\omega}{Q_w} \left(\frac{1}{\lambda_1} - \frac{1}{\lambda_2} \right), \quad (\text{B.24})$$

$$A_1 = -\frac{1}{\Lambda Q_{1w}}, \quad (\text{B.25})$$

$$A_2 = \frac{1}{\Lambda Q_{2w}}, \quad (\text{B.26})$$

where the w subscript is used to denote quantities evaluated at the tube wall (*i.e.*, at $r = r_w$). The final equations then become

$$u_x = \Lambda B \left[-j\omega \left(\frac{1}{\lambda_1} - \frac{1}{\lambda_2} \right) Q_{1w} Q_{2w} Q + \left(\frac{j\omega}{\lambda_1} - \nu' \right) Q_w Q_{2w} Q_1 - \left(\frac{j\omega}{\lambda_2} - \nu' \right) Q_w Q_{1w} Q_2 \right] e^{\Lambda x}, \quad (\text{B.27})$$

$$u_r = B \left[\frac{j\omega \Lambda^2}{(j\omega/\nu) - \Lambda^2} \left(\frac{1}{\lambda_1} - \frac{1}{\lambda_2} \right) Q_{1w} Q_{2w} \frac{dQ}{dr} + \left(\frac{j\omega}{\lambda_1} - \nu' \right) Q_w Q_{2w} \frac{dQ_1}{dr} - \left(\frac{j\omega}{\lambda_2} - \nu' \right) Q_w Q_{1w} \frac{dQ_2}{dr} \right] e^{\Lambda x}, \quad (\text{B.28})$$

$$T = B(\gamma - 1)T_o Q_w (-Q_{2w} Q_1 + Q_{1w} Q_2) e^{\Lambda x}, \quad (\text{B.29})$$

where $B = -A_1/(Q_w Q_{2w})$. The disturbance density and pressure can then be computed using Equations B.6 and B.9 and expressed as:

$$\rho = \rho_o B Q_w \left[\left(\frac{\nu' \lambda_1}{j\omega} - 1 \right) Q_{2w} Q_1 - \left(\frac{\nu' \lambda_2}{j\omega} - 1 \right) Q_{1w} Q_2 \right] e^{\Lambda x}, \quad (\text{B.30})$$

$$p = P_o B Q_w \left[\left(\frac{\nu' \lambda_1}{j\omega} - \gamma \right) Q_{2w} Q_1 - \left(\frac{\nu' \lambda_2}{j\omega} - \gamma \right) Q_{1w} Q_2 \right] e^{\Lambda x}. \quad (\text{B.31})$$

Appendix C Design and Manufacturing Details

Boundary layer transition experiments are highly sensitive to model imperfections and great care must be taken when manufacturing test apparatus. Before building the actual model, two prototypes were built (one half-scale, one full-scale) using solid sheets (instead of the expensive perforated sheet) in order to perfect the individual manufacturing processes and to validate the overall design. During this process, the following issues were found to be of particular importance and are discussed in the following sections:

1. Manufacturing of the perforated sheet with the desired parameters.
2. Rolling and welding of the cone sheet.
3. Attaching the cone sheet to the base cone.
4. Flush-mounting thermocouples through the perforated sheet.

In addition, during the search for a manufacturer for the perforated sheet, alternative materials were considered. Although not used, the most promising of these materials was a product called Feltmetal and is discussed in the final section.

C.1 Perforated Sheet

In contacting various manufacturers, it became apparent that there were three main challenges in making the required perforated sheet:

1. The small size of the holes.
2. The large aspect ratio of the holes (aspect ratio was approximately 10).
3. The sheer number of holes (at 1 hole/sec, it would take 174 days of continuous operation to drill the required 15 million holes).

A wide spectrum of manufacturing methods was considered including chemical etching, lithography, micro-EDM and laser drilling. Chemical etching was eliminated because it

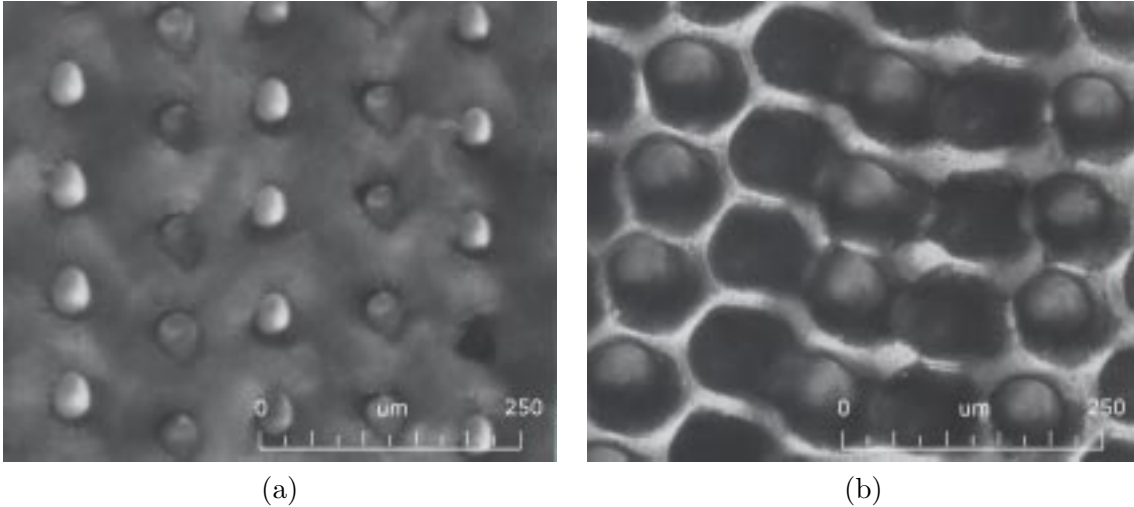


Figure C.1: Magnified image of the polyester (PET) Exitech perforated sheet (a) laser exit side (exposed to flow) (b) laser entry side (flush with model). The tear-drop shape of the holes on the laser exit side indicated the direction the laser head was moving when drilling the holes. The micrograph of the laser entry side indicated that the holes were connected.

only provides holes with an aspect ratio of 1. Lithography was eliminated since it could only be done in PVC and micro-EDM was eliminated because of the depth of the required hole. Laser drilling was left as the only viable alternative.

Two companies with the capabilities to produce a perforated sheet with the required parameters were found. The first, Exitech Limited (England), could only achieve this in polyester (PET). The second, Actionlaser Pty (Australia), was able to do this in essentially any metal. Their core competence is the manufacturing of stainless steel filter screens for sugar refineries and the requirements of this project were on the edges of their capabilities. Both companies used a pulsed Nd:YAG laser to drill the holes (one hole per pulse). Samples were obtained from both companies and examined under a microscope. Due to the laser drilling process, the holes were tapered with the small end corresponding to the laser exit side of the sheet. Refer to Figures C.1 and C.2 for micrographs of the Exitech and Actionlaser samples, respectively.

In general, there appeared to be a large variation from hole to hole. It was clear, however, that the Exitech sample had more uniform holes on the laser exit side, but it appeared that the holes were ‘connected’ on the laser entry side. Furthermore, the fact that Exitech was limited to plastics was a strong disadvantage. For these reasons it was decided to select Actionlaser as the manufacturer for the perforated sheet.

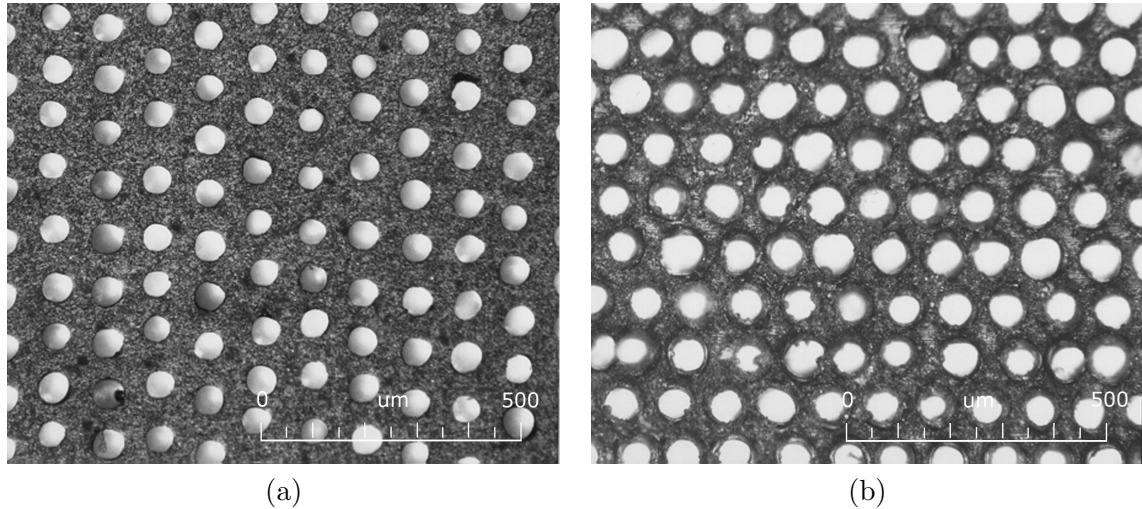


Figure C.2: Magnified image of the stainless steel 316 Actionlaser perforated sheet (a) laser exit side (exposed to flow) (b) laser entry side (flush with model). Careful examination of the micrographs allows one to see the grain boundaries on the surface of the sheet.

Measurements of 117 holes (on the Actionlaser sample) were found to have an average diameter of $55 \pm 4 \mu\text{m}$ spaced $100 \pm 8 \mu\text{m}$ apart (centre-to-centre) in a rectangular grid arrangement. This compared reasonably well with the independent assessment conducted by Actionlaser which indicated they had an average hole diameter of $49 \mu\text{m}$ (no standard deviation was provided). The final perforated sheet delivered for use on the actual model had slightly larger holes that were measured to be $60 \pm 4 \mu\text{m}$ in diameter and spaced $100 \pm 7 \mu\text{m}$ apart (refer to Figure C.3).

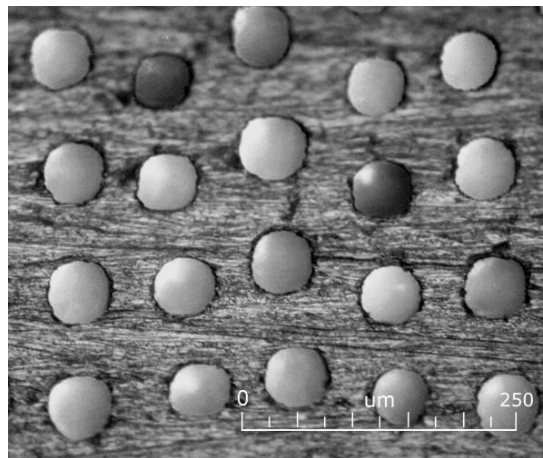


Figure C.3: Micrograph of the laser exit side of the final porous sheet used for the model.

C.2 Rolling and Welding of the Cone Sheet

As indicated previously the ‘cone sheet’ was manufactured by rolling two sheets of metal (one perforated, one solid) to form two longitudinal halves of a cone. The 26 gauge (0.45 mm) steel used for the perforated and solid sheets came from the same stock in order to insure that no spurious effects were introduced. The intention was that these two halves would be welded together along the longitudinal seam to form the ‘cone sheet’. This was a significant challenge since the small diameter (the front end) of the cone was only 25.2 mm (0.993 in). The smallest rollers used by precision sheet metal manufacturers are 50.8 mm (2.0 in); therefore, conventional rolling procedures were not possible. The only feasible method for forming the desired cone was by manually using a press brake which required considerable operator skill and expertise. In particular, making the two separate halves match exactly along the seam while still maintaining a reasonable tolerance on the overall half-angle of the cone was quite difficult. Another issue was that the laser drilling process resulted in significant residual stresses in the sheet that needed to be relieved. For this reason, a ‘rough cut’ was first performed to allow the material to relieve before performing the final precision cut to provide the required shape to accurately form the cone half. A local company, Lane & Roderick, succeeded in ‘rolling’ the final cone halves and benefited greatly from the two prototyping iterations. The subsequent welding of the cone halves was also not trivial since conventional welding of such thin materials typically results in significant warping and distortion. A specialty shop, California Lasers, performed a laser fusion weld that did not use filler material and essentially kept the sheet at room temperature except in the immediate vicinity of the weld. This technique minimized any surface rippling and resulted in a very fine weld that minimized the surface area that would affect the boundary layer. Refer to Figure C.4 for a micrograph of the final weld.

C.3 Attachment Details

In determining that the thermal interference fit was the best method of attaching the cone sheet to the base cone, the following requirements were considered:

1. Must minimize any non-uniformities in the surface of the cone. This includes such items as welds, fastener heads or imperfections.

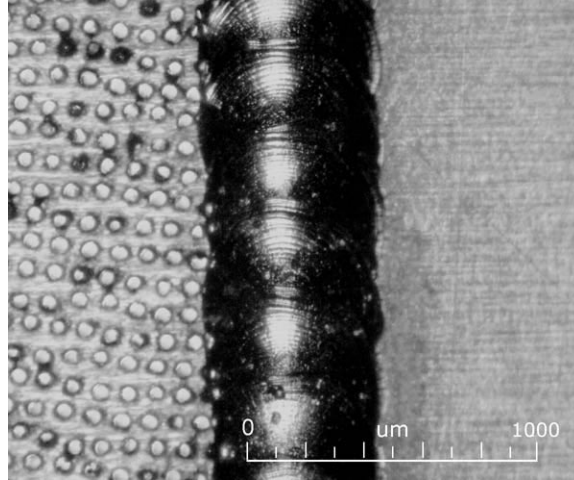


Figure C.4: Micrograph of the weld joining the perforated and solid sheet. The quality of the weld can be fully appreciated if one notes the scale on the micrograph.

2. Must allow the perforated sheet to fit to the cone ‘perfectly’ (*i.e.*, it could not allow regions where the sheet was not perfectly attached to the base cone. In such regions, flow would be able to enter one hole and out another).
3. Must be strong enough to withstand machining forces (since flush mounted thermocouples would be installed after attachment).
4. Must be strong enough to withstand tunnel forces.
5. Should allow for removal/replacement of the perforated sheet (in a non-destructive manner).

A wide variety of attachment methods were examined including the use of adhesive tapes, liquid adhesives, welding, brazing, mechanical fasteners, and finally the interference fit. When done properly, the interference fit was the most promising since it allowed the cone sheet to stretch over the base cone, closing any gaps between the two parts and completely eliminating surface imperfections (ripples). In addition, it eliminated the need for any mechanical fasteners that would disturb the boundary layer.

The mismatch in thermal coefficients of expansion for Al 6061 (base cone) and SS 304L (perforated sheet) was such that assembly of the base cone and perforated sheet in a cooled condition would result in an interference fit once the assembly was allowed to return to room temperature. The advantage of this was that it allowed the possibility of removing the cone sheet at a later date by simply cooling the assembly down to the same cold temperature.

Table C.1: Calculated interference fit based on thermal strains obtained from National Bureau of Standards.

Temperature	Induced Thermal Strain (mm/mm)		Interference Strain (mm/mm)	Actual Interference	
	Al 6061	SS 304L		Front	Back
70 K	0.0040	0.0028	0.0012	0.03 mm (0.0012 in)	0.11 mm (0.0043 in)
190 K	0.0022	0.0015	0.0007	0.02 mm (0.0007 in)	0.06 mm (0.0024 in)

This is to be contrasted with a typical interference fit where one part is heated and the other is cooled resulting in a fit which is essentially irreversible. Using the chosen technique, however, requires that the parts be cooled to very cold temperatures in order to achieve an adequate amount of interference. Data obtained from the National Bureau of Standards indicated that Al 6061 and SS 304L had thermal strains of 0.0040 and 0.0028 respectively, when cooled from room temperature down to 70 K (liquid nitrogen temperature). This resulted in an interference of 0.0012 mm/mm (or in/in), which translated into an interference of 0.03 mm (0.0012 in) at the front diameter of the cone and 0.11 mm (0.0043 in) at the back diameter of the prototype cone (see Table C.1). This amount of interference was more than adequate to retain the cone sheet in place.

Although the initial prototype was assembled in this manner, subsequent calculations revealed that the stresses induced in the actual perforated sheet would possibly exceed its material strength. This conclusion was based on the fact that the actual load bearing cross-sectional area of the perforated sheet would be half that of the regular solid sheet combined with the fact that the presence of the holes would induce stress concentrations. Although it may have been possible to test the material strength of a sample of perforated sheet, it was not necessary since an adequate fit resulting in reasonable stresses could be obtained by using a smaller temperature difference when performing the interference fit (see Table C.1). Instead of cooling the test model down to 70 K in liquid nitrogen, it was deemed adequate to go down to 190 K. Such temperatures were much easier to attain and, in fact, were obtained in special refrigerators commonly used to store biological cell samples. The second prototype (full-scale prototype) and the final model were both assembled in this manner. It should be noted that, although the original base cone was specified to have a half-angle of 5.0° ,

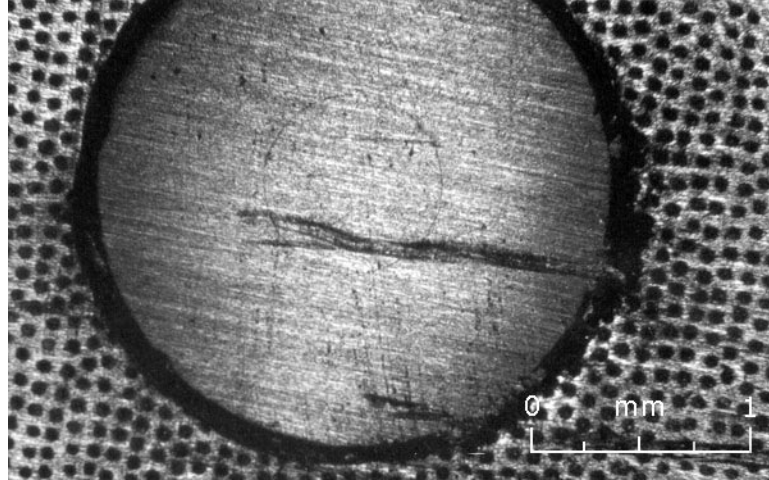


Figure C.5: Micrograph of a thermocouple flush-mounted in a test piece consisting of the perforated sheet with a Plexiglas backing. Note the holes appear as dark spots indicating that they have been clogged during the sanding process.

measurements indicated that it was actually 5.06° . Although well within any reasonable machining tolerance, it resulted in the back diameter being 1.0 mm (0.040 in) larger than expected. Such a large mismatch would have potentially caused serious problems with the attachment of the cone sheet onto the base cone had it not been taken into account.

C.4 Thermocouple Installation

Typically, when instrumenting a T5 model, the thermocouples are first installed approximately flush with the surface and then carefully sanded flush to the surface using very fine grit sandpaper so as to minimize the amount of material removed from the model. This technique typically resulted in a large sanding 'footprint' which made no difference on a solid surface, but would clog the holes on the porous surface. This damage was verified by installing the thermocouple in a Plexiglas test piece and examining it under a microscope. Figure C.5 shows a thermocouple installed in the test piece that had been backlit with a bright light source. Note that the holes in the perforated sheet appeared as black dots because very little light was coming through the holes. This was a strong indication that the holes had been clogged due to the sanding process.

A wide variety of different sanding techniques were tested, but it was found that it was impossible to not damage the porous surface. Ultimately, it was decided that the best that could be achieved was to minimize the size of the damaged area by using a rotary tool as

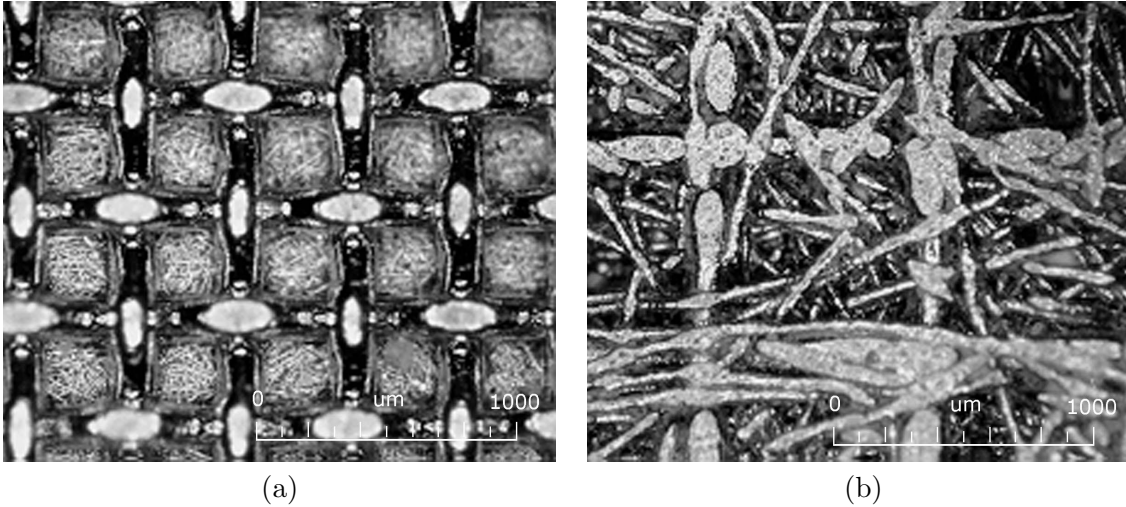


Figure C.6: Magnified image of Feltmetal by Technetics (a) FM1825 (fine fibers) (b) FM189 (coarse fibers). The coarse grid that appears in the foreground is used to provide structural integrity to the sheet. The fine fibres responsible for the acoustic absorption are in the background.

a mini disk sander. After much practice, this technique resulted in a damaged area that was roughly circular with a diameter twice that of a thermocouple. It was used for the thermocouples installed on both the porous surface and the smooth surface to insure that no spurious differences were introduced in the results.

C.5 Interesting Alternative Material - Feltmetal

During the design process, attempts were made to identify other candidate materials to use instead of the perforated sheet in the event that a suitable manufacturer could not be found. This search yielded a very interesting commercially available product known as ‘felt metal’. Manufactured by Technetics Corporation (Florida), this product consisted of a sintered, fibrous, porous metal typically formed in sheets. Its name was derived from the manufacturing process which was very similar to that used for organic felts. This product is often used as an acoustic liner in the nozzle of jet engines and in other noise suppression applications.

Two samples (different ‘grades’) were obtained from the manufacturer and examined under a microscope. The material consists of fine fibers of stainless steel (ranging from $8\ \mu\text{m}$ to $50\ \mu\text{m}$ in diameter depending on the grade) joined together in a random fashion (see Figure C.6). The diameter of the fibers and the approximate porosity of the felt metal can be tuned to particular frequencies. This material would be an ideal substitute for the

perforated sheet since it has many of the desired properties. It is typically made of stainless steel and can most certainly withstand the T5 conditions. This material can be machined (with some special care) and can also be welded and formed. It has the added benefit that there is the possibility that it could be directly sintered onto the surface of the cone - thereby eliminating the entire issue of attachment. The main drawback is that, according to the manufacturer's specifications, the acoustic absorption performance degrades with increased flow velocity. Furthermore, none of the stock grades available would be suitable for attenuating frequencies in the MHz range at the T5 conditions. It is unclear whether this is a manufacturing limitation or simply an economic consideration. In view of the apparent ease of manufacturing of this material (as compared to the perforated sheet), this product should definitely be viewed as a viable alternative for use as a boundary layer control surface.

Appendix D Acoustic Testing

Prior to manufacturing the model, a variety of samples of different materials were tested using facilities at QMI Incorporated (Los Angeles). The setup used was a ‘pitch-catch’ type setup involving a separate transmitter and receiver (see Figure D.1). The general test method involved measuring the pressure amplitude of the received signal reflected from a flat (unperforated) sheet of aluminum for a known transmitted signal. This reference measurement was assumed to correspond to perfect acoustic reflection and all other measurements for the other samples were made relative to this baseline.

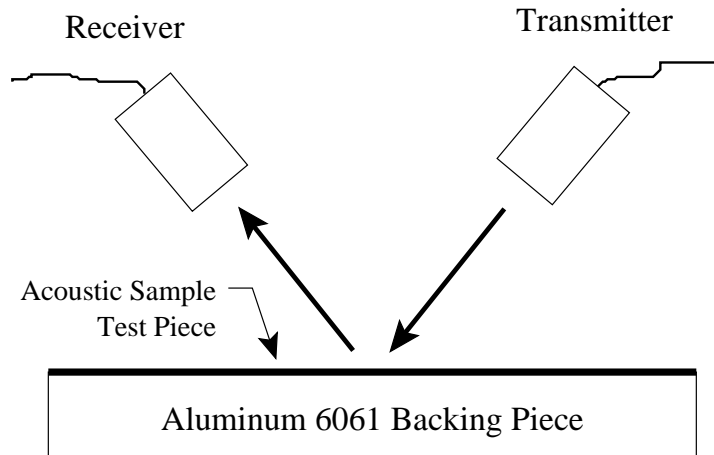


Figure D.1: Schematic diagram showing the pitch-catch setup used for the acoustic tests. The transmitter emits a signal that is reflected off the surface and measured by the receiver. The reduced signal measured by the receiver indicates the amount of absorption by the surface and the air. A measured signal using a solid surface is used as the baseline.

Two sets of tests were conducted. The first set consisted of air-coupled tests at 400 kHz and the second set was a water immersion test at 5 MHz. It is unclear whether the immersion testing is relevant to the air-coupled application of this project due to the large acoustic impedance mismatch. Immersion testing, however, is the only way to achieve such high frequencies. The samples tested included the Actionlaser perforated sheet, the Exitech perforated sheet and the two different grades of the felt metal product (FM 189 and FM 1825). All samples were tested with and without a metal backing plate of 6 mm (0.25 in) thick aluminum 6061 to simulate the presence of the base cone.

Table D.1: Summary results for acoustic testing of samples.

400 kHz Air Coupled Test	With Backing	Without Backing
Flat Sheet (Reference)	0.0 dB	0.0 dB
Perforated Sheet	-3.0 dB	-7.0 dB
FM189	-6.5 dB	-5.3 dB
FM1825	—	-11.8 dB
5 MHz Immersion Test	With Backing	Without Backing
Flat Sheet (Reference)	0.0 dB	0.0 dB
Perforated Sheet	-9 dB	-8 dB
FM189	-16 dB	— dB
FM1825	-19 dB	-17 dB

Refer to Table D.1 for a summary of the results obtained. The numbers given represent the difference between the magnitude of the reflected signal received from the reference surface and the reflected signal received from the desired test sample. For example, in the air-coupled tests, the perforated sheet with backing attenuated the signal by 3.0 dB relative to a flat sheet (this is the case that most closely approximates the actual experiment conditions).

Note that the results of these tests need to be interpreted with extreme care. They were static benchmark tests to provide an initial evaluation as to the effects of the perforated sheet and other samples. The results of these tests would not necessarily be reproduced when performing the actual experiments since there were a number of critical parameters that were different:

1. All of these tests were static (*i.e.*, with no flow). This was of particular concern for the Feltmetal products which were extremely good absorbers for these conditions, but whose performance is known to degrade with flow velocity, as stated by the manufacturer.
2. These tests were conducted at room temperature and at standard density. This means that the acoustic impedance for the air (or water for the immersion tests) did not match the experimental test conditions. This mismatched acoustic impedance is critical since it plays a significant role in the ‘reflectivity’ of a surface.
3. The immersion tests were not necessarily very accurate since it was found that the materials were hydrophobic (*i.e.*, the holes in the perforated sheet and the gaps in

the felt metal retained air bubbles). Attempts were made to remove the bubbles by forcing water over the samples and by allowing them to sit in the water for a long period of time.

